UNCLASSIFIED

PHOTOPHYSICS OF C60 COLLOIDS

by

Andrew F. Clements

A Dissertation Submitted to the Faculty of the

COLLEGE OF OPTICAL SCIENCES

In Partial Fulfillment of the Requirements
For the Degree of

DOCTOR OF PHILOSOPHY

In the Graduate College

THE UNIVERSITY OF ARIZONA

2012

UNCLASSIFIED

Report Documentation Page

Form Approved
OMB No. 0704-0188

1. REPORT DATE	2. REPORT TYPE	3. DATES COVERED
28 NOV 2012	**Dissertation**	**14-02-2012 to 23-11-2012**

4. TITLE AND SUBTITLE **PHOTOPHYSICS OF C60 COLLOIDS**	5a. CONTRACT NUMBER
	5b. GRANT NUMBER
	5c. PROGRAM ELEMENT NUMBER
6. AUTHOR(S) **Andrew Clements**	5d. PROJECT NUMBER
	5e. TASK NUMBER
	5f. WORK UNIT NUMBER
7. PERFORMING ORGANIZATION NAME(S) AND ADDRESS(ES) **U.S. Army TARDEC,6501 East Eleven Mile Rd,Warren,Mi,48397-5000**	8. PERFORMING ORGANIZATION REPORT NUMBER **#23516**
9. SPONSORING/MONITORING AGENCY NAME(S) AND ADDRESS(ES) **U.S. Army TARDEC, 6501 East Eleven Mile Rd, Warren, Mi, 48397-5000**	10. SPONSOR/MONITOR'S ACRONYM(S) **TARDEC**
	11. SPONSOR/MONITOR'S REPORT NUMBER(S) **#23516**
12. DISTRIBUTION/AVAILABILITY STATEMENT **Approved for public release; distribution unlimited**	
13. SUPPLEMENTARY NOTES	

14. ABSTRACT

The goal of this dissertation is to study the photophysics of suspensions of colloidal C60 particles to determine if their nonlinear optical (NLO) response is superior in any way to benchmark NLO materials such as molecular solutions of C60 and carbon black suspensions (CBS). C60 in molecular form is known to exhibit strong reverse saturable absorption (RSA) and it is posited that colloidal particles composed of many C60 molecules would maintain some degree of RSA behavior upon association, although some quenching is to be expected. CBS is known to have an NLO response that is dominated by nonlinear scattering resulting from a phase change due to heating of the carbon black particles by absorbed energy. Colloidal C60 particles that are many nanometers in diameter are similar to CBS, so it is posited that they would also have a nonlinear scattering mechanism contributing to their NLO response. Three samples of C60 colloids are characterized by several techniques, along with two carbon black suspensions and one molecular solution of C60. Transmission electron microscopy is used to determine morphology. Femtosecond pump-probe spectroscopy is used to determine the absorption spectrum and the relaxation kinetics of the first excited singlet state. Nanosecond laser flash photolysis is used to determine the absorption spectrum and the relaxation kinetics of the first excited triplet state. Z-scan is used to determine triplet-triplet absorption cross-sections. An experiment is performed to determine the percentage of the input energy that is transmitted, scattered, or absorbed by each sample. Computer modeling is performed to compare the experimental results to theory. Results show that all materials that exhibit nonlinear scattering have a constant extinction coefficient in the nonlinear regime, implying a characteristic size for the scattering centers that is independent of input energy. Quenching processes in C60 colloids are found to be morphology dependent, with more crystalline structures resulting in stronger quenching and less RSA. C60 colloids with stronger RSA are found to result in less nonlinear scattering than strongly quenched colloids. Highly crystalline C60 colloids were shown to have a stronger NLO response than the benchmark materials at medium to high energies.

15. SUBJECT TERMS

16. SECURITY CLASSIFICATION OF:			17. LIMITATION OF ABSTRACT	18. NUMBER OF PAGES	19a. NAME OF RESPONSIBLE PERSON
a. REPORT	b. ABSTRACT	c. THIS PAGE			
unclassified	**unclassified**	**unclassified**	**Public Release**	**186**	

THE UNIVERSITY OF ARIZONA
GRADUATE COLLEGE

As members of the Dissertation Committee, we certify that we have read the dissertation prepared by Andrew F. Clements

entitled Photophysics of C60 Colloids

and recommend that it be accepted as fulfilling the dissertation requirement for the Degree of Doctor of Philosophy

_____ Date:
Eustace Dereniak

_____ Date:
Russell Chipman

_____ Date:
Alan Kost

_____ Date:

_____ Date:

Final approval and acceptance of this dissertation is contingent upon the candidate's submission of the final copies of the dissertation to the Graduate College.

I hereby certify that I have read this dissertation prepared under my direction and recommend that it be accepted as fulfilling the dissertation requirement.

_____ Date:
Dissertation Director: Alan Kost

STATEMENT BY AUTHOR

This dissertation has been submitted in partial fulfillment of requirements for an advanced degree at the University of Arizona and is deposited in the University Library to be made available to borrowers under rules of the Library.

As the author of this dissertation was a federal government employee at the time it was prepared and submitted, this work is a “Governmental Work” subject to the conditions expressed in 17 U.S.C. § 105, which impacts copying and taking of quotations.

SIGNED: Andrew F. Clements

ACKNOWLEDGEMENTS

First and foremost, I would like to thank my advisor, Alan Kost. I could not have asked for a better dissertation director. He has been extremely helpful and is one of the kindest souls I have ever encountered. It has been a true privilege to study under the man who wrote the seminal paper in my field.

It has also been an honor to have Eustace Dereniak and Russell Chipman serving on my committee. Both are veritable icons in their specialties and I am grateful for their assistance and suggestions.

None of this would have been possible without the encouragement and support of my boss, mentor, and close friend, Rob Goedert. It was fun to have his companionship as we pursued our M.S. degrees in Optical Sciences together and I'm thankful for his support of my desire to continue to the Ph.D. level. Words cannot express the depth of my respect for him. I owe him a debt of gratitude that I can never repay.

I'd also like to thank my co-workers, Tom Whittaker, David Chinoski, and Clive Catchpole for their support and Doug Templeton for his mentorship through the years.

The research for this dissertation was funded under the In-House Laboratory Independent Research program at the U.S. Army Tank-Automotive Research, Development, and Engineering Center and I would like to thank Grant Gerhart, Rob Karlsen, David Gorsich, and Paul Decker for their financial and moral support.

The transient absorption spectroscopy experiments were done at the U.S. Air Force Research Laboratory and I would like to thank Joy Haley, Dan McLean, Jon Slagle, Tom Cooper, and Augustine Urbas for the use of their equipment, their help in interpreting the results, and for many helpful conversations. I would also like to thank Andy Mott and David Mackie of the U.S. Army Research Laboratory, who took the z-scan data, and David Ziegler of the U.S. Army Natick RDE Center for the TEM images.

Thanks to R. David Rauh, Fei Wang, and Jane Bertone of EIC Laboratories, Inc. for synthesizing the C60 colloid samples. Thanks to Anthony Sutorik, Todd Stefanik, and De Gao of Nanocerox, Inc. for synthesizing the carbon black suspensions.

I'm very grateful to my parents for all the sacrifices that they made through the years so that I could have the best education possible and to my sister, who reminds me that there is more to life than being a nerd.

Thank you to all my family and friends for praying for me and for putting up with me not being around much for the last few years.

Finally, thanks be to God, who gave me life and who makes it worth living.

DEDICATION

This dissertation is dedicated to God, the Father, Son, and Holy Spirit, who spoke into the void and said, “Let there be Light,” thereby creating that great mystery which we in Optical Sciences humbly strive to understand.

TABLE OF CONTENTS

TABLE OF CONTENTS—*Continued*

TABLE OF CONTENTS—*Continued*

LIST OF TABLES

LIST OF FIGURES

TABLE OF FIGURES—*Continued*

TABLE OF FIGURES—*Continued*

TABLE OF FIGURES—*Continued*

ABSTRACT

The goal of this dissertation is to study the photophysics of suspensions of colloidal C_{60} particles to determine if their nonlinear optical (NLO) response is superior in any way to benchmark NLO materials such as molecular solutions of C_{60} and carbon black suspensions (CBS). C_{60} in molecular form is known to exhibit strong reverse saturable absorption (RSA) and it is posited that colloidal particles composed of many C_{60} molecules would maintain some degree of RSA behavior upon association, although some quenching is to be expected. CBS is known to have an NLO response that is dominated by nonlinear scattering resulting from a phase change due to heating of the carbon black particles by absorbed energy. Colloidal C_{60} particles that are many nanometers in diameter are similar to CBS, so it is posited that they would also have a nonlinear scattering mechanism contributing to their NLO response.

Three samples of C_{60} colloids are characterized by several techniques, along with two carbon black suspensions and one molecular solution of C_{60}. Transmission electron microscopy is used to determine morphology. Femtosecond pump-probe spectroscopy is used to determine the absorption spectrum and the relaxation kinetics of the first excited singlet state. Nanosecond laser flash photolysis is used to determine the absorption spectrum and the relaxation kinetics of the first excited triplet state. Z-scan is used to determine triplet-triplet absorption cross-sections. An experiment is performed to determine the percentage of the input energy that is transmitted, scattered, or absorbed by each sample. Computer modeling is performed to compare the experimental results to theory.

Results show that all materials that exhibit nonlinear scattering have a constant extinction coefficient in the nonlinear regime, implying a characteristic size for the scattering centers that is independent of input energy. Quenching processes in C_{60} colloids are found to be morphology dependent, with more crystalline structures resulting in stronger quenching and less RSA. C_{60} colloids with stronger RSA are found to result in less nonlinear scattering than strongly quenched colloids. Highly crystalline C_{60} colloids were shown to have a stronger NLO response than the benchmark materials at medium to high energies.

CHAPTER 1: INTRODUCTION

Nonlinear optical materials are of interest for a host of applications, such as all-optical switching and optical limiting.[1] The quest for materials with improved nonlinear optical (NLO) response is a widely researched topic.

The types of materials investigated in this work respond to the energy or power in the incident laser pulse in such a way as to attenuate high energy pulses. Under normal (low energy) illumination conditions, they have a relatively high linear transmittance, but when a laser pulse is focused into them, they attenuate the light through nonlinear absorption or nonlinear scattering processes so that the transmittance decreases with increasing input energy.

Strongly absorbing nanoparticle suspensions have an NLO response that is dominated by a nonlinear scattering mechanism. The strong linear absorption of the particles drives explosive bubble formation (and other processes) to rapidly create a multitude of scattering centers in the focal region of the laser beam that absorb and scatter much of the incoming light away from the transmitted beam path.

Reverse saturable absorber (RSA) dyes have an NLO response that is dominated by a nonlinear absorption mechanism. Initial absorption from the ground state causes excited states to be populated. When these excited states are more strongly absorbing than the ground state and have significant lifetimes with respect to the input laser pulse, the pulse can be strongly attenuated by this nonlinear absorption.

Two nonlinear optical materials that are commonly used as benchmarks for these general categories of nonlinear optical materials are carbon black suspensions and

solutions of C_{60}. Carbon black suspensions have a nonlinear optical response that is dominated by nonlinear scattering. Molecular C_{60} has a nonlinear optical response that is dominated by reverse saturable absorption (RSA).

It has been noted that under certain conditions, C_{60} forms stable colloidal particles in suspension. Intuitively, one might expect that the nonlinear optical response of C_{60} colloids might resemble that of molecular C_{60} for very small colloids and that of carbon black for large-scale colloids. This work investigates the photophysics of C_{60} colloids to determine if this general trend is true and to determine if there is any improvement in the nonlinear optical response to be gained by the potential combination of nonlinear absorption and nonlinear scattering behaviors in such materials.

CHAPTER 2: LITERATURE REVIEW

The nonlinear optical (NLO) properties of carbon black suspensions (CBS) have been extensively studied.

Mansour et al. reported a series of experiments on the photophysics of carbon black suspensions.[2] The mechanism they propose for the NLO properties of CBS is strong linear absorption giving rise to thermionic emission, resulting in avalanche ionization and thus, nanoplasmas that absorb and scatter the light. They reported the NLO behavior of CBS to be fluence-dependent (i.e., related to the time-integrated irradiance). They performed a non-calibrated measurement of the simultaneous transmittance, scattering (at one angle), and absorption of CBS, reporting that above the nonlinear threshold, absorption increases mildly and levels off, while nonlinear scattering increases dramatically. They performed measurements of scattering as a function of angle, establishing that the scattering centers formed in the nonlinear regime can be treated according to Mie theory.

Fein et al. conducted a study of the threshold energies for the onset of NLO activity in CBS and found it to be strongly solvent dependent.[3] Nonlinear scattering was also found to be strongly solvent dependent. However, emitted light measurements were nearly independent of solvent. They attributed much of the nonlinear attenuation to be a result of nano-bubbles formed around the particles well below the plasma threshold and performed thermodynamic numerical modeling to support this.

Riehl and Fougeanet proposed a thermodynamic model to analyze the performance of CBS.[4, 5] Their results indicated two mechanisms at work in CBS:

formation of strong scattering centers via the sublimation of the particle itself and, in some solvents with appropriate thermodynamic properties, the formation of nanobubbles of evaporated liquid around the particles at lower input energies which also act as scattering centers. In the case of carbon black particles in water, they observed only a single nonlinear threshold corresponding to particle sublimation. They attribute the emitted white light seen during CBS's nonlinear response to be incandescence of the carbon particles. A simplified form of the thermodynamic model presented by Riehl and Fougeanet serves as the basis for the thermodynamic numerical computations in this dissertation.

Durand et al. conducted time-resolved scattering and pump-probe experiments on CBS in different solvents.[6] They found that the results were only solvent dependent after the first 1 or 2 nanoseconds of the pulse, leading to the interpretation that the initial nonlinear scattering is due to scattering from a nano-plasma caused by sublimation of the particle, followed by additional scattering resulting from bubble growth in the liquid.

Belousova et al. have also conducted experiments and presented a thermodynamic model of aqueous suspensions of carbon particles.[7] Their model consists of heating of the particles by absorbed light, formation of a vapor shell by explosive boiling of the liquid surrounding the particle, and growth of this shell. Light is attenuated predominantly by scattering from the vapor shell. Qualitative agreement between the model and experimental results were achieved.

McEwan et al. proposed a model for beam propagation in carbon black suspensions.[8] Like many of the other models, it is based on heating of the carbon

particles by the absorbed laser light and bubble formation upon particle vaporization when the particle reaches a critical temperature. In terms of beam propagation, it assumes that the transmittance through CBS follows the Beer-Lambert law and that the extinction coefficient has a digital character; it has one value for particle temperatures below vaporization and a higher value after the nonlinear scattering center has formed. The Beer-Lambert law is defined as:

$$T = e^{-\propto L},$$

where T is the transmittance, α is the extinction coefficient, and L is the path length through the material. The values for the extinction coefficient are obtained from experimental data. This strategy was adopted for the modeling of beam propagation in this dissertation.

Since its discovery,[9] C_{60} has been widely studied. In particular, the photophysical properties of the C_{60} molecule have been the subject of intense study. Many authors have reported on the photophysical properties of molecular solutions of C_{60}.[10-24] Likewise, many authors have studied the photophysical and structural properties of solid films of C_{60}.[25-45] Of particular note, Ebbesen et al. measured the excited singlet and excited triplet state properties and spectra of C_{60} in toluene via picosecond and nanosecond flash photolysis.[10] Sension et al. reported the excited state spectrum and temporal characteristics of C_{60}'s NLO behavior.[11] Tutt and Kost first reported the optical limiting behavior of C_{60} in solutions and solid matrices.[46, 47] Tremendous interest in C_{60}'s optical limiting and optical switching properties has followed.[1, 48-60] Mishra et al. emphasized

the importance of nonlinear scattering to the NLO response of C_{60} at very high input energies, which is an important consideration in this dissertation.[61, 62]

Nashold and Walter performed a study of the mechanisms involved in the NLO responses of carbon black suspensions and C_{60} solutions.[63] Two experiments were performed: one experiment with the sample in the center of an integrating sphere and collecting transmitted, total scattered, and absorbed energy data, as well as an experiment in which the spatial distribution of the scattered light was collected. The first experiment is an earlier version of the total scattering experiment performed in this dissertation. The results showed that for CBS, absorption and scattering both increased once the NLO threshold was exceeded, with the absorption increasing more gradually than the scattering but with a nearly equal share of absorption and scattering over much of the response range. The results showed that absorption was dominant for a solution of C_{60} in toluene, but with a significant contribution from scattering. Over much of the response range, the ratio of scattered to absorbed light was reported to be about 0.4. In view of the results to be reported below in this dissertation, it is likely that the C_{60} solution used in the Nashold study was not totally dissolved and may have contained some C_{60} molecules that were clustered together as particles.

Under certain conditions, C_{60} forms stable colloidal assemblies in solvents.[64-73] Colloidal suspensions of C_{60} particles can also be formed in binary solvent mixtures, in which one is a good solvent and the other is a poor solvent for C_{60}.[74-78] Aqueous suspensions of colloidal C_{60} particles are also formed by a number of methods,[79-93] including solubilization in micellar solutions.[84, 90, 94-98] Studies have been done of the

photophysical properties of these colloidal fullerene suspensions.[96, 97, 99, 100] Some of these results indicated that colloidal C_{60} suspensions could have interesting NLO properties. In particular, Fujitsuka et al. reported a very broad excited triplet state absorption spectrum that decayed over time to the typical C_{60} triplet absorption spectrum which peaks near 740 nm.[99] The photochemical properties, and in particular the generation of reactive oxygen species (ROS) via intersystem crossing to the triplet state, have been of interest both for potential exploitation for photodynamic therapy[101] and regarding concerns about their potential environmental impact, as there have been reports of significant cytotoxicity effects.[79-82] A variation of colloidal C_{60} suspensions, known as astralenes, has also been the focus of considerable study for its NLO properties.[102-109]

The previously known synthesis methods for generating colloidal C_{60} all yield very dilute solutions. To better investigate the potential NLO properties of C_{60} colloids, several alternate synthesis methods were developed to achieve high colloid loadings in aqueous suspensions with Triton X-100 as a surfactant (to be reported below). The new preparation methods were based on those reported in the literature by Deguchi et al.[73, 92] and Beeby et al.[94, 96, 100, 110] and yield suspensions with concentrations on the order of 4 mM.

This work builds upon the previous understandings of the NLO behavior in the benchmark materials of CBS and molecular C_{60} (seeking to glean further insights) and examines the NLO behavior of new, highly concentrated colloidal C_{60} suspensions, making an effort to relate the observed nonlinear absorption and nonlinear scattering properties to physical properties of the colloids, such as size and morphology.

CHAPTER 3: SYNTHESIS AND CHARACTERIZATION OF SAMPLES

3.1. Synthesis

3.1.1. C_{60} in Toluene Solution (C_{60}-Tol)

A solution of C_{60} in toluene was prepared as a benchmark sample against which to compare the performance of the other samples. All of the other samples were suspended in water. However, C_{60} has an extremely low solubility in water, so another solvent had to be chosen for the molecular solution of C_{60}. Toluene was chosen because C_{60} has high solubility in toluene and there is considerable published data on C_{60} in toluene.

59.9 mg of C_{60} (99.9% pure) was combined in a pre-cleaned 40 mL vial with 35 mL of spectrophotometric grade toluene (which was further filtered through a 0.5 μm PDFE filter) and mixed briefly with a magnetic stirrer. To ensure that the C_{60} completely dissolved into the toluene and no particulates were present, the solution was heated to 140°F for one hour and stirred overnight. 2 mL of the stock solution was added to 2.8 mL of filtered toluene in a 7 mL pre-cleaned vial. The concentration tested in the total scattering experiment was 0.713 mg/mL.

3.1.2. Acidified Carbon Black in Water (CBS-1)

A suspension of carbon black in deionized water was prepared for use as another benchmark sample. An acid digestion process was used to de-agglomerate and functionalize carbon black particles with carboxylic acid groups. 20 mL of concentrated ACS grade nitric acid (70%) and 30 mL of concentrated ACS grade sulfuric acid (95-98%) were placed in a 500 mL beaker. To this mixture, 1 g of carbon black (Cabot

Monarch-1000®) was added. The carbon black was added gradually as the solution was swirled, to avoid igniting the carbon. This mixture was warmed to a low temperature on a hot plate, which resulted in the emission of orange vapors. After approximately 1 hour, vapor emission ceased, leaving a brown, oil-like substance in the beaker. This oily remainder was rinsed into a round bottom flask using deionized water and heated to evaporate excess acid. The material that remained was transferred to a beaker. The material was rinsed twice with deionized water, sonicated to disperse the carbon black particles, and then heated to evaporate the liquid until a dry powder remained. Water was added a third time, followed by sonication, then centrifugation to remove large particles. The supernatant was collected and the remaining water was evaporated. 0.033 g of the resulting solid was dispersed into 5 mL deionized water to form the carbon black suspension referred to as CBS-1 in this work.

3.1.3. Agglomerated Carbon Black in Water (CBS-2)

A second carbon black suspension was prepared as a benchmark material, with the intent of demonstrating the difference in nonlinear optical performance between two carbon black suspensions with differing particle sizes.

30 g of carbon black (Cabot Sterling-1120®) was combined with 350 mL of concentrated (70%) nitric acid (HNO_3) and refluxed over the weekend. The mixture was filtered through a course silica frit, trapping particles on the surface. The particles were washed with water and ethanol to remove any remaining nitric acid. The remaining oxidized particles were mixed with tetrahydrofuran (THF) and sonicated to disperse. This suspension was centrifuged to remove the heaviest particles by sedimentation. The

supernatant was collected. The sediment was redispersed in THF and the process of sonication and centrifugation was repeated twice more. All of the collected supernatant was combined and concentrated to a small volume by evaporation. Hexane was added gradually to the THF suspension, causing the carbon black particles to precipitate. This mixture was centrifuged and the solid precipitate was redispersed into deionized water and filtered through a syringe filter with an average pore size of 20 nm. Although this preparation was intended to result in very small carbon black particles, the particle sizing data shows that large agglomerates were formed. This carbon black suspension is referred to in this work as CBS-2.

3.1.4. C_{60} Colloids in Water with 15% (v/v) Triton X-100 Surfactant (C_{60}-1)

10 mg of C_{60} (98% purity) was dissolved into 4 mL of toluene by stirring for 3 days. The UV-Vis spectrum of this toluene solution was measured using a 2 mm cell. The solution was diluted by 1:1 with neat toluene and the UV-Vis spectrum of the diluted sample was recorded. The dilutions were repeated twice more.

The absorbance at 532 nm was plotted against C_{60} concentration (mg/mL). The absorbance of the C_{60} in toluene solution was found to be linear with concentration, according to the following relation:

$$A_{532} = 0.2311\ (C_{60}\ in\ mg/mL) + 0.0058.$$

Note that absorbance is defined as:

$$A = -log_{10}\left(\frac{I}{I_0}\right),$$

where I_0 is the irradiance incident upon a sample and I is the irradiance that is transmitted through a sample. Absorbance is synonymous with the term optical density (OD). Absorbance is sometimes defined in terms of the natural logarithm:

$$A = -ln\left(\frac{I}{I_0}\right),$$

but in this case, the log base 10 definition is used. Absorbance is often confused with absorptance, which is defined as a simple ratio of the transmitted to incident irradiance:

$$a = \frac{I}{I_0}$$

The molar extinction coefficient, ε, was found to be 832 M^{-1} cm^{-1} by plotting this absorbance relation in terms of the C_{60} concentration in moles, which agrees fairly well with data from the literature.[111]

All of the C_{60} toluene solution (including the diluted portions) was combined (for total volume of 7 mL) in a 16 mL wide mouth vial and 0.3 mL of Triton X-100 was added. To remove the toluene, the vial was heated in a 50°C water bath with argon bubbling through it. After 4 hours, all of the toluene had evaporated and a dark brown Triton X-100 and C_{60} residue remained. Deionized water (resistivity of 10-15 Megaohm-cm and TOC < 30 μg/L [ppb]) was then added to the residue in 0.7 and 1 mL increments and sonicated between additions. The resulting suspension was dark brown, the color typical of C_{60} colloids. A small amount of precipitated C_{60} was also present in the bottom of the vial. The suspension was filtered through a 0.22 μm pore size syringe filter. About 1.9 mL of filtered solution was obtained.

To determine the amount of C_{60} present in the suspension, the amount of C_{60} that was not incorporated into the suspension was redissolved and measured. The C_{60} residue that remained in the bottom of the vial, on the syringe filter, and in the syringe was dried under vacuum for 4 hours. Toluene was rinsed through the syringe to recover C_{60}. The filter membrane was removed from the syringe filter and cut into small pieces that were placed in the vial containing the C_{60} residue, to which toluene was added. C_{60} was extracted into 4.2 mL of toluene with stirring for 24 hrs. The extracted C_{60} in toluene was passed through a 0.2 μm pore diameter syringe filter and a UV-Vis spectrum was taken. The absorbance at 532 nm was 0.325. Since the absorbance baseline from 700 nm to 800 nm was zero, indicating no scattering from large particles, it may be assumed that no contaminants were present. The absorbance versus concentration relation indicates that the concentration of the reclaimed C_{60} in toluene solution is 1.38 mg/mL. Thus, the total amount of reclaimed C_{60} that was not extracted by Triton X-100 is 5.80 mg, leaving 4.20 mg of C_{60} extracted by the Triton X-100 comprising the C_{60} colloids in the aqueous suspension. The initial C_{60} concentration in the Triton X-100/water suspension was therefore 2.21 mg/mL.

Serial aqueous dilutions were made of this stock solution using Triton/water (15% v/v) to yield solutions of 1.105, 0.553, 0.276, 0.138 mg/mL, respectively. Their UV-Vis spectra were taken using a 2 mm cell. The diluted samples appeared stable; no precipitation was observed overnight.

The absorbance at 532 nm was plotted against C_{60} concentration in molarity (mol/L). The Beer-Lambert Law plot yielded a molar extinction coefficient, ε, of 1289

M^{-1} cm^{-1}. When absorbance was plotted against C_{60} concentration in mg/mL, the following calibration curve was obtained:

$$A_{532} = 0.3579\ (C_{60}\ in\ mg/mL) + 0.0126.$$

The sample used in the transient absorption spectroscopy experiments was determined to have an absorbance of 1.15 at 532 nm in a 2 mm path length cell. Therefore, the calculated C_{60} concentration in this sample is 3.18 mg/mL or 0.00441 M. The sample used in the total scattering experiment was determined to have an absorbance of 0.2271 at 532 nm in a 2 mm path length cell and consequently a concentration of 0.6 mg/mL.

3.1.5. C_{60} Colloids in Water with 11% (v/v) Triton X-100 Surfactant (C_{60}-2)

7 mg of C_{60} was added to 8 mL of N-Methylpyrrolidone (NMP) and stirred in the dark for three days. The solution was allowed to settle and the supernatant was filtered through a 0.2 µm syringe filter so that no particulate C_{60} was present. The 8 mL solution of C_{60} in NMP was added drop-wise while stirring to a solution of 1 mL of Triton X-100 and 300 mL of deionized water, forming a yellow solution. Half this solution was dialyzed against deionized water, separated into two equal portions (75 mL each) into two 250 mL flasks, and freeze-dried. After freeze-drying, a brownish slurry residue remained in each flask. 1 mL of deionized water was added to each flask and both flasks were sonicated in an ultrasonic bath until the residue was fully redissolved. The second half of the 300 mL solution was processed in the same way. The contents of all four flasks were combined, resulting in 4.5 mL of a dark brown suspension. The final suspension contained approximately 0.5 mL of Triton X-100 and 4 mL of deionized

water. The suspension was filtered through a 0.22 μm syringe filter. The concentration of C_{60} in the sample would have been 1.5555 mg/mL if all of the initial C_{60} was converted to nanoparticles. Assuming some loss in the process, the concentration of C_{60} in the base suspension is estimated as 1.5 mg/mL.

At full concentration, this sample had an absorbance at 532 nm of 1.238. Since a serial dilution study was not done to determine a concentration equation, the concentrations of the diluted samples used in the transient absorption spectroscopy and total scattering experiments are estimated by simple ratio. The sample used in the transient absorption study had an absorbance at 532 nm of approximately 1.0 in a 2 mm path length cell, so its concentration is estimated as 1.2 mg/mL. The sample used in the total scattering experiment had an absorbance of 0.2284 at 532 nm in a 2 mm path length cell and consequently an estimated concentration of 0.28 mg/mL.

3.1.6. C_{60} Small Colloids in Water with 10% (v/v) Triton X-100 Surfactant (C_{60}-3)

The synthesis of this sample was based on a method published by Beeby, which indicated that C_{60} colloid size may be controlled by the ratio of C_{60} to Triton X-100 surfactant. The intent of this sample was to produce very small nanoparticles.

A molecular solution of C_{60} in toluene with a concentration of 2.5 mg/mL was prepared by stirring overnight in the dark. 5 mL of the C_{60} in toluene solution was mixed with 5 g of Triton X-100. The toluene was removed by rotary evaporation at 40°C, leaving a concentration of 2.68 mg/mL of C_{60} in Triton X-100.

For the sample used in the total scattering experiment, 0.35 mL of the concentrated C_{60} in Triton X-100 suspension was added to 3 mL of autoclaved, ultra

filtered water and dispersed in a hematology mixer overnight. The estimated concentration of C_{60} in this sample is 0.3 mg/mL.

3.2. Characterization

3.2.1. Transmission Electron Microscopy

Transmission electron microscopy (TEM) was performed to examine the C_{60} colloid samples under high magnification to determine the morphology of the particles and to gain some insights on the sizes of primary particles and agglomerates. TEM allows imaging of structures that are too small to observe optically.

3.2.1.1. Experimental Technique

Particle size characterization was conducted using a 200 kV transmission electron microscope (TEM). Statistics were obtained by manually measuring the sizes of all particles in the images, using statistical software.

3.2.1.2. Results and Discussion.

TEM images were obtained for the C_{60}-1 colloidal suspension. Figure 3-1 shows TEM images at different magnifications of the C_{60}-1 suspension. Images (a), (b), and (c) had been filtered through a 0.22 micron syringe filter. The particles are polydisperse, with sizes falling mostly in the range of 10 to 50 nm. In general, the particle shapes trend from rather spherical to more faceted as the particle size increases. Particle sizing from 100 particles in image (a) showed an average particle size of 18 ± 7 nm. As the molecular density of C_{60} is $1.44 \times 10^{21}/cm^3$,[112] an 18 nm diameter spherical cluster will

contain approximately 4392 C_{60} molecules if the sphere exhibits crystalline packing (face centered cubic). Image (b) shows several C_{60} particles with sizes near 5 nm. Image (c) shows particles ranging in size from approximately 10 nm to 40 nm. While lattice fringes were observed for particles larger than 20 nm, evidence of crystallinity was not seen in particles smaller than 20 nm in diameter. However, further data would be required to confirm any size dependence to the crystalline nature of C_{60} particles. Image (d) shows colloidal particles of approximately 100-150 nm in diameter in the unfiltered C_{60}-1 colloidal suspension. These particles clearly exhibit facets and fringe patterns, indicating crystalline packing.

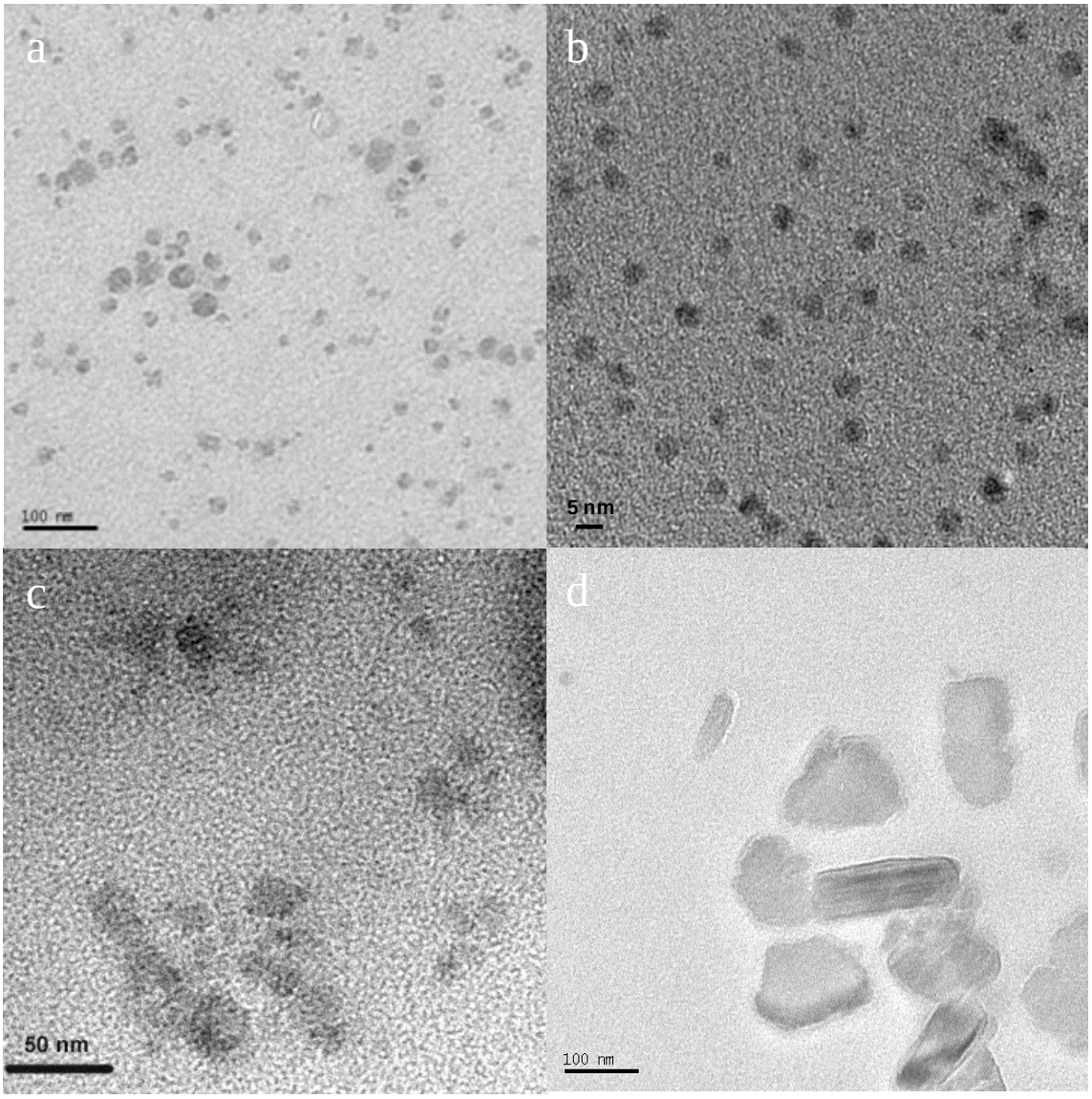

Figure 3-1. TEM Images of the C_{60}-1 Suspension.

Figure 3-2 shows TEM images of a colloidal particle from the C_{60}-1 suspension at high magnification, revealing faceted edges and parallel lines. As shown in the inset to panel (b), the diffraction pattern in the digital Fast Fourier Transform (FFT) image is consistent with either face centered cubic or a hexagonal crystalline symmetry, but was not sufficient to distinguish between these possible structures.

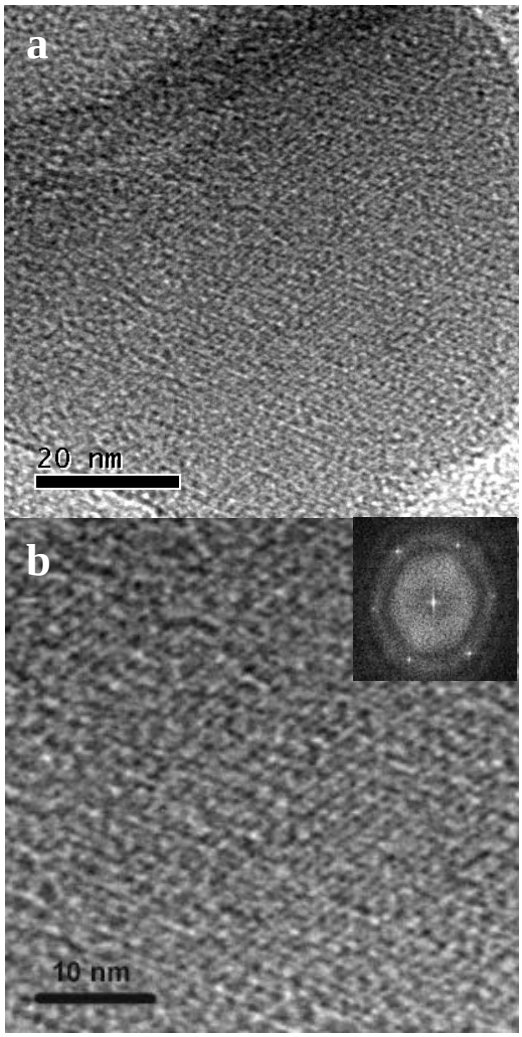

Figure 3-2. High Resolution TEM Images of C_{60}-1. Inset to (b): Fourier Transform of High-Res TEM.

Like C_{60}-1, TEM images of the C_{60}-2 suspension revealed a broad particle size distribution with many large agglomerates, as shown in Figure 3-3(a), and many small particles on the order of 5 nm in diameter, as shown in Figure 3-3(b). Notably, there is little or no evidence for lattice fringes even in the larger agglomerates in this sample. This suggests that the agglomerates formed in the C_{60}-2 synthesis have less crystallinity and are less tightly packed than the C_{60}-1 agglomerates.

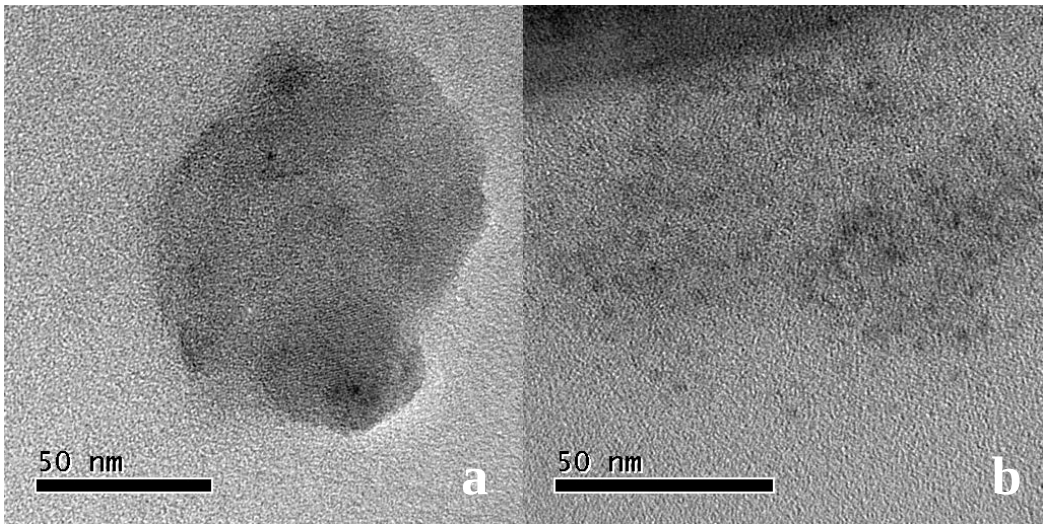

Figure 3-3. TEM Images of the C_{60}-2 Suspension.

As shown in Figure 3-4, the agglomerates found in the C_{60}-3 suspension had much less defined boundaries than the C_{60}-1 sample. The agglomerates seem to be formed of mostly spherical particles near 10 nm in diameter. Overall, this sample also appears to have less crystallinity than C_{60}-1.

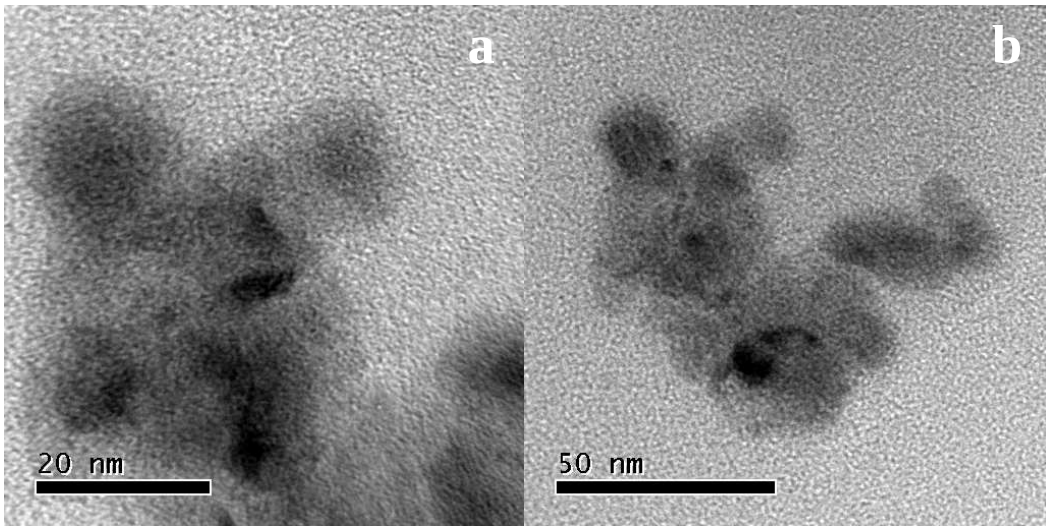

Figure 3-4. TEM Images of the C_{60}-3 Suspension.

3.2.2. Dynamic Light Scattering

Dynamic light scattering is a technique for measuring particle size distributions by measuring Brownian motion of a large number of particles and relating this to the sizes of the particles. Brownian motion is the random movement of suspended particles as they are "pushed" by the solvent molecules surrounding them. Smaller particles are pushed further and move more rapidly than larger particles.

The velocity of Brownian motion is quantified by the translational diffusion coefficient, which is usually given the symbol, D. The velocity of Brownian motion is related to the particle's size via the Stokes-Einstein equation:

$$d = \frac{\mathbb{k}\mathbb{T}}{3\pi\eta D},$$

where d is the hydrodynamic diameter of the particle, $\mathbb{k}$ is Boltzmann's constant, T is absolute temperature, and η is viscosity.

Laser light scattered from a collection of particles will interfere to create a speckle pattern. This speckle pattern will be constantly fluctuating because the particles are moving. The smaller the particles are, the faster they move, and the faster the rate of intensity fluctuations in the speckle pattern. DLS instruments use digital autocorrelators to compare the signal from irradiance due to the scattered light with itself at several points in time. For large particles, there will be correlation in the scattered light signal for a long time, because they move slowly. Conversely, the correlation in the scattered light signal will fall of quickly for small, rapidly moving particles. The correlation function decays exponentially. Size data can be extracted from the correlation function

by performing either single or multiple exponential fits to the correlation function. A single exponential fit results in the z-average particle size diameter. Multiple exponential fits result in a plot of particle size vs. the intensity of light scattered. Algorithms employing Mie theory are used to convert the intensity distribution to volume and number distributions.

It is important to accurately know the viscosity of the sample and the temperature during data collection. It is important to know the complex refractive indices of both the particles and the liquid to convert from intensity to a volume or number basis.

3.2.2.1. Experimental Technique

The particle size distributions of the samples were measured by dynamic light scattering (DLS). In most cases, dilution was necessary to obtain good DLS data. Samples were diluted with either ultrapure deionized water (pH 7.5, 18 Megaohm-cm) or autoclaved, ultra filtered water (0.02 µm filtered). For undiluted samples, the viscosity input to the DLS instrument was determined for the ratio of Triton-X-100 to water in the sample by interpolation of viscosity data available on the DOW Answer Center knowledge base.[113] For diluted samples, the viscosity was very near that of water. The complex refractive index was set at 2.2 – 0.06i for the colloidal C_{60} DLS measurements, in accordance with the literature.[84, 112, 114] The complex refractive index was set at 1.84 – 0.85i for the carbon black particles.[115, 116]

3.2.2.2. Results and Discussion

Particle size distributions were measured via DLS for each suspension at about the same time that the transient absorption spectroscopy and total scattering experiments were conducted so that if there were any changes to the size distributions over time, this would not be missed. Table 3-1 summarizes the particle size distribution statistics obtained by DLS. Data are presented in z-average, intensity, volume, and number bases. It is important to consider all of these bases to obtain a clearer picture of the particle size distribution. The raw data of a DLS measurement is a correlogram, which is converted to a particle size distribution on an intensity basis. This is artificially weighted towards larger particles, because scattering intensity is proportional to the sixth power of the particle radius (according to the Rayleigh approximation for small particles). Using the refractive index of the particle and solvent, the intensity distribution is operated upon to calculate a volume distribution based on Mie theory. A further numerical operation using the refractive indices of the particle and solvent yield the number distribution. Although the number distribution represents the actual physical number of particles of particular sizes present in the suspension and is typically what one desires, each of these mathematical operations can be an opportunity for errors to be introduced. The z-average particle size is the intensity-weighted mean hydrodynamic size. It is derived from a cumulants analysis of the correlogram, in which a single particle size is assumed and a single exponential fit is applied to the autocorrelation function.

Table 3-1. Particle Size Distribution Statistics from DLS Measurements.

Sample Description	Z-average (nm)		Intensity (nm)		Volume (nm)		Number (nm)	
	APS	PDI	APS	PW	APS	PW	APS	PW
CBS-1 (transient abs.)	79.9	0.197	102	51.8	67.1	48.6	37.5	13.6
C_{60}-1 (0.2 µm filtered, transient absorption)	105	0.25	117	39.7	94.9	37.4	70.3	19.9
C_{60}-1 (unfiltered, transient absorption)	106	0.219	131	55.2	101	53.3	64.5	21.1
CBS-1 (total scattering)	81.11	0.246	113.6 (99) 4041 (1)	70.35 1066	53.14 (85.4) 253 (9.2) 4552 (5.4)	29.93 81.07 1070	33.63	12.55
CBS-2 (total scattering)	1086	0.6	2102 (90.5) 135.9 (9.5)	921.2 40.24	2815 (99) 135.4 (1)	1140 49.92	1600 (1.9) 102.3 (98.1)	765.8 36.05
C_{60}-1 (total scattering)	112.1	0.207	141.9	60.38	115.6	63.85	69.39	25.7
C_{60}-2 (total scattering)	102.2	0.181	124.7	51.73	95.16	50.63	61.97	21.14
C_{60}-3 (total scattering)	11.71	0.409	9.129 (75.3) 220.4 (21.4) 4543 (3.3)	2.655 92.29 944.9	7.308 (99.9) 217.3 (0.0) 4934 (0.1)	2.123 89.53 928.7	6.221	1.495

The data for CBS-1 taken in close proximity to the transient absorption spectroscopy measurements is indicative of a broad size distribution; the average particle size increases when progressing from a number to intensity basis. When the DLS measurements were repeated for CBS-1 in close proximity to the total scattering

measurements, the particle size distribution on a number density basis looked very much the same. Some larger contaminant particles had been introduced (likely from vials, syringes, or sample cells that had not been adequately cleaned), but the dominant mode in the multimodal size distributions was that of the smallest particles, so the degree of contamination was small.

While the intent for CBS-2 was to synthesize a carbon black suspension with a very small particle size, the DLS data shows that the sample was highly prone to agglomeration. Even though the sample was filtered through a 0.02 μm filter during synthesis, the DLS particle size data shows a bimodal distribution with one mode centered around 102 nm in diameter and the other centered around 1600 nm in diameter on a number density basis. When the DLS instrument was observed processing the data, there was also occasionally a spike around 1 nm, so there may also be a portion of the size distribution in this very small size range, which is below the DLS instrument's ability to resolve.

The data for the unfiltered C_{60}-1 colloidal suspension and the same suspension after filtration through a 0.2 μm pore size cellulose acetate filter and vacuum evacuation to remove bubbles that were caused by filtration shows little change in measured particle size as a result of filtration. However, the visual appearance of the suspension changed from a cloudy brown to a clear brown upon filtration. The small decrease in diameter from intensity to number basis argues against the presence of large outlier particles. So, this change in appearance may be due to removal of particles or micelles larger than the sensitivity of the DLS instrument. When the DLS measurement was repeated on C_{60}-1

during the total scattering experiment, the size distribution was very similar to those taken during the transient absorption spectroscopy experiments.

The C_{60}-2 colloidal suspension had a very similar size distribution to that of C_{60}-1, despite having a significantly different synthesis method.

The C_{60}-3 colloidal suspension had a much smaller size distribution than the other two colloid samples. Some contaminant particles in the size regimes of 200 nm and 5 μm were present in the DLS data and agglomerates of about 75 nm diameter were found via TEM observation. Note in the TEM images that the agglomerates seem to be made up of round particles on the order of 6-10 nm in diameter. However, the DLS intensity distribution is dominated by the smallest particles, which indicates that the concentration of the contaminant particles is low.

Plots of the DLS particle size distributions for the data shown in Table 3-1 are included in Appendix A.

3.2.3. Nanoparticle Tracking Analysis

Nanoparticle tracking analysis is another particle sizing technique, in which video of scattered light from particles moving under Brownian motion is recorded and analyzed to track the movements of each individual particle.

3.2.3.1. Experimental Technique

In the Nanoparticle Tracking Analysis (NTA) technique, a very thin cell is filled with a very dilute suspension of particles. This cell is viewed through a microscope by a high resolution camera. The bottom of the cell is a glass block with very high optical

density to provide high contrast to the microscope. A continuous wave laser is introduced into the sample, skimming almost parallel to the top window, transverse to the optical axis of the microscope objective. Although the particles are too small to be resolved optically, laser light scattered from them is viewed by the microscope and appears as bright dots on the camera's focal plane. Video is recorded of these bright spots, which move according to the Brownian motion of the particles. Software is used to track each particle individually over a period of time. From the observed Brownian motion, the software calculates the estimated hydrodynamic radius of each particle and amasses a particle size distribution based on all of the particles viewed.

3.2.3.2. Results and Discussion

One of the chief advantages of the NTA technique is that the native basis for the particle size distribution is number density. Therefore, it is not subject to the errors that can be introduced when converting DLS intensity-based data to volume and number based distributions. However, the sample volume for NTA is very much smaller than DLS, so fewer particles are examined. The largest particle size that the NTA technique can measure is 1 μm. Also, the smallest particle size that the NTA technique can measure is a function of the brightness of the light reflected from the smallest particles and the camera's ability to distinguish this from the background. This in turn is a function of the difference between the refractive index of the particles and the liquid, as well as the magnitude of the particles' absorbance. For the types of particles investigated here, the NTA technique had difficulty resolving with confidence particle sizes below about 50 nm in diameter. These factors must be considered when evaluating the NTA

particle size data in Table 3-2, below. (Note that the estimated concentration is based on the highly diluted samples used in the NTA instrument, not the concentrations used in the experiments.)

Table 3-2. Particle Size Distribution Statistics from NTA Measurements.

Sample Description	Mean (nm)	Mode (nm)	Standard Deviation (nm)	Cumulative Under Size			Estimated Concentration (particles/mL)
				D10 (nm)	D50 (nm)	D90 (nm)	
CBS-1	143	89	78	62	123	256	1.3×10^8
CBS-2	151	127	80	71	133	256	0.93×10^8
C_{60}-1	100	67	66	44	81	173	2.7×10^8
C_{60}-2	106	74	65	52	88	175	1.92×10^8
C_{60}-3	157	80	96	66	133	274	1.67×10^8

The average particle diameter for CBS-1 on a number distribution basis measured by DLS is about 35 nm. This is beneath the response of the NTA instrument, and thus the NTA measurements for this sample picks up mainly the contaminant particles with sizes around 100 nm.

The DLS data for CBS-2 indicated a bimodal distribution. Since the larger particles detected by DLS are beyond the range of the NTA instrument, the NTA particle size distribution for this sample picks up mainly the particles slightly larger than 100 nm.

The mode of the NTA particle size distribution for C_{60}-1 agrees quite well with the number distribution data given by DLS.

Likewise, the mode of the NTA particle size distribution for C_{60}-2 agrees quite well with the average particle size by number distribution given by DLS.

The DLS data for C_{60}-3 indicated a preponderance of particles of about 6 nm diameter. This is well below the sensitivity of the NTA instrument, so the NTA distribution for this sample consists mainly of contaminant particles larger than 100 nm.

Although there is some disagreement between the DLS and NTA measurements, the particle size distributions within the optimal range of the NTA instrument do coincide quite well with the DLS measurements, and the differences in the other measurements are explainable.

Plots of the NTA particle size distributions for the data shown in Table 3-2 are included in Appendix A.

3.2.4. Ground State Absorption Spectra

3.2.4.1. Experimental Technique

Ground state UV-Vis absorption spectra were measured in a spectrophotometer in either a 1 mm or 2 mm path length quartz cuvette. Measurements are of internal absorbance or transmittance; the data have been corrected for Fresnel reflection loss.

3.2.4.2. Results and Discussion

Figure 3-5 shows the quantified ground state absorbance spectra of the C_{60}-1 colloidal suspension compared to C_{60} in toluene. The C_{60} in toluene spectrum shows the typical characteristics of a C_{60} solution: a strong absorption peak around 330 nm, a smaller peak around 410 nm that corresponds to vibronic interactions with the liquid, and a broad absorption band between 500 and 600 nm.[10] The spectrum of the colloidal C_{60} suspension shows a broad peak around 450 nm that has been attributed to the formation

of C_{60} colloids.[94] Comparing the two spectra, the band appearing at 336 nm in the C_{60} in toluene solution has shifted slightly to 342 nm in the colloidal suspension. This absorption band is known to be affected by its environment and this red-shift suggests that the Triton X-100:water solution has stabilized the C_{60} slightly more than the toluene.[117] In addition, the overall absorption of this band has reduced in magnitude in the Triton X-100:water suspension compared to the toluene solution. The band at 450 nm has been previously reported and attributed to aggregation of C_{60} within the Triton X-100 micelle.[94, 95, 117, 118] The amount of aggregation is highly dependent on the preparation method of the colloidal suspension.[79, 88, 119, 120] In the literature, Bensasson et al. found that preparation of the C_{60} micelles under nitrogen (ε_{450nm} = 2100 M^{-1} cm^{-1}) or oxygen (ε_{450nm} = 12180 M^{-1} cm^{-1}) led to different degrees of aggregation and that under certain synthesis conditions, it was possible for C_{60} to be very highly solubilized by Triton X-100 such that there was little or no aggregation within micelles.[117] The C_{60}-1 sample was prepared under air-saturated conditions and had a molar extinction coefficient of $\varepsilon_{450\ nm}$ = 4350 M^{-1} cm^{-1} (as prepared for the transient absorption spectroscopy measurements). When this experimental ε is plotted with the values from Bensasson versus percentage of oxygen (0, 21, 100), a linear fit is obtained. This indicates that preparation of these samples under varying oxygen concentrations allows tuning of the amount of colloidal C_{60} micelles present. Thus, the sample may consist of a mixed colloidal suspension of both micelles with monomeric C_{60} and micelles containing colloidal particles of many C_{60} molecules.[117] The possibility that the mixture contains free C_{60} can be ruled out due to its very low solubility in water.[121-123] Also of note is the

small bump observed at 615 nm in the colloidal suspension, which is consistent with the absorption peak observed at 599 nm for C_{60} in toluene. (Inset of Figure 3-5.) This red-shift is also consistent with a greater stabilization of the energy by the colloidal suspension than the toluene solution. Overall, the ground state absorption spectrum of C_{60}-1 appears to be consistent with literature reports of colloidal C_{60} spectra and which some authors attribute to a mixed absorption from monomeric micelles and colloidal micelles.

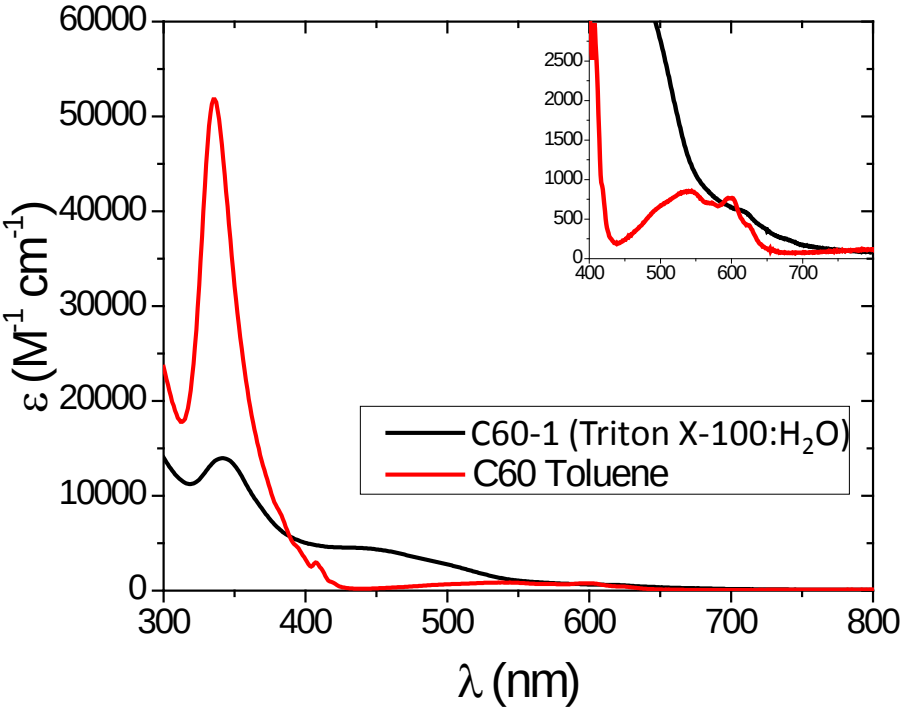

Figure 3-5. Quantified Ground State Absorbance Spectra of C_{60}-1 Suspension and C_{60} Solution in Toluene.

Figure 3-6 shows the ground state absorbance spectra of the samples used in the total scattering experiment. These samples were normalized to each have an internal

transmittance of 70% through a path length of 2 mm at 560 nm, which was the pump wavelength for the total scattering study. The CBS-1 and CBS-2 have a gently rolling featureless absorption spectrum that has the character typical of carbon black nanoparticles. The C_{60} in toluene spectrum is as discussed above, as is the spectrum of C_{60}-1. The C_{60}-2 spectrum is very similar to that of C_{60}-1. However, for the same transmittance at 560 nm, the absorption peaks around 330 nm and 450 nm are slightly more pronounced in the C_{60}-2 sample than in C_{60}-1. This may indicate a higher concentration of both monomeric and (smaller) colloidal C_{60} in the C_{60}-2 sample. The C_{60}-3 spectrum is quite smooth with barely perceptible absorption features near 330 nm and 450 nm. This spectrum closely resembles the spectrum for C_{60} in a completely colloidal state published by Eastoe et al.[96]

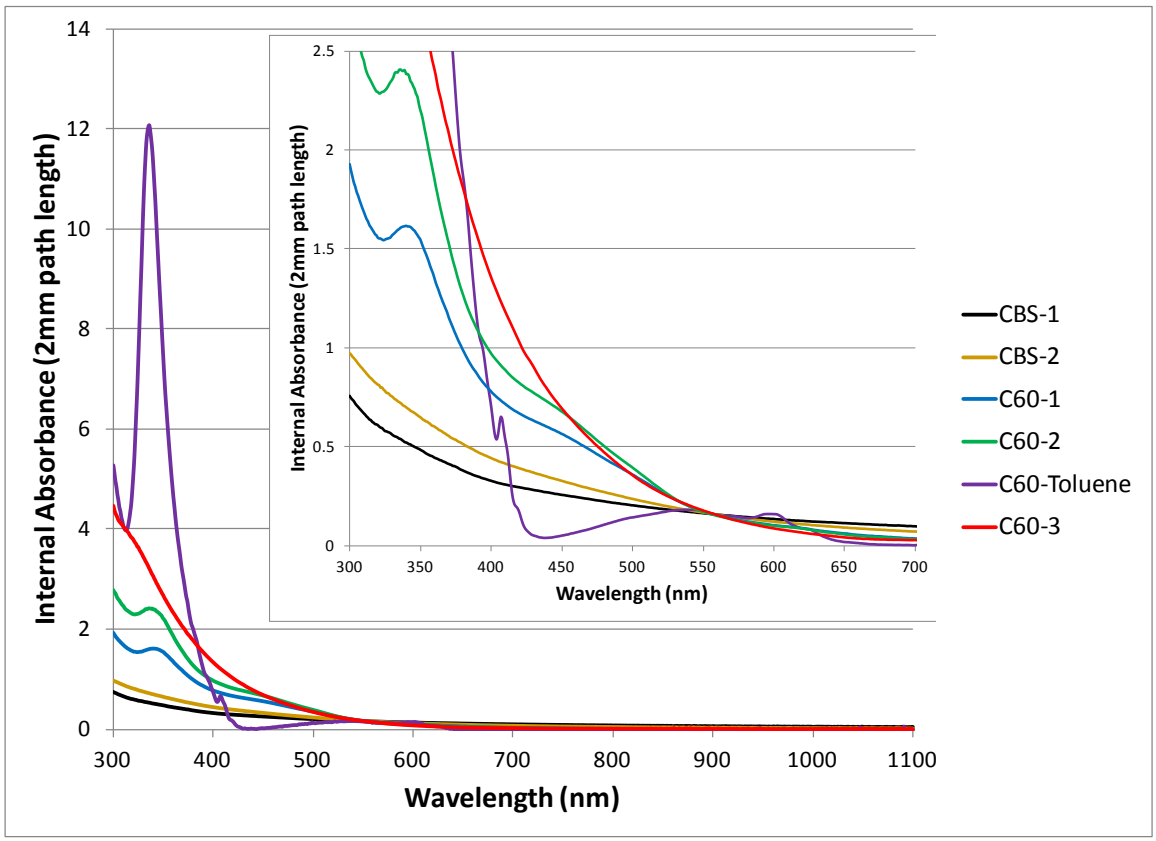

Figure 3-6. Ground State Absorption Spectra of Total Scattering Samples.

Figure 3-7 re-plots the above data for the total scattering samples in terms of percent transmittance. As the shapes of the transmittance curves would indicate, the C_{60} in toluene solution has a purple appearance, while the C_{60} colloid suspensions have an amber appearance and the carbon black suspensions appear brown.

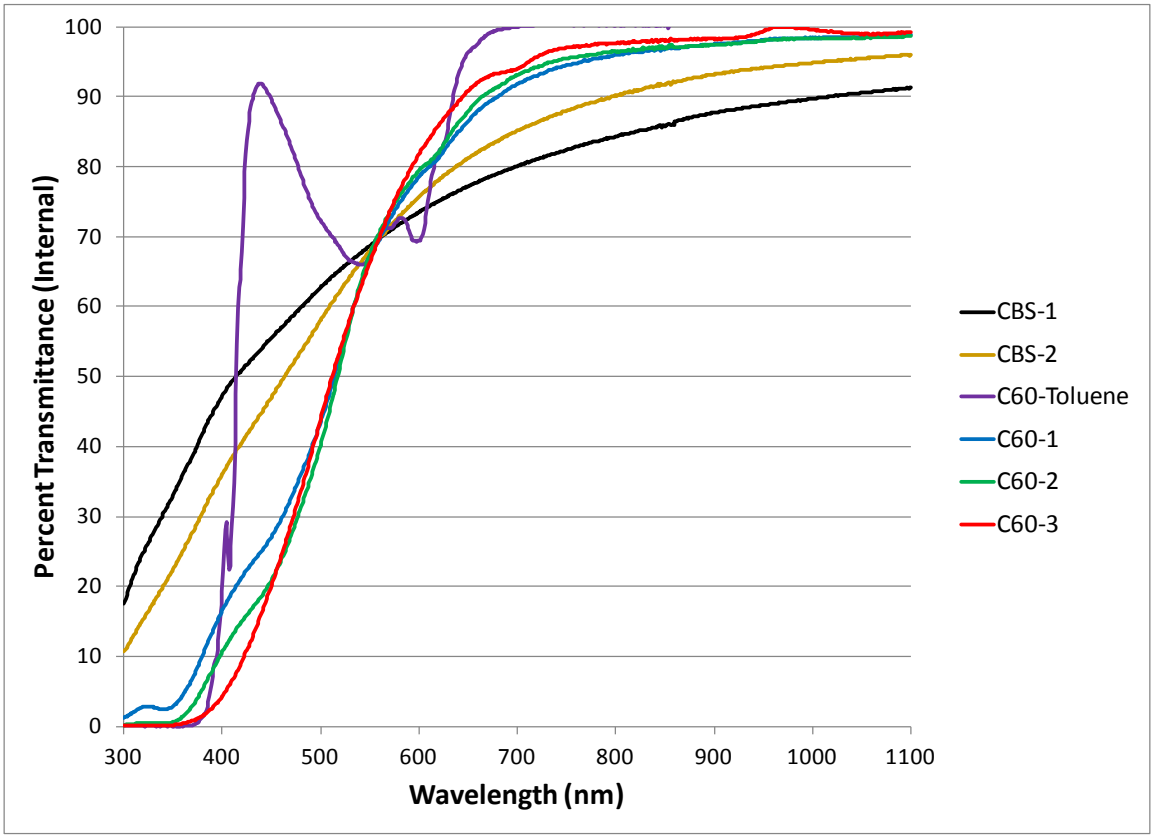

Figure 3-7. Internal Percent Transmittance Spectra of Total Scattering Samples.

CHAPTER 4: TRANSIENT ABSORPTION SPECTROSCOPY STUDY

4.1. Introduction

Transient absorption spectroscopy refers to a suite of measurement techniques in which a sample material with nonlinear optical properties is excited with a pump pulse and probed with a broadband light source such that the spectrum of the change in the material's absorbance is measured as a function of time. One fine distinction to make is that what is really measured in these experiments is the change in transmittance of the material and that both absorption and scattering can contribute to the reduction in transmittance. However, the term transient absorption spectroscopy is in common use and these techniques are most often applied to materials whose responses are dominated by nonlinear absorption—in particular, reverse saturable absorbers (RSAs).

RSA is a special case of excited state absorption (ESA) in which the absorption cross-section of the excited state is much larger than the absorption cross-section of the ground state, resulting in a decrease in transmittance with increasing input irradiance. RSA behavior is typically described by a five-level Jablonski diagram, as depicted in Figure 4-1.

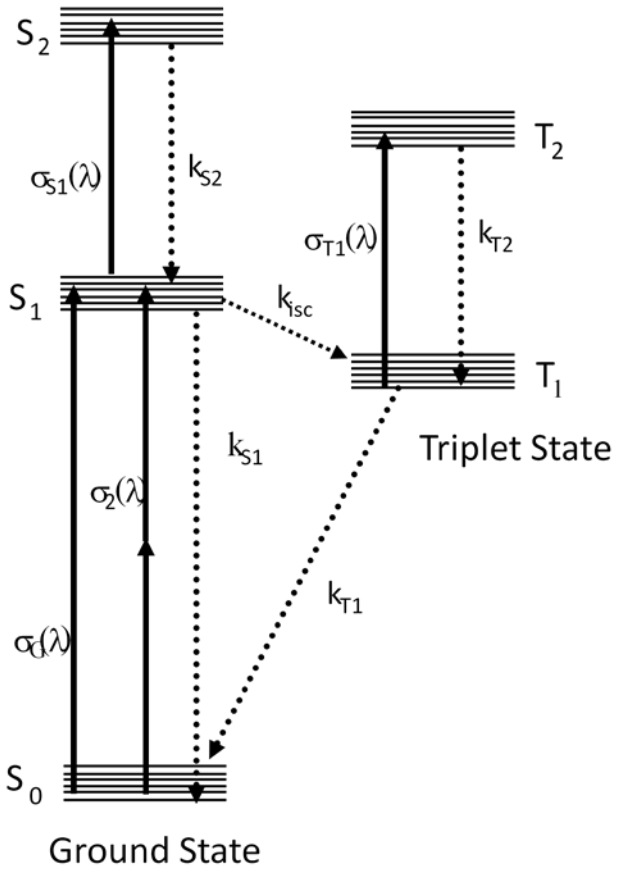

Figure 4-1. Jablonski Diagram Describing Reverse Saturable Absorption (RSA).

In the above diagram, k_{s1} is the rate associated with fluorescence and internal conversion (heat) from the first excited singlet state, k_{s2} is the decay rate from the upper excited singlet states back to S_1 (which is typically less than 1 ps), k_{isc} is the intersystem crossing rate from S_1 to T_1, k_{T1} is the decay rate from the first excited triplet state to the ground state, k_{T2} is the decay rate from the upper excited triplet states back to the first excited triplet state (which is typically less than 1 ps), σ_G is the ground state absorption cross-section, σ_2 is the two-photon absorption cross-section, σ_{S1} is the absorption cross-section of the first excited singlet state, and σ_{T1} is the absorption cross-section of the first

excited triplet state. Not shown directly on the diagram is k_{SQ}, the rate associated with quenching (depopulating the first excited singlet state as a result of interactions with other nearby molecules). The total decay from the first excited singlet state is k_S, which is simply the addition of k_{S1}, k_{ISC}, and k_{SQ}. The inverse of each of the above rates is the corresponding lifetime, and is represented by the character, τ.

At any instant and spatial location, the absorption is dictated by the population densities and the absorption cross-sections of each of these five energy bands. The dynamics of the population densities are related by a set of rate equations that take into account the absorption cross-sections of the optical transitions and the decay rates between bands. Transient absorption spectroscopy techniques are a means of experimentally obtaining the lifetimes and absorption cross-sections used in the rate equations.

Femtosecond pump-probe experiments have ultrafast resolution and are used primarily to determine the time-resolved spectra and kinetics of the first excited singlet state. Nanosecond flash photolysis is used to determine the time-resolved spectra and kinetics of the first excited triplet state, which is typically long-lived.

4.2. Femtosecond Pump-Probe Transient Absorption Spectroscopy

This experiment is used to measure the absorption spectrum and the relaxation kinetics of the first excited singlet state. The material under study is pumped with a femtosecond laser pulse to excite a significant amount of its valence electron population into the first excited singlet state. It is probed with a very low energy femtosecond white

light pulse, which is measured by a spectrometer over several optical delays on the picosecond timescale. When the material is unexcited, the absorption spectrum measured by the spectrometer corresponds to the ground state. When the material is pumped hard enough to drive a significant amount of the population into the first excited singlet state, its absorption spectrum changes. Since photons are being absorbed from both the ground state and the first excited singlet state, the absorption spectrum is a combination of the ground state and first excited singlet spectra. The absorption spectrum due to the first excited singlet state is found by subtracting the new absorption spectrum from the ground state spectrum. This is why the differential absorption spectrum is plotted.

Over time, the electron population decays from the first excited singlet state by means of several processes. As this happens, the differential absorption spectrum gradually fades. By fitting the temporal decay of the differential absorption spectrum, one can determine one or more time constants which correspond to the mechanisms by which the population is decaying from the first excited singlet state. Since the inter-system crossing lifetime to the triplet manifold is typically on the order of a nanosecond and the time delays considered in the femtosecond pump-probe experiment are on the order of picoseconds, this experiment is able to isolate the spectrum and kinetics associated with the singlet state.

4.2.1. Experimental Technique

A Ti:sapphire laser was used to generate 170 fs (FWHM) pulses at a 500 Hz repetition rate at a wavelength of 780 nm. The energy per pulse was approximately 1 mJ. A pulse-picking shutter was used to select a single pulse from this pulse train. A beam

splitter was used to divide this output into a pump and a probe beam. The pump beam was frequency doubled to 390 nm and focused into the sample, which was contained in a quartz cuvette with a 2 mm path length. The probe beam traversed a computer-controlled optical delay and was focused into a sapphire plate, generating a white light continuum. The white light probe beam was focused into the sample at near normal incidence such that the focal spots of the pump beam and probe beam overlapped. The transmitted probe beam was focused to a CCD spectrometer (see Figure 4-2). A transmittance spectrum was obtained for several values of optical delay. Combining these results elucidates the time evolution of the transmittance spectrum in response to the pump pulse. These results were then analyzed to determine the kinetics of the optical absorption processes. The data for this experiment are plotted in terms of the change in absorbance (ΔA) as a function of the probe wavelength. Again, the terminology “absorbance” is used here in keeping with common practice, but the reader is reminded that when scattering is present, this also affects the change in transmittance.

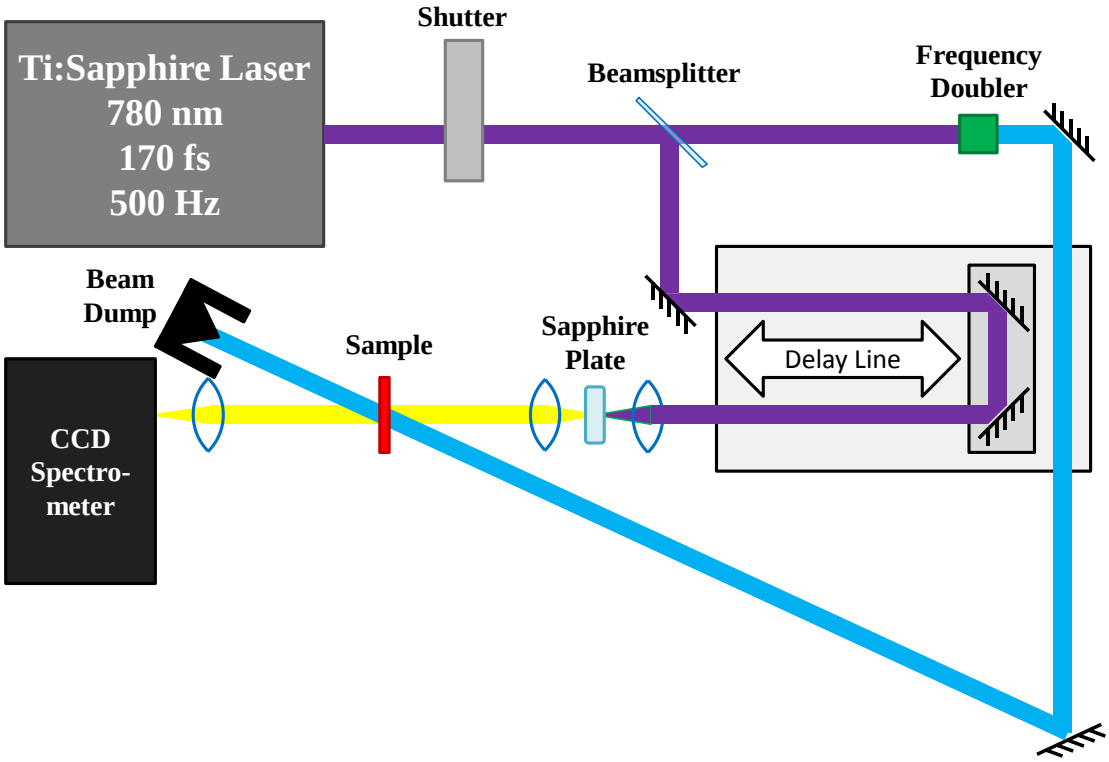

Figure 4-2. Femtosecond Pump-Probe Apparatus.

4.2.2. Results and Discussion

Femtosecond transient absorption measurements for a sample of C_{60}-1 in air-saturated 15:85 Triton X-100:water (diluted to 988 μM) are shown in Figure 4-3 for probe pulse delays of 0 to 6590 ps. The kinetic lifetimes of the excited state absorption processes in the ultrafast regime were determined using a multi-exponential fit and are given in Table 4-1. A sample of 938 μM C_{60} in air-saturated toluene was prepared for comparison. Femtosecond transient absorption measurements for this sample are shown

in Figure 4-4 and the kinetic lifetimes are given in Table 4-1. The results for C_{60} in toluene are consistent with what has been reported in the literature.[10]

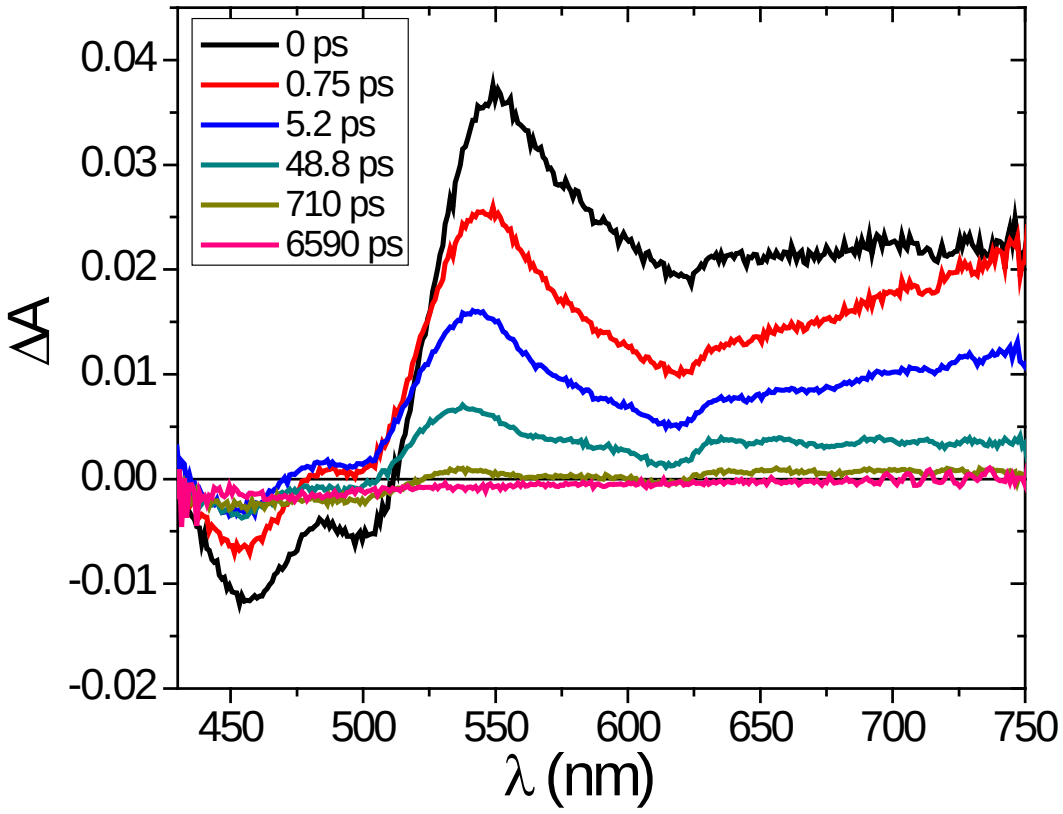

Figure 4-3. Femtosecond Pump-Probe Data for C_{60}-1.

Table 4-1. Transient Absorption Lifetimes.

	C_{60}-1 Colloid Suspension	C_{60} in Toluene	C_{60} Solid Film	Process
τ_{S2}	0.53 ± 0.28 ps	0.58 ± 0.52 ps	0.26 ps	Intramolecular vibrational relaxation
τ_{SR}	5.3 ± 1.8 ps	8.0 ± 4.7 ps	4.6 ps	Solvent reorganization
τ_{S}	42.6 ± 13.2 ps	960 ± 380 ps	64 ps	Self-quenching or singlet-singlet

				annihilation / Inter-system crossing
τ_{T1}	1.1 ms (from air sat LFP) 86 ms (from deoxy LFP)	333 ns (air sat LFP) 3.7 ms (deoxy LFP)	N/A	Long-lived Triplet excited state

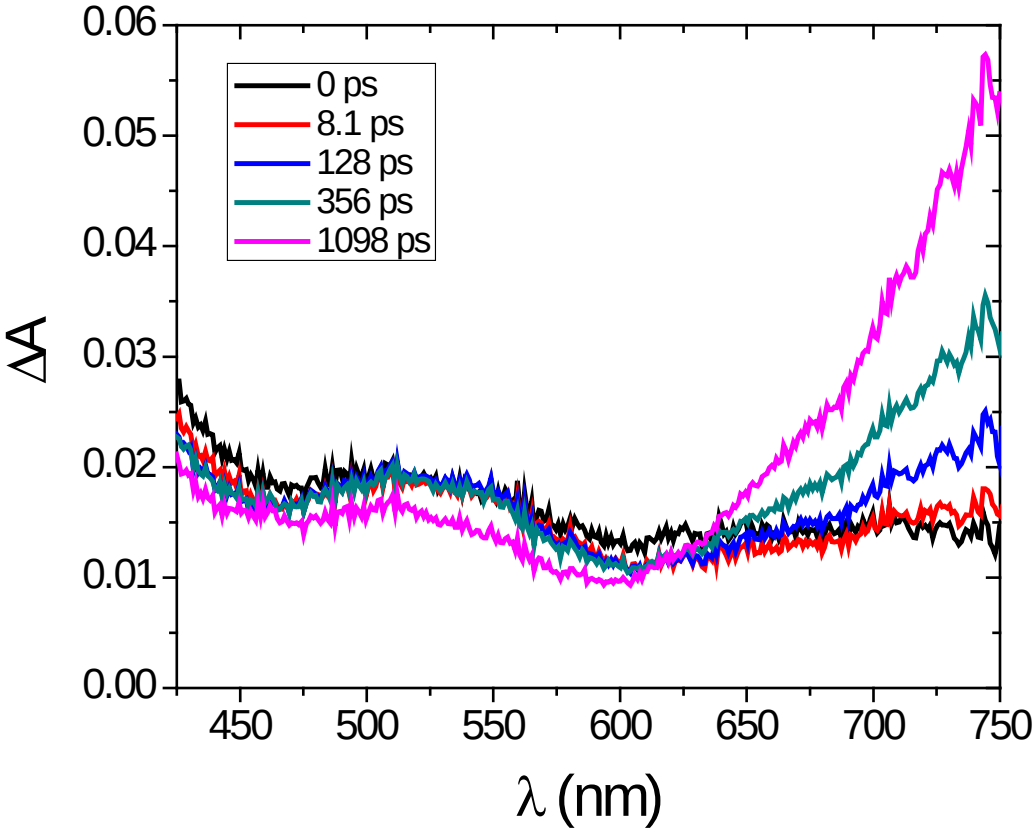

Figure 4-4. Femtosecond Pump-Probe Data for C_{60} in Toluene.

Spectrally, the two materials appear quite different. Both spectra are somewhat broadband. C_{60}-1 has a peak near 550 nm and slight bleaching near 450 nm. C_{60} in toluene has a minimum near 600 nm and a pronounced peak near 740 nm. This difference in spectra indicates that the distribution of the band of higher singlet excited states is quite different in the two materials.

The C_{60} in toluene solution first exhibits a fast decay of 0.58 ps, which is likely due to intramolecular vibrational relaxation (IVR). The photon energy of the pump pulse at 390 nm is larger than the ground state band gap, so electronic and vibrational levels higher than the S_1 state are briefly populated. Relaxation from these levels usually occurs within 1 ps. The C_{60}-1 suspension had a very similar initial decay rate, attributed to the same processes.

The second decay of 8.0 ps in the C_{60} in toluene solution is consistent with solvent reorganization around the C_{60} molecule. The second delay in the C_{60}-1 sample was 5.3 ps, which is attributed to the same type of process. Since the first two decays are so similar, it appears that the aggregation of the C_{60} colloids has no effect on these processes.

The third decay exhibited by C_{60} in toluene is due to formation of the triplet excited state via intersystem crossing, which is well known in the literature to be 1200 ps.[10] The value obtained by fitting the femtosecond pump-probe data is within experimental error of this amount. The third decay exhibited by the C_{60}-1 sample was 42.6 ps, which is significantly shorter than that of the C_{60} in toluene solution. The shortening of this decay is attributed to quenching of the singlet excited state through either a self-quenching process or singlet-singlet annihilation, analogous to the quenching processes reported in the literature for solid films of C_{60}.[15, 124] The close proximity of C_{60} molecules within aggregates inside of the micelles argues against any slow diffusional processes and instead results in very efficient quenching of the C_{60} singlet excited state.

Ultrafast transient absorption studies on thin films of C_{60} have been reported in the literature.[31, 125] These studies revealed spectral properties similar to those shown in Figure 4-3. In both cases, the authors describe the transient absorption as coming from formation of a singlet exciton. In addition, a study on a C_{60} film excited at 633 nm resulted in three lifetimes of τ_{S2} = 0.26 ps, τ_{SR} = 4.6 ps, and τ_S = 64 ps,[29] which are similar to the decays calculated for the C_{60}-1 colloidal sample. Thus, colloidal C_{60} appears to act very similar to C_{60} solid films.

A long-lived absorption tail was observed for the C_{60} in toluene solution, with its peak at 740 nm, which is consistent with the known triplet excited state absorption of C_{60}.[10] A long-lived absorption tail was also measured for the C_{60}-1 sample. This absorption tail might be due to formation of a triplet excited state or formation of reduced C_{60} ($C_{60}^{\cdot -}$) in a self-quenching reaction.[110] The spectrum at this probe delay is not consistent with triplet C_{60}, but the weak absorption signal was near the limit of detection. Reduced C_{60} has a characteristic absorption feature at 1070 nm. However, since the femtosecond pump-probe apparatus was unable to measure beyond 800 nm, the presence or absence of reduced C_{60} could not be confirmed. It is also possible that the reduced transmittance at these long delays might be due to scattering processes.

Overall, the femtosecond data reveal that a quenching process is occurring in the C_{60} colloidal sample at a fast rate, nearly eliminating intersystem crossing to the triplet excited state. Using the lifetimes collected, the following calculation was performed to estimate the fraction of singlet excited state quenched. Assuming a pseudo first order rate and knowing the k_{obs} value of the colloidal sample is 2.3 x 10^{10} s^{-1} (1/42.6 ps), k_d is

1.0 x 10^9 s^{-1} (1/960 ps) from the C_{60} in toluene, and the concentration of quencher is 988 μM (i.e. the concentration of C_{60} in the diluted suspension), the following equation determines the rate constant for quenching k_q (M^{-1} s^{-1}) to be 2.2 x 10^{13} M^{-1} s^{-1}.

$$k_{obs} = k_d + k_q[Q]$$

This rate constant is orders of magnitude faster than a typical diffusion controlled rate constant of 1 x 10^9 M^{-1} s^{-1} and may be attributed to the close packing of the C_{60} molecules within the micelles. Using this calculation, the estimated fraction of singlet excited states quenched in the C_{60}-1 sample is 95.6%. Therefore, only about 4.4% of the singlet excited states can participate in excited state triplet absorption via intersystem crossing in the C_{60}-1 sample.

4.3. Nanosecond Laser Flash Photolysis

This experiment is used to determine the absorption spectrum and relaxation kinetics of the first excited triplet state. The name of the experiment is a slight misnomer. The term “photolysis” literally means the chemical decomposition of materials under the influence of light. In this usage, the materials are being excited by light, but not necessarily decomposed. The experiment is very similar to the femtosecond pump-probe experiment, except that nanosecond pulses are used. Since singlet states are typically short-lived and probe delays in the nanosecond flash photolysis experiment are on the order of tens of nanoseconds, the differential absorption spectrum corresponds to the valence electron population that has been populated to the first excited triplet state via

inter-system crossing. Likewise, the decay of this differential absorption spectrum corresponds to the kinetics of the depopulation of the first excited triplet state.

4.3.1. Experimental Technique

Nanosecond transient absorption measurements were carried out using the third harmonic (355 nm) of a Q-switched Nd:YAG laser. A pulse-picking shutter was used to select a single pulse from a repetitive pulse train for good shot-to-shot energy stability. The pump beam was expanded to present a uniform irradiance to the sample. The pulse width was approximately 5 ns FWHM. Pulse fluences of up to 8 mJ cm^{-2} at the excitation wavelength were typically used. The sample was placed in a 1 cm square quartz cuvette. The pump pulse induces a time-dependent change in the sample's transmittance spectrum. To measure the change in the sample's transmittance, a 75 W continuous wave xenon lamp was focused through the sample transverse to the pump beam and reimaged onto the entrance slit of a monochromator. A pair of shutters was used to gate the white light from the xenon lamp. A filter was placed before the sample in the probe path to adjust the white light's irradiance so that it would not perturb the sample by itself. A neutral density filter wheel was used to adjust the irradiance of the white light transmitted through the sample to the monochromator's sensitivity range. A photomultiplier tube (PMT) detects the transmitted signal for a single wavelength. The current from the photomultiplier tube goes through a back-off circuit which subtracts the signal due to the background irradiance and passes it to a digital oscilloscope, which records the entire pulse with high temporal resolution. The monochromator is tuned to a new wavelength and the process is repeated. Thus, the laser-perturbed changes in the

transmittance spectrum are captured as a function of time. The sample cuvette was masked so that the xenon light only passed through it just inside the pump beam input window so that it would not probe the sample at a depth at which the pump beam had been partially depleted by the sample.[126] (See Figure 4-5.) The amassed data is analyzed at prominent spectral features to extract multiple exponential time constants related to the physical processes responsible for the changes in the spectrum.

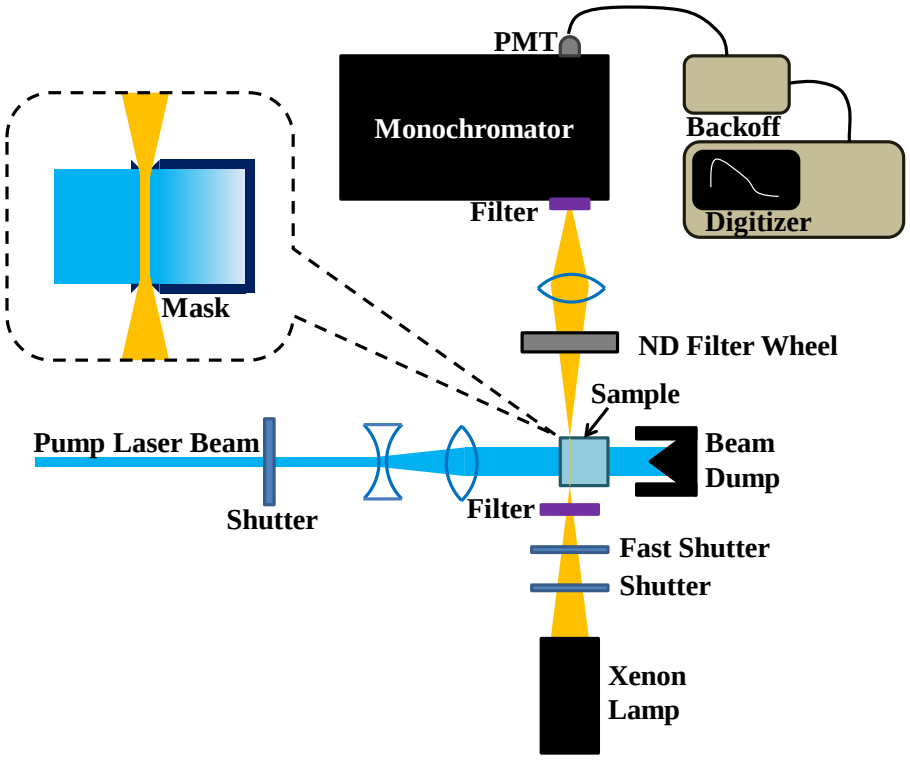

Figure 4-5. Nanosecond Laser Flash Photolysis Apparatus.

4.3.2. Results and Discussion

Nanosecond laser flash photolysis studies were performed on both the C_{60}-1 colloidal suspension and a solution of C_{60} in toluene. The samples were prepared with a matched optical density (OD) at the excitation wavelength of 355 nm so that the overall absorption could be compared between the two samples. For both samples, data was taken under both air-saturated and deoxygenated conditions.

Figure 4-6 shows the differential absorbance immediately following the laser pulse for 17.0 μM C_{60} in air-saturated toluene and 44.1 μM C_{60} in air-saturated 15:85 Triton X-100:water (C_{60}-1). The decay lifetimes are given in Table 4-1. The shapes of the spectra are nearly identical with only a small shift in the peak. The magnitude of the change in absorbance, ΔA, however, is markedly different. With a matched optical density (OD) at the exciting wavelength, the same number of singlet excited states is produced in each sample. However, in the C_{60}-1 suspension, the ΔA at the peak of the spectrum is 0.006, whereas for C_{60} in toluene the ΔA is 0.143 at the peak. This 96% lower magnitude in the change of absorbance in the C_{60}-1 as compared to the solution of C_{60} in toluene is consistent with the estimate above of the fraction of excited singlet states quenched (95.6%). Therefore, there is still a small percentage (~4%) of C_{60} singlet excited states undergoing intersystem crossing to the triplet excited state.

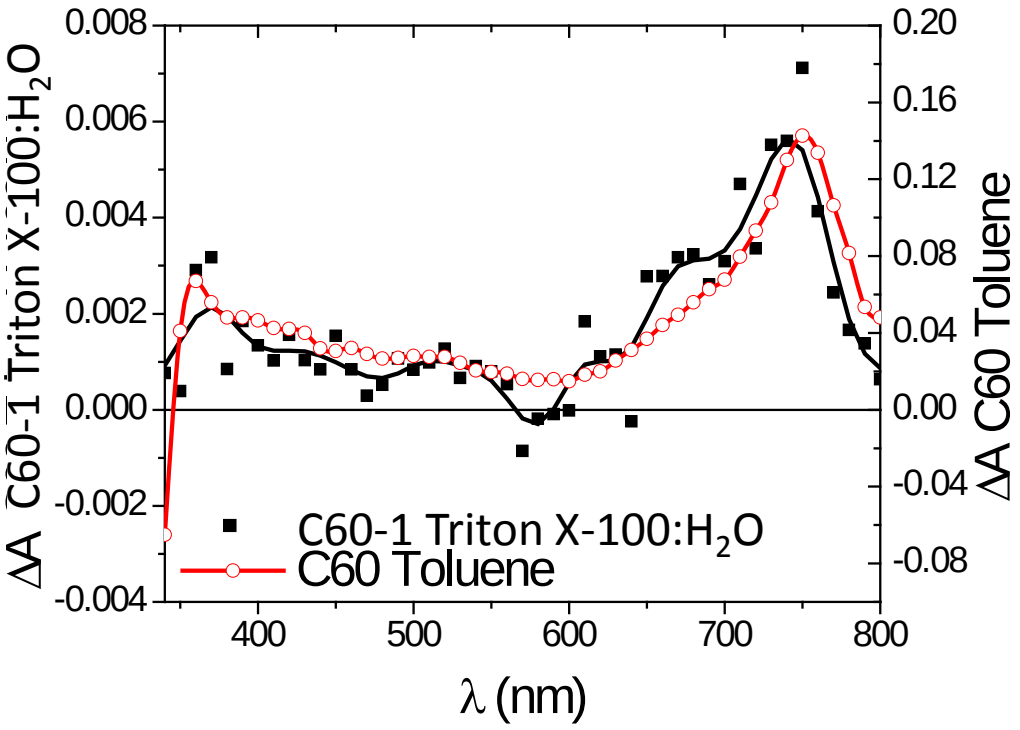

Figure 4-6. Laser Flash Photolysis of C_{60}-1 Suspension and C_{60} in Toluene.

Unlike the air-saturated sample, the laser flash photolysis data for C_{60} in deoxygenated 15:85 Triton X-100:water (C_{60}-1) did not result in a measureable spectrum; the only discernible signal appeared at 740 nm. From the weak 740 nm peak, a lifetime of 86 μs was determined for the deoxygenated sample. The sample was deoxygenated via three freeze-pump-thaw cycles. The ground state absorption spectrum was carefully monitored before and after deoxygenation and there were no significant changes—particularly in the broad region near 450 nm which is attributed to the presence of the colloidal particles—indicating that the sample had not changed. One possible explanation for this observation may be that there is a slight competition by trapped

oxygen to quench the singlet excited states. In other words, the rate of oxygen quenching of singlet C_{60} is much slower than the rapid self-quenching resulting from the close proximity of the C_{60} molecules, but it remains a competitive pathway under air-saturated conditions. Upon removal of this competitive reaction, the faster self-quenching pathway depletes the singlet excited states much more efficiently (to > 96%), reducing the number of singlet excited states that intersystem cross to the triplet excited state.

Nanosecond laser flash photolysis was also conducted for the C_{60}-2 colloidal suspension. Spectrally, the results were nearly identical to the C_{60}-1 sample, as shown in Figure 4-7. The lifetime of the long absorption tail was found to be 1.1 μs, in agreement with C_{60}-1. The concentration was not known with confidence, so conclusions cannot be drawn based upon the magnitude of the curve.

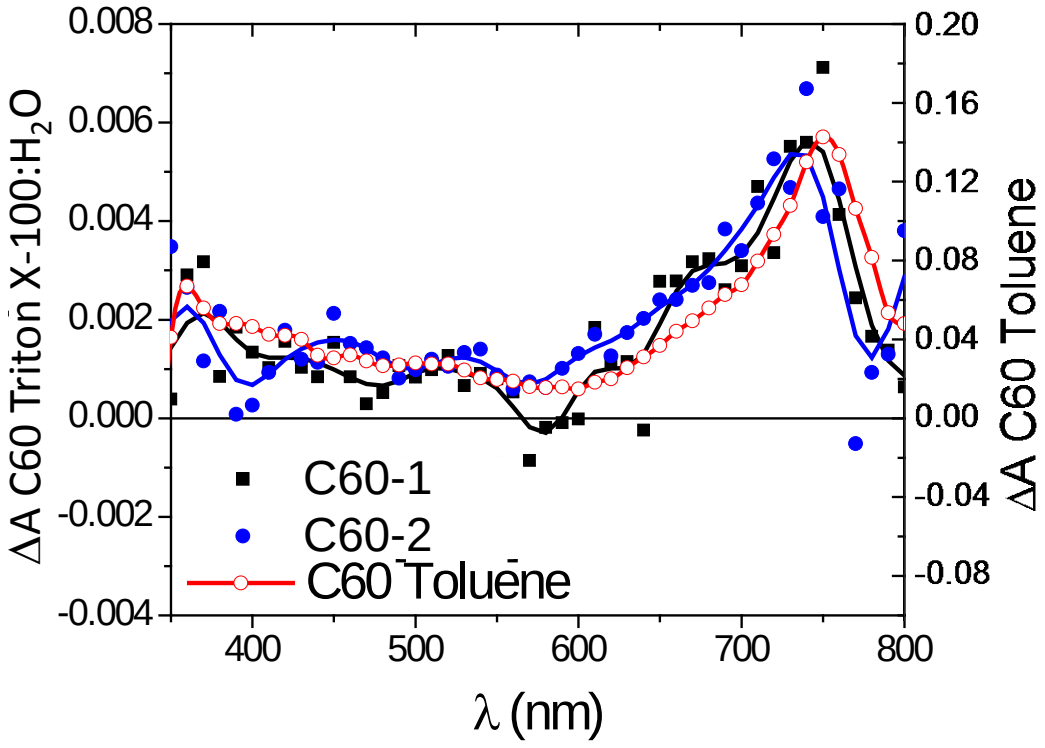

Figure 4-7. Laser Flash Photolysis Data for C_{60}-1, C_{60}-2, and C_{60} in Toluene.

Finally, at a later time, nanosecond laser flash photolysis was conducted for the C_{60}-3 colloidal suspension. Figure 4-8 shows the differential absorbance spectra of the sample at two different input energies of similar magnitude to the previous laser flash photolysis data. The shape of these spectra is similar to that of the previous colloidal C_{60} suspensions, but blue-shifted in with a slightly broader peak. The magnitude of the peak is greater than the corresponding peak in the C_{60}-1 sample, but smaller than the C_{60} in toluene solution. This may indicate that the quenching processes responsible for inefficient intersystem crossing in the colloidal suspensions with larger particles (i.e.,

C_{60}-1) are less dominant in the C_{60}-3 sample. However, since the concentration was not noted, firm conclusions cannot be drawn based on the magnitude of these curves.

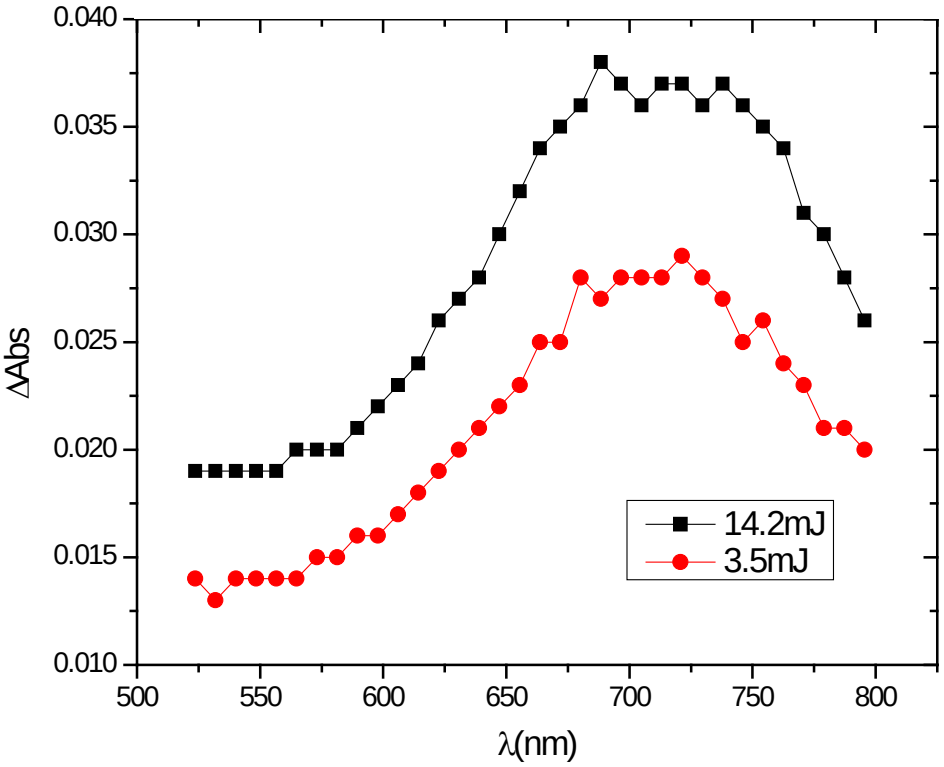

Figure 4-8. Laser Flash Photolysis Data for C_{60}-3 Suspension.

4.3.3. Conclusions

From the femtosecond pump-probe measurements, it appears that C_{60}-1 has decay rates very similar to the behavior of C_{60} solid films. There is evidence of strong quenching processes that make inter-system-crossing (ISC) to the first excited triplet state—which is extremely efficient in C_{60} molecular solutions—quite inefficient. The estimated triplet quantum yield for C_{60}-1 is 4.4%, compared to 96% for C_{60} in toluene.

On the nanosecond timescale, C_{60}-1, C_{60}-2, and C_{60}-3 all have nearly the same shape to the ΔA spectrum as C_{60} in toluene, indicating that in all cases there are at least some excited triplet states becoming populated as a result of ISC.

In the case of C_{60}-1, which was measured with careful attention paid to its concentration, the 96% lower magnitude in the ΔA peak near 740 nm indicates that only about 4% of the population in the first excited singlet state undergoes ISC to the first excited triplet state, which confirms the estimate of 4.4% triplet quantum yield based on the femtosecond measurements.

When C_{60}-1 was deoxygenated and re-measured, there was a slight signal near 740 nm with a very long decay time, but the rest of the spectrum was almost undetectable. This indicates that by removing the oxygen, the first excited singlet state quenching processes became more efficient. One interpretation to these results may be that in air-saturated conditions, there is a competing quenching process involving oxygen which is much slower than the self-quenching due to the close proximity of the C_{60} molecules to each other and that when this competing process is removed, the overall rate of quenching increases, resulting in much less ISC to the triplet state.

CHAPTER 5: Z-SCAN STUDY

5.1. Introduction

Z-scan is a standard technique for measuring nonlinear changes in the refractive index and the absorption of NLO materials.[127] This technique is widely used to characterize RSA materials and established treatments exist with which to analyze z-scan data in order to determine characteristic parameters, such as the triplet-triplet absorption cross section.[128] Although particle suspensions do show characteristic behaviors in the z-scan apparatus, no known method yet exists with which to extract characteristic parameters for carbon black suspensions from z-scan data. The z-scan technique was employed in this study to determine the RSA behaviors of C_{60}-1 and C_{60}-2, with C_{60} in toluene and CBS-1 used as reference samples.

5.2. Experimental Technique

The laser used in this experiment was an injection-seeded, frequency-doubled Nd:YAG laser operating at 532 nm with a pulse repetition rate of 10 Hz. When necessary, the beam was gated with a pulse-picking shutter. The laser had a high quality Gaussian spatial output, which is important when fitting z-scan data to theory. A beamsplitter, BS1, was used to reflect a portion of the incoming pulse as a reference beam with which to determine the input energy. A lens, L0, brought the reference beam to a partial focus onto a silicon energy detector, D1, so that all the energy was captured but the detector was not saturated by too tight of a focus. A neutral density filter, F1, was used to adjust the irradiance transmitted to the detector for the detector's optimal

dynamic range. The primary beam was focused by a near diffraction limited lens, L1, into the sample, S. A near diffraction limited lens, L2, was used to collect the transmitted light and partially focus it to a silicon energy detector, D2. A neutral density filter, F2, was used to adjust the transmitted irradiance to optimize the dynamic range of D2. Both detectors were read by an energy ratiometer, M1. The sample, S, was translated to different locations along the axis of propagation (the z-axis) and the transmittance of the sample measured. (See Figure 5-1.)

Although analysis methods do exist for thick samples, the analysis of z-scan data is more straightforward for thin samples whose path length is less than the Rayleigh range of the beam. The samples in this study were thin samples (1 mm path length). As the sample is scanned in and out of the focal region, the beam diameter—and thus the irradiance in the sample—changes. The resulting changes in transmittance as a function of z-position can thus be correlated to the irradiance at those positions.

When determining the nonlinear refractive properties of a sample, an aperture is placed at lens L2 to partially obscure the beam transmitted to detector D2. This is called a closed-aperture z-scan. Typically, this aperture is used to reduce the linear transmittance of the sample to 10% to 50% of its actual transmittance. If the sample undergoes nonlinear refraction, either more or less light will pass through the aperture, depending on the sign of the refractive index change. When this aperture is not in place (or fully open), all of the transmitted energy is collected by lens L2 and read by detector D2, so what is measured as a change in transmittance is due entirely to absorption. This is called an open-aperture z-scan. (The exception to this, of course, is strongly scattering

materials. Any light that is scattered outside of the collection aperture of lens L2 will also result in a lower transmittance.) Since any change in absorption is also present in the closed-aperture z-scan, both closed-aperture and open-aperture z-scans are done when one wishes to determine the nonlinear refractive parameters of a sample. Only an open-aperture z-scan is required to determine the nonlinear change in absorption. In this work, only open apertures z-scans were performed, since nonlinear refraction was expected to be negligible in these samples.

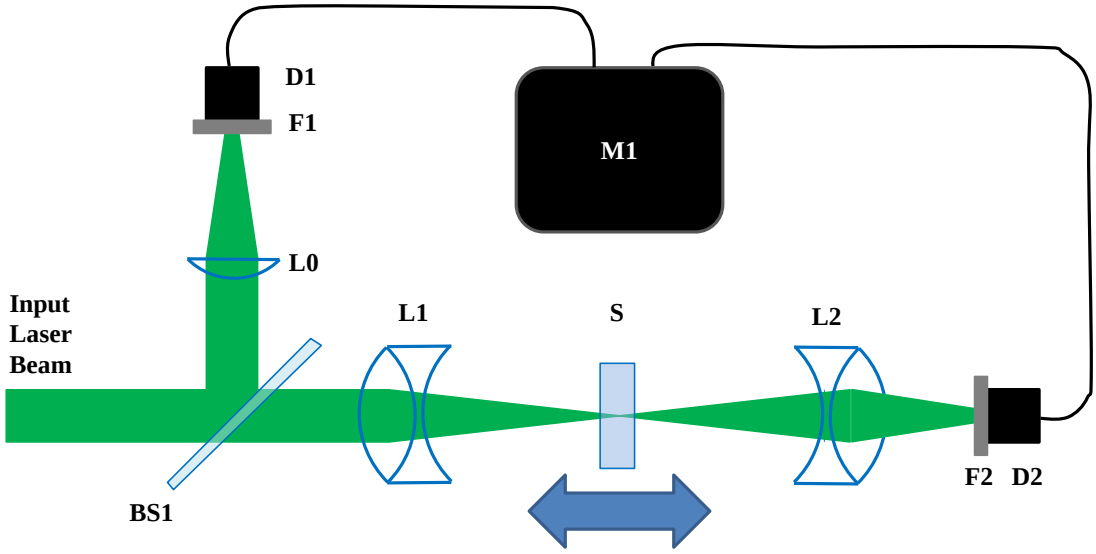

Figure 5-1. Z-Scan Apparatus.

5.3. Results and Discussion

Z-scans of a solution of C_{60} in toluene were performed as a baseline. A solution of 0.27 mg/mL of C_{60} in toluene was prepared and placed in a 1 mm path length quartz cuvette. An absorption coefficient of 0.696 cm^{-1} was measured at 532 nm in a

spectrophotometer. The sample was immersed in a sonicator bath for 30 minutes and re-measured. The absorption coefficient remained constant. The sample was placed at the focus of the z-scan experiment and the transmission of the sample was observed as a function of pulse number at both 10Hz and 1 Hz to make sure that there was no multiple shot bleaching of the material. Since there did not appear to be such an effect occurring with the C_{60} sample, multiple z-scans were taken at 10Hz, between energies of 0.26 – 2.41 μJ. The z-scans on C_{60} in toluene are shown in Figure 5-2. Each z-scan was background corrected and each point of the z-scan represents an average of 25 shots at each z-position. Simplified 3-level analysis of the 5-level RSA model was performed on the data as in Wood et al.[128] for each input energy and the average triplet-triplet absorption cross-section was determined to be 7.5×10^{18} cm^2, which is very close to the value of 8.1×10^{18} cm^2 measured previously by Ebbesen.[10]

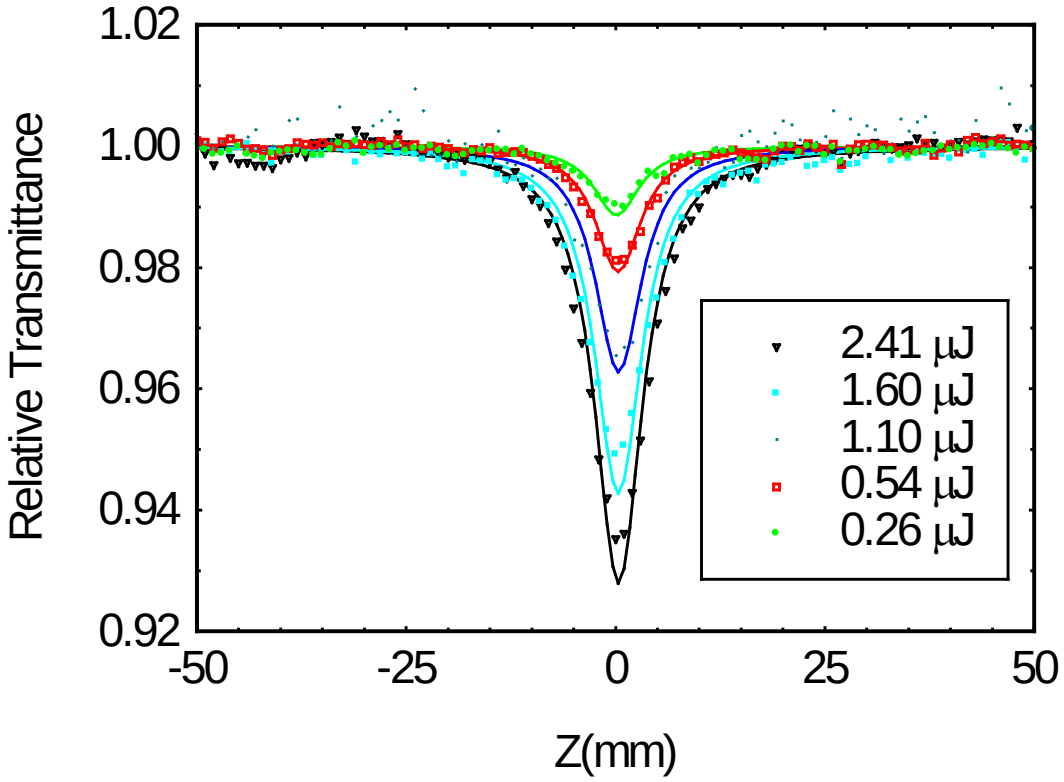

Figure 5-2. Z-Scan Data for C_{60} in Toluene.

Z-scans of acidified carbon black in water (CBS-1) were performed as a second baseline material. The nonlinear behavior of carbon black suspensions (CBS) is well documented and at nanoseconds is dominated by nonlinear scattering arising from the linear absorption of incident light, followed by rapid heating and ionization of the carbon particle within the timescale of the pulse width.[2, 6] Before irradiation, the suspended carbon black particles fall into the Rayleigh scattering regime. After scattering center formation, the remaining light in the pulse is scattered according to Mie scattering. Studies have shown that open aperture z-scans of carbon suspensions roughly resemble that of nonlinear absorbers.[8, 129] However, the resulting z-scans do not fit RSA analysis

and there is no known simple analysis from which to derive any photo-physical properties from such a z-scan. When a z-scan is performed on CBS, there is a characteristic dip of the transmitted irradiance, but the dip is much narrower than that of a reverse saturable absorber (RSA) or two photon absorber (TPA) material with the same change in transmitted irradiance.

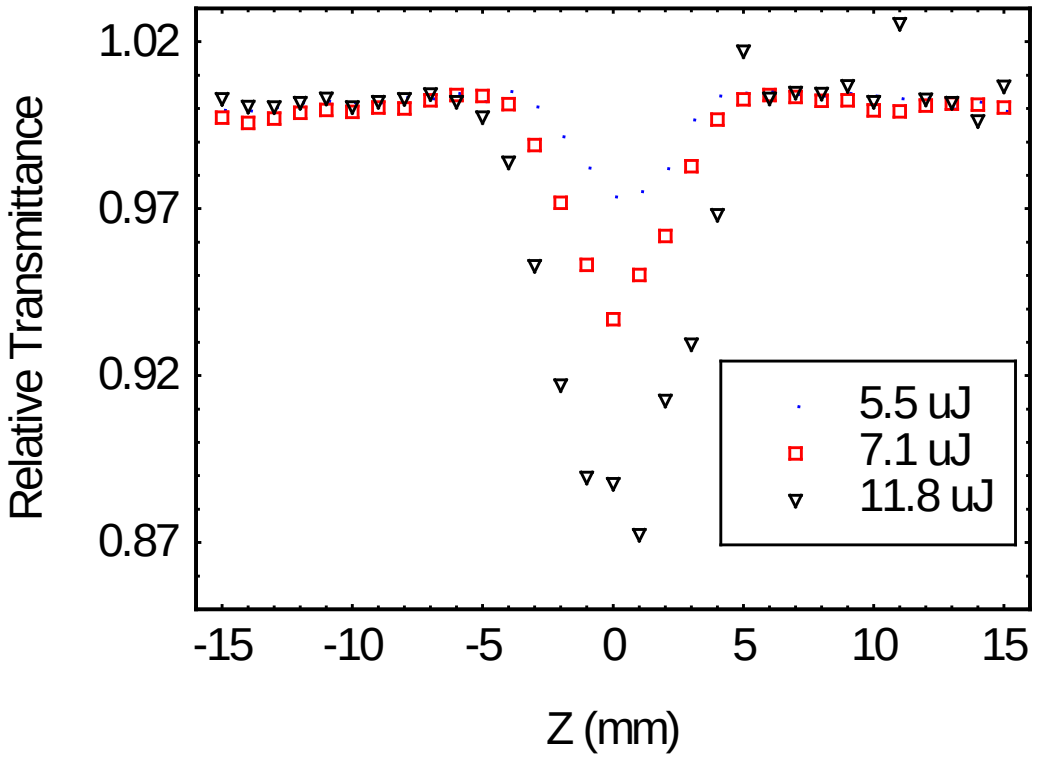

Figure 5-3. Z-Scan Data for CBS-1.

The internal transmission of the CBS-1 sample was 9% at 532 nm through a 1 mm path length cell. The input energy was varied between 5.5 and 11.8 μJ. Due to the fact that bleaching of the sample began after each shot, no averaging was performed and a delay of 200-500 seconds was introduced between each z-position. The results of the z-

scans on CBS-1 are shown in Figure 5-3. The dip of the open aperture z-scan of CBS-1 is much narrower than that of the reverse saturable absorption exhibited by the C_{60} sample, did not fit 3-level analysis models of RSA behavior, and is consistent with the nonlinear scattering mechanism of CBS.

Z-scans of the C_{60}-1 colloidal suspension were performed. The internal transmittance in a 1 mm quartz cuvette was 24.5% at 532 nm. As with CBS-1, bleaching was clearly evident after each pulse and recovery time was greater than 15 minutes. In these z-scans, the energy was varied between 7.3 and 18.6 μJ. Each point in Figure 5-4 represents one shot. The cell was translated at least 500 μm vertically or horizontally between each shot so as to provide an unbleached volume to each laser pulse. As can be seen from the data, the narrow dip of the z-scan for all energy levels tested indicates that nonlinear scattering is the dominant mechanism for this C_{60} colloid sample. The z-scan data did not fit 3-level RSA analysis but was consistent with z-scans of CBS. The weak triplet-triplet absorption observed for this sample in the nanosecond flash photolysis experiment was below the noise floor of the z-scan experiment.

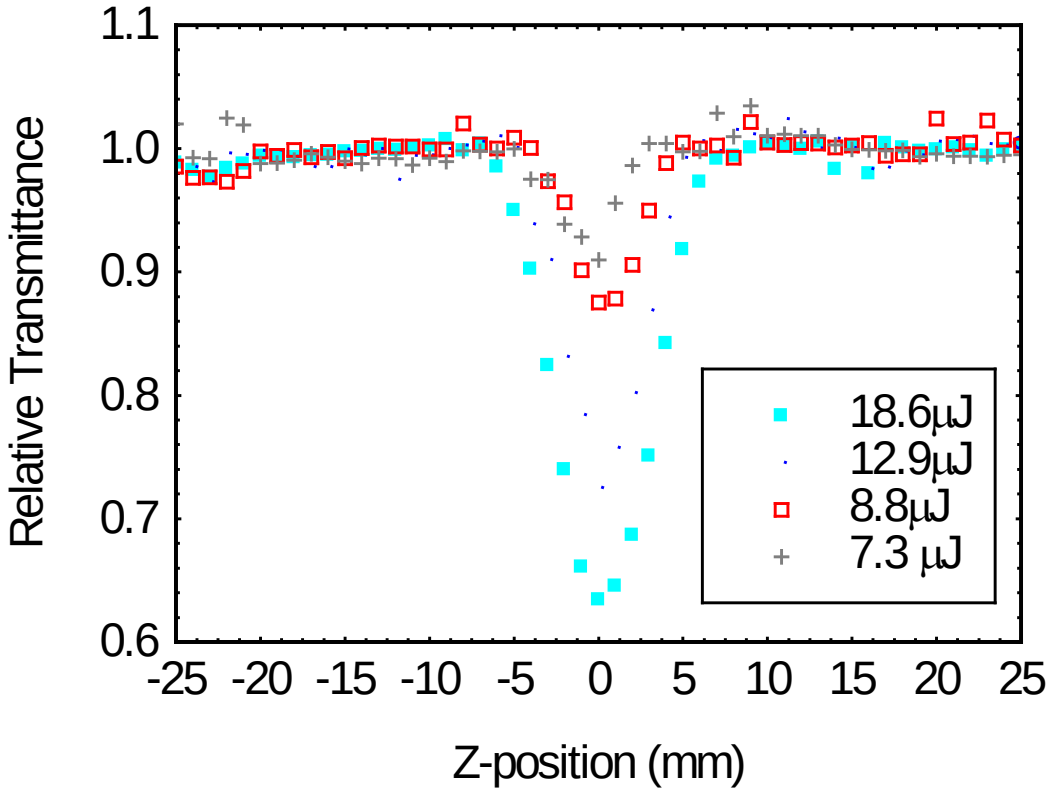

Figure 5-4. Z-Scan Data for C_{60}-1.

Z-scans of the C_{60}-2 colloidal suspension were also performed, with the same precautions to avoid shot to shot bleaching as in the C_{60}-1 sample. These z-scans, while qualitatively similar to those of the C_{60}-1 sample, did in fact fit the simplified 3-level RSA analysis, yielding triplet excited state absorption cross-sections of 2.71×10^{-19} cm^2 and 3.15×10^{-19} cm^2 at input energies of 12.8 μJ and 18.7 μJ, respectively. (See Figure 5-5.)

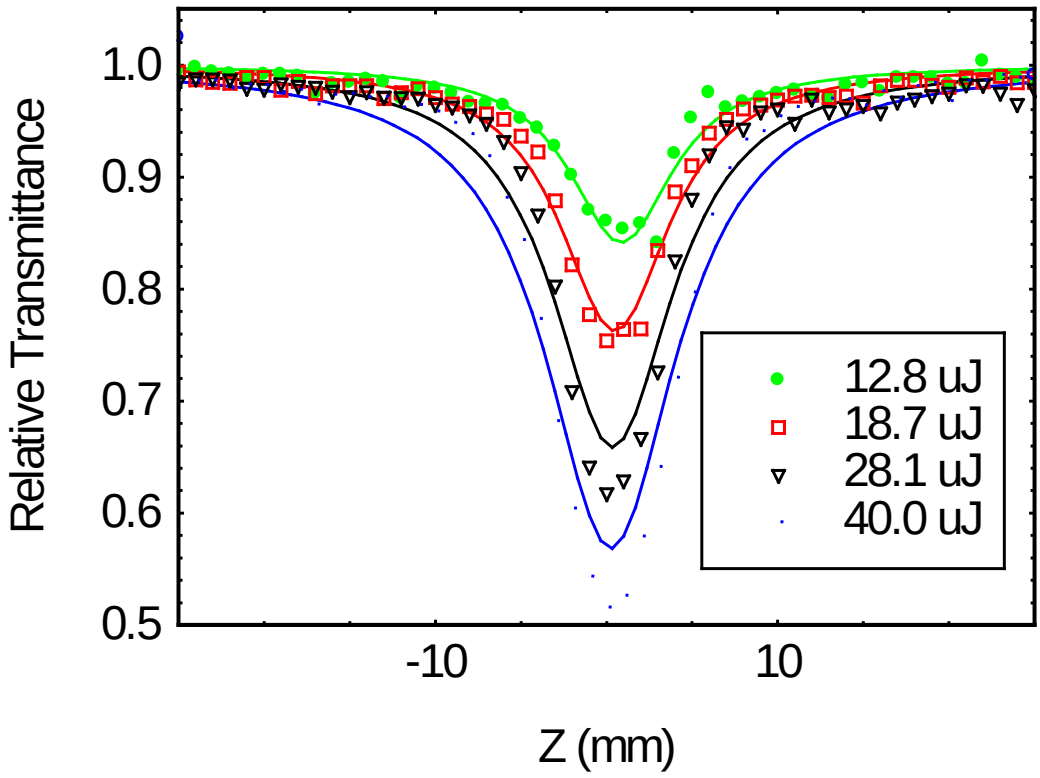

Figure 5-5. Z-Scan Data for C_{60}-2.

5.4. Conclusions

Although the nanosecond laser flash photolysis experiment showed that there was indeed weak triplet-triplet excited state absorption with a differential absorption spectrum similar to molecular C_{60} occurring in the C_{60}-1 colloidal suspension, the z-scan experiment was not sensitive enough to resolve this behavior.

The z-scan experiment was, however, able to resolve some RSA behavior in the C_{60}-2 sample. This seems to indicate that C_{60}-2 has a higher triplet quantum yield than C_{60}-1. Since there is no appreciable difference between the particle size distributions of

these two samples, the difference in RSA behavior may be related to the difference in synthesis methods and the resulting morphologies.

CHAPTER 6: TOTAL SCATTERING VERSUS NONLINEAR ABSORPTION STUDY

6.1. Introduction

The intent of this experiment is to provide a total accounting for all of the energy that is incident upon a nonlinear optical material sample, determining how much is transmitted, how much is scattered, and how much is absorbed. The experiment also determines how much light is absorbed and then remitted, using this as an indicator for the presence of certain processes such as fluorescence, phosphorescence, incandescence, or plasma generation.

6.2. Experimental Technique

6.2.1. Apparatus

In this experiment, the sample material is placed at the center of an integrating sphere. The experimental apparatus measures the input energy, transmitted energy, scattered energy, and emitted energy. Energy that is not accounted for by the transmitted or scattered energy measurements is considered to be absorbed energy.

The laser used for this study was a dye laser pumped by a frequency-doubled, injection-seeded, nanosecond pulsed neodymium yttrium aluminum garnet (Nd:YAG) laser. Rhodamine 590 in ethanol was used in the dye laser, which was tuned to 560 nm for these experiments. The full width at half maximum (FWHM) of the seeded 532 nm pump pulse was 6.9 ns with a standard deviation of 1 ns. The width the dye pulse was 9.7 ns FWHM with a standard deviation of 3.3 ns. As shown in Figure 6-1, the Nd:YAG

pulse was very smooth, but the dye pulse had a somewhat spiky temporal structure (though it was notably smoother when pumped with a seeded pulse rather than with an unseeded pulse). The dye beam was 6.5 mm in diameter and vertically polarized exiting the laser. The beam was expanded to twice its diameter and passed through a vacuum spatial filter, although no pinhole was used because, with the pinhole, insufficient energy was delivered to the experiment. The beam was attenuated by a series of two pairs of achromatic half-wave plates and polarizers, in order to achieve approximately 6 orders of magnitude of attenuation. The attenuated beam was vertically polarized proceeding to the experiment. A pulse picking shutter was used to allow single pulses through to the experiment. Running the laser at 20 Hz and using the shutter to select single pulses provided much better shot to shot energy stability than firing single pulses from the laser. The beam then passed through a variable zoom beam expander and was expanded by a factor of 1.5. The beam was verified using a shear plate collimation tester to be approximately collimated entering the total scattering apparatus.

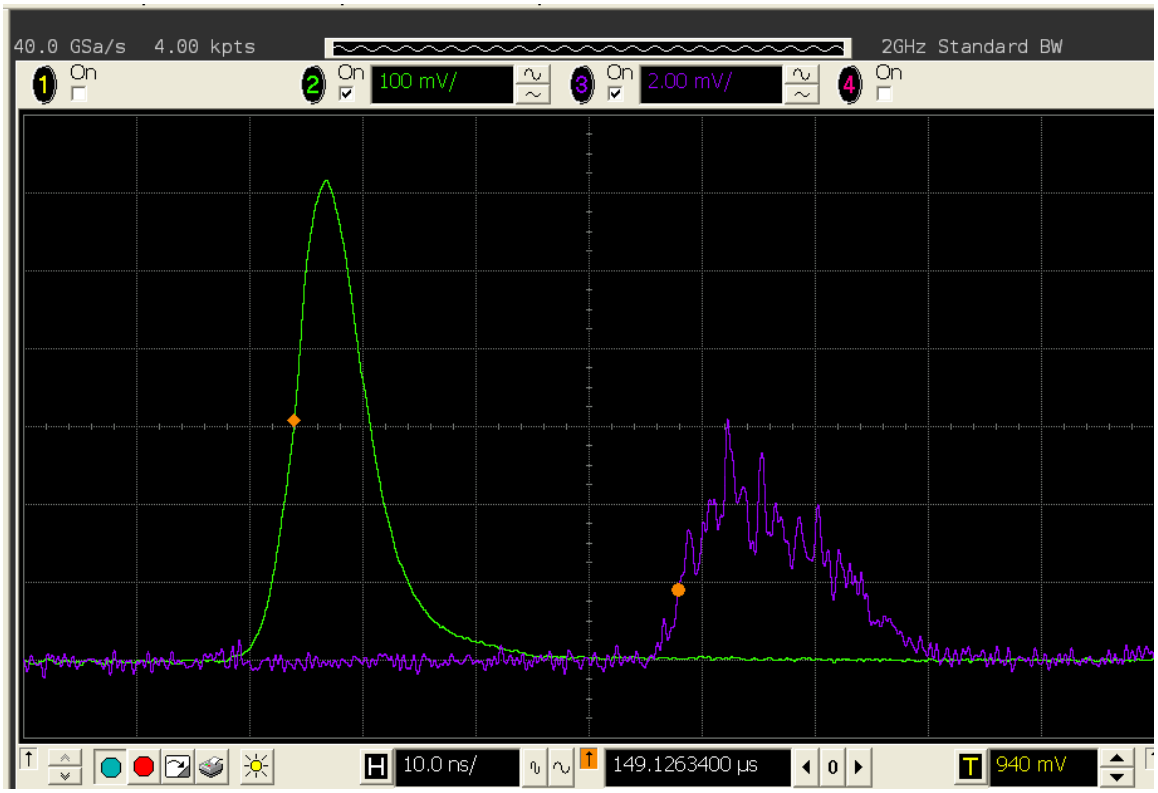

Figure 6-1. Laser Pulse Temporal Measurement. Pump laser (532 nm) in green; dye laser (560 nm) in purple.

The total scattering apparatus is shown in Figure 6-2. Part of the beam was reflected from a beam splitter, BS1, to provide a reference signal for the input energy. This reflected beam was attenuated by a neutral density filter, F1, and focused by a plano-convex lens, L3, to a silicon photodiode energy detector, D1. A lens tube, T1, was placed directly in front of the detector and a black fabric shroud was draped over the detector assembly to reduce noise from stray light. The beam transmitted through BS1 was passed through a variable aperture, A1, (which was used only during alignment and left open during data collection) and focused by a high-quality achromat, L1, to the sample, S, located at the center of the integrating sphere. The focal length of L1 was 160

mm and its diameter was 80 mm. Since the input beam diameter was 20 mm at L1, the focal geometry was f/8 in air. The liquid sample was contained in a spectroscopic cell made of quartz with an internal path length of nominally 2 mm. This cell was mounted in a cell holder suspended from the top cap of the integrating sphere. This cell holder could be translated vertically by rotating a knob on the top of the integrating sphere, in order to expose the sample to a fresh location on each shot. The beam transmitted through the sample was re-collimated by another high-quality achromatic, L2, which was identical to L1. The re-collimated beam passed through another variable aperture, A2, (again, only used for alignment) and was reflected from another beam splitter, BS2, to provide a reference signal for the output energy. Note that this signal contains some energy due to forward scattering. The reflected beam was attenuated by a neutral density filter, F2, and focused by a plano-convex lens, L4, to a silicon photodiode energy detector, D2. A lens tube, T2, was placed directly in front of the detector and a black fabric shroud was draped over the detector assembly to reduce noise from stray light. The light transmitted through the beam splitter was terminated in a beam dump. Also, the light reflected from the surfaces of detectors D1 and D2 were terminated into beam dumps. The signals from detectors D1 and D2 were read by an energy ratiometer, M1.

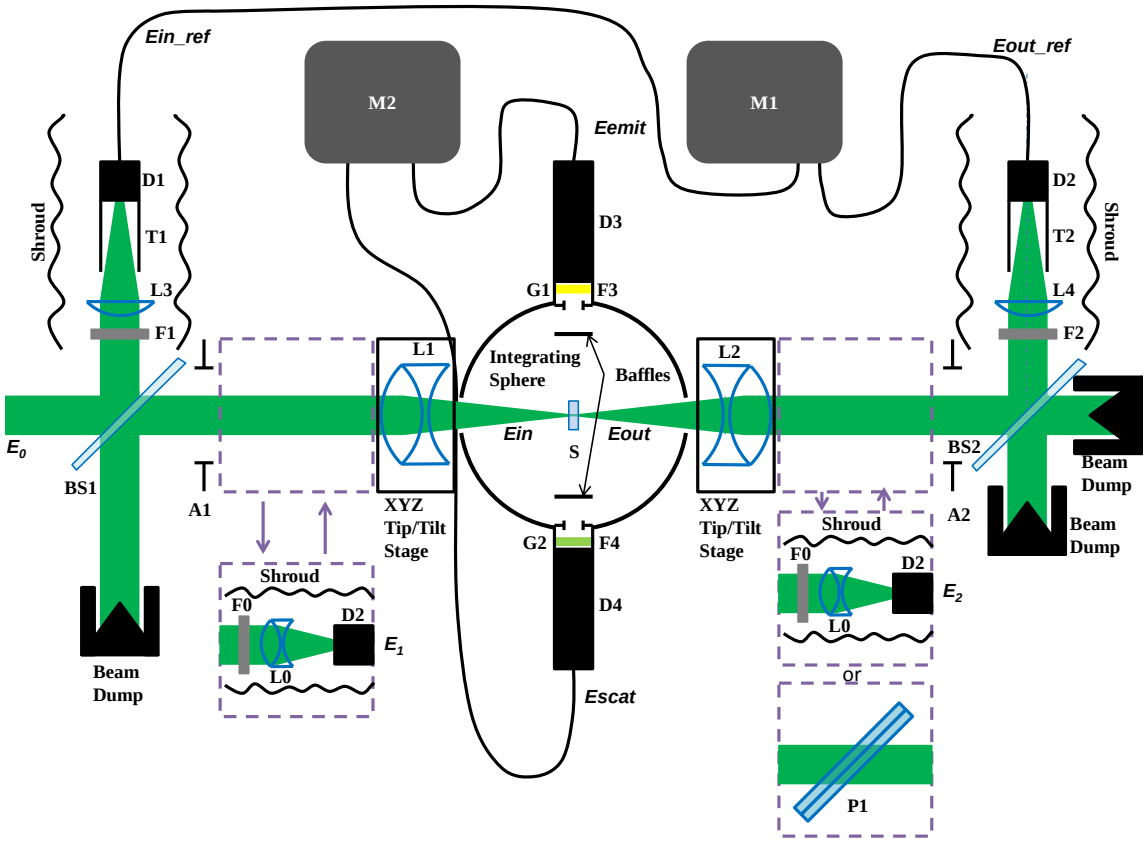

Figure 6-2. Total Scattering Apparatus.

The integrating sphere itself was 8 inches in diameter and contained six ports. The inside surface was coated with Spectraflect®. The input and output ports were 1 inch in diameter, in a line along the optical axis, and unobstructed. The two side ports were situated transverse to the optical axis and were baffled so that light from the sample could not reach these ports by a direct path. These ports were used to measure the amount of energy emitted from the sample and scattered from the sample. A Gershun tube, G1, with a 1.7 degree full angle field of view was attached to the emitted energy port.[130] A notch filter, F3, was used to block the wavelength of the input beam allow all other visible wavelengths to pass through to a silicon photodiode energy detector, D3.

Likewise, a Gershun tube, G2, with a 75 degree full angle field of view was attached to the scattered energy port. A narrow band pass filter, F4, was used to pass only the wavelength of the input beam to a silicon photodiode energy detector, D4. The Gershun tubes were necessary because filters F3 and F4 were interference filters and therefore their transmittances as a function of wavelength were sensitive to the angle of the incident light. Note that the field of view for the scattered light detector did allow out of band wavelengths through at high incident angles, but the irradiance of the emitted light was orders of magnitude below the scattered light, so a larger field of view was allowed so that the scattering signal could be sensitive enough to detect the onset of nonlinear scattering. The signals from detectors D3 and D4 were read by an energy ratiometer, M2.

To calibrate the input energy reference detector to the actual input energy, a calibration apparatus was inserted between A1 and L1. This consisted of a neutral density filter, F0, a high-quality achromat, L0, and detector D2, positioned as shown. The focal length of L0 was 80 mm and its diameter was 50 mm. A black, non-shedding fabric shroud was placed over this apparatus to reduce noise from stray light.

To calibrate the output energy reference detector to the actual output energy, a calibration apparatus was inserted between L2 and A2. This consisted of a neutral density filter, F0, a high-quality achromat, L0, and detector D2, positioned as shown. Likewise, a shroud was used to reduce background light.

A shear plate collimation tester was inserted between L2 and A2 to ensure that the light exiting the sphere was re-collimated correctly for each sample and for cases in which the sphere was empty.

To characterize the beam diameter as a function of distance along the propagation axis within the sample, the focal spot was measured in air at several z-positions using a beam profiling CCD camera. A large aperture, high quality microscope objective was used to magnify the image of the focal spot onto the camera and neutral density filters were used to adjust the exposure on the sensor so as to maximize the dynamic range of the image without saturating the camera. Several images were taken throughout the focal region along the z-axis in air. A curve fitting program was used to find a function which closely matched the through-focus behavior of the effective $1/e^2$ beam radius. The data and fitted curve are plotted in Figure 6-3.

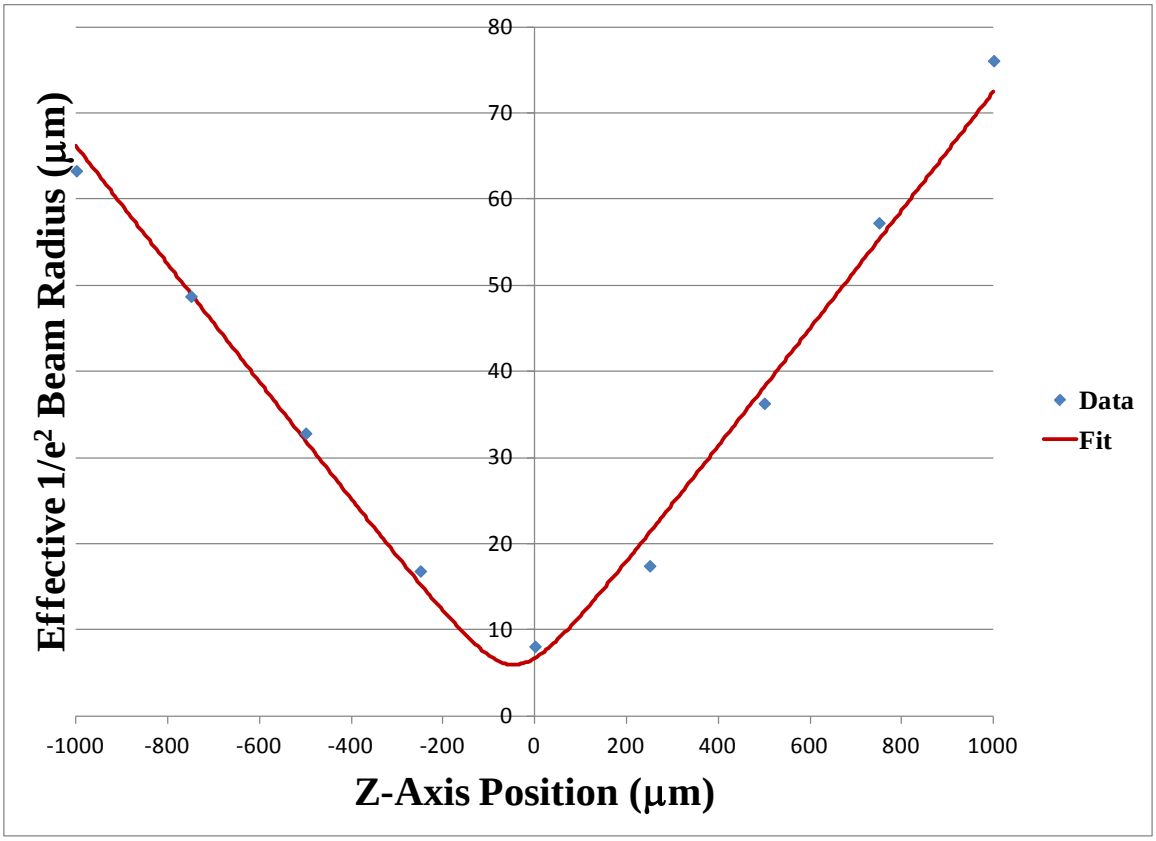

Figure 6-3. Through-focus Effective $1/e^2$ Beam Radius (measured in air).

The camera images that correspond to these data points are shown in Figure 6-4. As is evident from these images, the beam quality was far from ideal. It would have been preferable to spatially filter the beam for the experiment, but doing so reduced the energy too much. In order for all of the samples to reach strong nonlinear behavior, more energy was required and spatial beam quality had to be sacrificed.

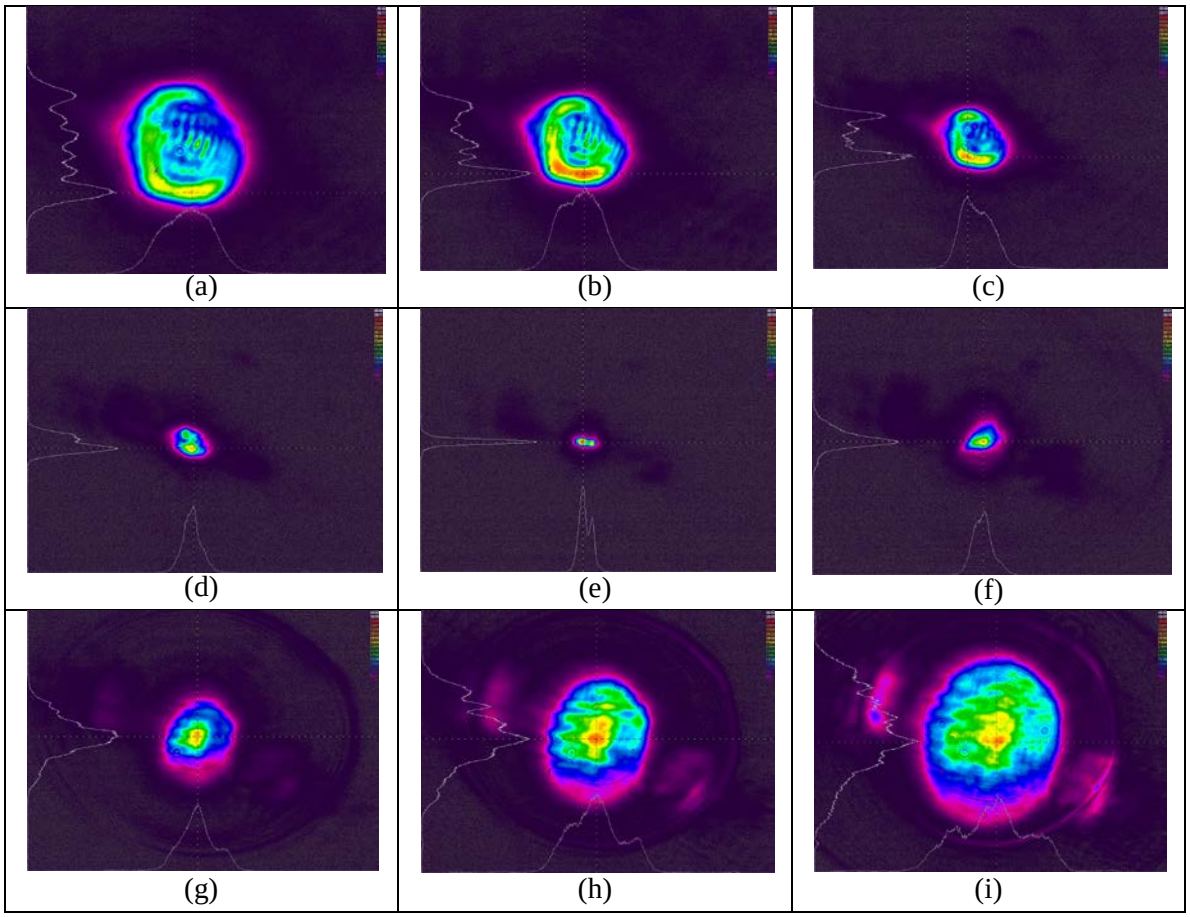

Figure 6-4. Cross-Sections of the Dye Laser Beam Through Focus (measured in air). Z-axis positions relative to focus are: (a) -1 mm, (b) -0.75 mm, (c) -0.5 mm, (d) -0.25 mm, (e) 0 mm, (f) 0.25 mm, (g) 0.5 mm, (h) 0.75 mm, (i) 1 mm.

6.2.2. Calibration Procedure

The first step in calibrating the total scattering apparatus was to align the laser beam through the integrating sphere with no sample present, with the aid of apertures A1 and A2. A shear plate was used to check collimation before the sphere. The shear plate was then placed after the sphere and the positions of lenses L1 and L2 were adjusted along the z-axis (i.e., the propagation direction) so that the focal point was approximately centered in the sphere and the output beam was re-collimated by lens L2. Detectors D1 and D2 were checked to ensure that the beams reflected to them were centered on the detector surface. (The detectors were positioned partway to focus such that the diameter of the beam was about one third of the detector surface diameter.)

6.2.2.1. Input Energy Reference vs. Input Energy

Detector D2 was then positioned for the input energy calibration as shown in Figure 6-2, along with filter F0 and lens L0. The input energy was varied over approximately 6 orders of magnitude using the polarizer and half wave plate assembly. A linear regression of $E1/Ein_{ref}$ was computed, resulting in a ratio, R1.

6.2.2.2. Input Energy Reference Versus Output Energy

Detector D2 was moved to its output energy position between lens L2 and aperture A2, along with filter F0 and lens L0. The input energy was again varied over approximately 6 orders of magnitude and a linear regression of $E2/Ein_{ref}$ was computed, resulting in a ratio, R2.

6.2.2.3. Input Energy Reference Versus Output Energy Reference

Detector D2 was moved to the output energy reference position. The input energy was again varied over approximately 6 orders of magnitude and a linear regression of $Eout_{ref}/Ein_{ref}$ was computed, resulting in a ratio, R3.

6.2.2.4. Adjustment for Lenses and Sphere Ports

Another ratio, R4, was defined to account for the losses resulting from L1 and L2 and the input and output sphere ports. It is defined as:

$$R4 = \frac{E_2}{E_1} = T_{L1}T_{PORT1}T_{PORT2}T_{L2},$$

where T indicates the transmittance of the element. R4 is simply a combination of the other three ratios, but is referred to separately for convenience.

The input and output energies are then calculated as follows:

$$Ein = \frac{\sqrt{R4}}{T_{F0}T_{L0}} R1\ Ein_{ref}$$

and

$$Eout = \frac{R2}{\sqrt{R4}T_{F0}T_{L0}R3} Eout_{ref}.$$

L0 was a high-quality, anti-reflection coated achromat and its transmittance was estimated as 98%. Lenses L1 and L2 were identical, so their transmittances are the same. Although the transmittance loss at the input port is likely higher than that of the output port, they were attributed the same amount of transmission loss for expediency of calculation. Note that Ein and Eout are defined here as external to the cell.

6.2.2.5. Scattered Energy Calibration

A port plug with a calibrated reflectance was used to close the output port on the integrating sphere. The scattered energy detector was filtered so that it only allowed through the incident wavelength. (In the case of this work, this was 560 nm.) The input energy was again varied over approximately 6 orders of magnitude and data collected on the input energy reference detector and the scattered energy detector. The amount of energy reflected into the sphere was calculated by multiplying the input energy (determined from the input energy reference reading) by the reflectance of the port plug at the wavelength of the input beam. A linear regression of $E_{reflected}/E_{scat}$ was computed, establishing the relationship between the raw scattered energy detector signal and the actual energy scattered from a sample. There was some leakage of scattered light through the notch filter onto the emitted energy detector. Therefore, the raw signal from the scattered energy detector was then plotted versus the raw signal from the emitted energy detector and an equation was derived from a curve fitting program, since the data was not linear for low input energies. This function was subtracted from the emitted energy data to compensate for the scattered energy leakage.

Note that there are three ports open (or filled with detectors rather than a high reflectance coating) during calibration, but four ports open when measurements are being taken, because the output port plug is removed to measure transmittance. Therefore, a correction factor must be applied.

The flux incident on the scattered light detector is given by:

$$\Phi_d = L_s A_d \Omega,$$

where L_s is the radiance on the surface of the sphere, A_d is the area of the detector, and Ω is the solid angle that the detector views. The radiance on the surface of the sphere is given by:

$$L_s = \frac{\Phi_i}{\pi A_s} M,$$

where Ω_i is the incident optical flux, A_s is the surface area of the sphere, and M is the sphere multiplier. The sphere multiplier is given by:

$$M = \frac{\rho}{1-\rho(1-f)},$$

where ρ is the reflectance of the coating on the inside surface of the sphere and f is the port fraction. The port fraction is calculated by adding the areas of all of the ports and dividing this sum by the total surface area of the sphere.[131]

The sphere diameter was 8 inches, so its area was 1297 cm^2. The diameter of each port was 1 inch, so the area of each port was 5 cm^2. There were three ports open during calibration and four ports open during measurements, which correspond to port fractions of 0.0117 and 0.0156, respectively. The reflectance of the sphere coating at 560 nm was 0.976. Therefore, the sphere multipliers corresponding to the 3-port and 4-port cases were 27.556 and 24.882, respectively. To adjust for the correct number of open ports, the detector reading was multiplied by its calibration factor and then a port adjustment factor of 27.556/24.882.

6.2.2.6. Emitted Energy Calibration

With the calibrated reflectance port plug still in place on the output port, the laser wavelength was changed as far as possible from the normal input wavelength within the

response curve of the current laser dye. (In the case of this work, this was 580 nm.) The emitted energy detector was filtered such that it blocked the normal input laser wavelength, but passed the detuned wavelength. The input energy was again varied over approximately 6 orders of magnitude and data collected on the input energy reference detector in the emitted energy detector. As above, the amount of energy reflected into the sphere was calculated by multiplying the input energy (determined from the input energy reference reading) by the reflectance of the port plug at the detuned wavelength. A linear regression of $E_{reflected}/E_{emit}$ was computed, establishing the relationship between the raw emitted energy detector signal and the actual energy emitted from a sample. There was some leakage of emitted light through the bandpass filter onto the scattered energy detector. Therefore, the raw signal from the scattered energy detector was then plotted versus the raw signal from the emitted energy detector and an equation was derived from a curve fitting program, since the data was not linear for low input energies. This function was subtracted from the scattered energy data to compensate for the emitted energy leakage.

As with the scattered energy calibration, a correction factor must be applied to account for the loss of energy through the output port, since this is open during the experiment but not during calibration.

6.2.2.7. Neutral Density Filter Check

To check the system calibration, a neutral density filter was inserted between aperture A1 and lens L1 and the input energy was varied over approximately 6 orders of magnitude. The transmittance of this filter, as measured in the total scattering apparatus,

was compared to a measurement of the same filter in a UV-Vis spectrophotometer. (This filter was chosen to have a transmittance of 62.02% at 560 nm, which was close to the linear transmittance of the samples.)

6.2.3. Data Collection

Once the experiment was calibrated, a sample was inserted into the integrating sphere. Lenses L1 and L2 were adjusted so that the transmitted laser beam was re-collimated. Starting at a low input energy, a z-scan was performed by translating lenses L1 and L2 by the same amount, gradually stepping the focal point through the sample along the optical axis. (Normally, z-scan is performed by translating the sample. However, since the sample had to remain at the center of the integrating sphere, the lenses were translated instead.) The input energy was then increased by approximately an order of magnitude and the z-scan repeated. This was done over about three or four orders of magnitude. The position in which the sample showed the strongest nonlinear response was chosen as the z-position of the sample during data collection. In cases where the shape of the z-scan curve changed with increasing input energy, more weight was given to the higher input energy curves when selecting the optimal sample position.

Once the best sample position was determined, the sample cell was translated vertically to a fresh location (maintaining the same z-position) and the wave plates were adjusted for maximum attenuation. Single shot data were taken from the input energy reference detector, the output energy reference detector, the scattered energy detector, and the emitted energy detector over approximately 6 orders of magnitude of input energies. The samples were kept in the same vertical location so long as the response

was linear, but translated vertically so that each shot exposed a fresh portion of sample for each data point once the behavior began to be nonlinear.

6.3. Results and Discussion

The experimental results of the total scattering experiment are plotted below for the six samples examined in this study. The data are plotted in terms of input energy vs. the percent of this energy that was either transmitted (including a small amount of forward scattered light), scattered into the integrating sphere, or absorbed. Since the input energy plotted on the x-axis is defined as the energy just before the sample cell, the Fresnel reflection loss is also plotted. This was assumed to be constant. While this is not strictly true (as in the case of a strongly absorbed beam, which would not reflect as much upon exiting the cell as upon entering), this simplifying assumption is not expected to introduce significant errors into the data. Although measured, the percent of the energy accounted for by emitted light is not plotted in these results, since it was orders of magnitude below all of the other energy values and is a subset of the absorbed energy.

Figure 6-5 shows the experimental results for CBS-1. The sample remains linear until an input energy of about 2 μJ. At this point, both scattering and absorption increase nonlinearly. However, the nonlinear response is clearly dominated by a scattering mechanism. There has long been a debate in the literature about the precise mechanisms of attenuation by carbon black suspensions. The nonlinear absorption seen here could be taken as evidence for nano-plasmas playing a role in the response. Also note the sharp onset of nonlinear behavior once the activation threshold is reached. This is consistent

with a phase change mechanism resulting in explosive formation of scattering centers upon sublimation of the particle.

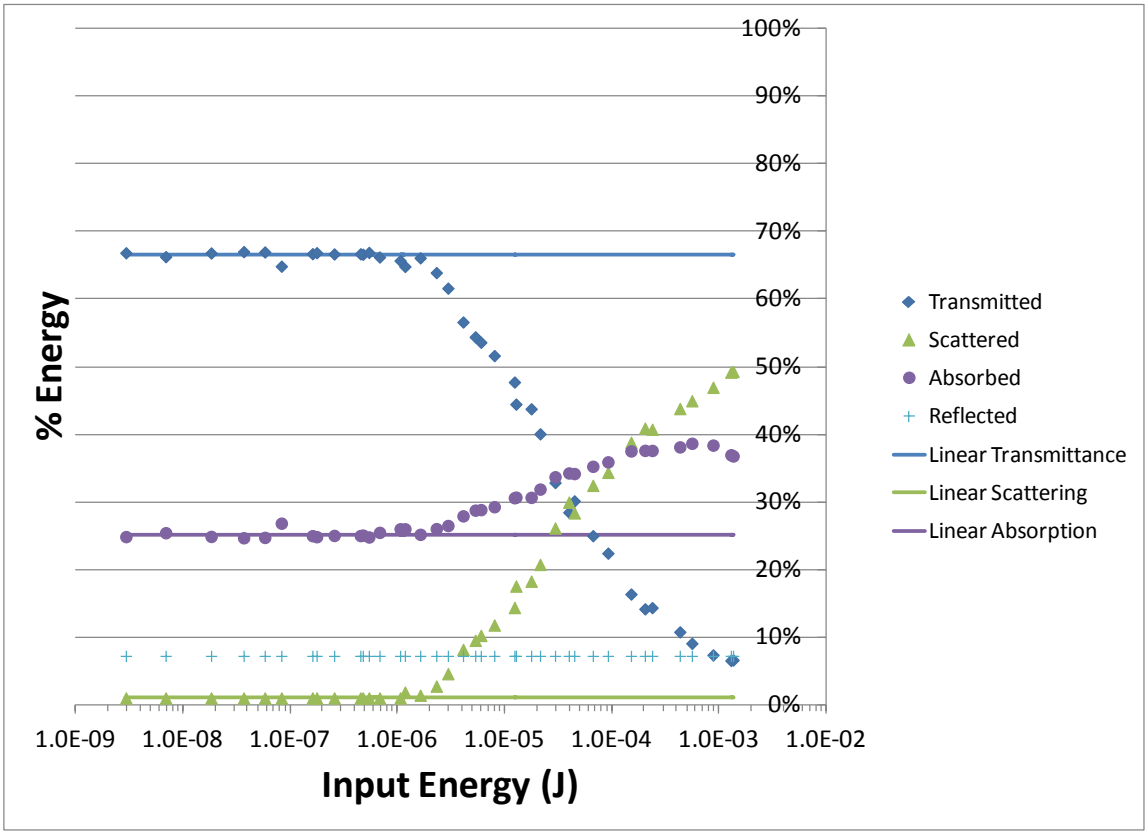

Figure 6-5. Percent of Input Energy Transmitted, Scattered, and Absorbed by CBS-1.

Figure 6-6 shows the experimental results for CBS-2. The sample remains linear until an input energy of about 10 μJ. Here, it begins to roll over much more gradually than CBS-1. CBS-2 is a less than ideal sample. The intent of this sample was to provide a carbon black suspension of a different size with which to compare CBS-1. The CBS-2 sample agglomerated into a bimodal distribution of particles with about 98% of the population near 100 nm in diameter and about 2% of the population close to 1.6 μm in diameter. The light interacts much more strongly with the micron-sized agglomerates

than the nanometer-sized particles since the absorption cross-sections of the micron-sized agglomerates are much larger. The higher threshold is indicative of the micron-sized particles and the very gradual attenuation is likely due to the sparsity of these particles. Note that in this case, the absorption remains linear even in the NLO response regime.

The marked differences in the behaviors of CBS-1 and CBS-2 may be at least partially due to the differences in the carbon black materials from which they were made. CBS-1 was made from Monarch-1000®, which is a very high surface area carbon black with a small primary particle diameter of 16 nm and very high conductivity. CBS-2 was made from Sterling-1120®, which has a primary particle diameter of 90 nm and is the lowest surface area carbon black produced by Cabot Corporation. Sterling-1120® also has the lowest conductivity of any carbon black produced by Cabot Corporation. The higher density of the Sterling-1120® aggregates would result in a slower temperature rise for the same amount of input energy. Also, since its conductivity is lower, Sterling-1120® would not liberate electrons as easily as Monarch-1000®. One would presume that there would be a soup of free electrons upon particle sublimation, but perhaps in CBS-2, the boiling point of water is reached before the sublimation point of carbon black. If nanoplasmas are the source of the nonlinear absorption seen in CBS-1, then the absence of such plasmas could explain the flat absorptance in CBS-2. An alternate explanation is that according to Mie theory, scattering is dominant for micron-sized scattering centers. It may simply be that any absorption is dwarfed by the scattering contribution from the larger scattering centers, which will necessarily be at least as large as the micron-sized particles from which they form.

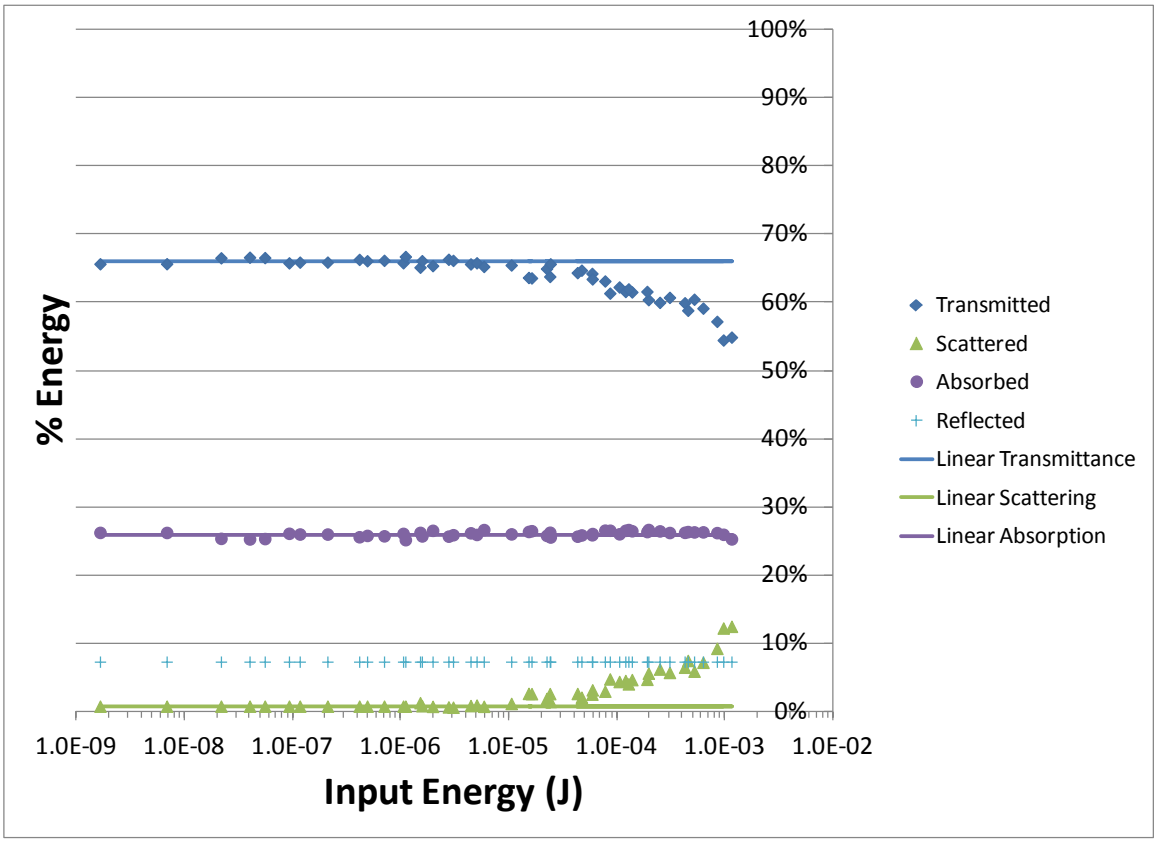

Figure 6-6. Percent of Input Energy Transmitted, Scattered, and Absorbed by CBS-2.

Figure 6-7 shows the experimental results for a solution of C_{60} in toluene. Nonlinear behavior begins in the sample at around 100 nJ and is entirely dominated by nonlinear absorption. The gradual roll in the percent transmittance data is typical of RSA materials. A region of minimal nonlinear scattering is exhibited between about 20 and 250 μJ. This is followed by a region between about 350 μJ and 2 mJ in which nonlinear scattering increases significantly, corresponding to a slight decrease in nonlinear absorption. Finally, at the highest input energies, there is a plasma created at the front window of the cell, resulting in window damage. In this region, nonlinear scattering decreases and nonlinear absorption increases. One possible explanation for this behavior

is that the region of small-scale scattering corresponds to vaporization of the toluene as it is heated by the C_{60} molecules and that the region of more intense scattering corresponds to sublimation of the C_{60} molecules themselves. This would parallel behavior reported by Reihl and Fougeneat,[4, 5] in which carbon suspensions in organic solvents with favorable thermodynamic properties exhibited a two-threshold behavior: the first corresponding to boiling of the solvent around the particle and the second corresponding to sublimation of the particle itself. Alternately, the low scattering region might correspond to scattering from nano-bubbles and the more strongly scattering region could result from dielectric breakdown of the liquid.

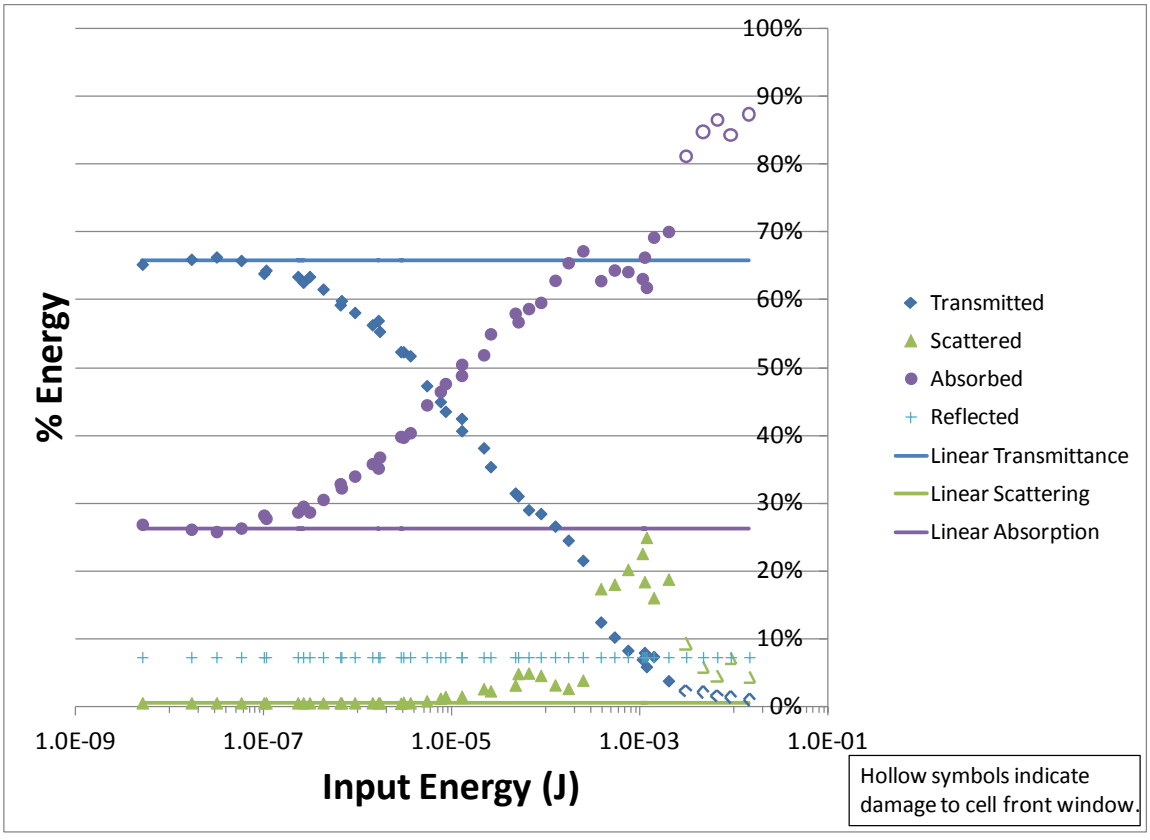

Figure 6-7. Percent of Input Energy Transmitted, Scattered, and Absorbed by C_{60} in Toluene.

Figure 6-8 shows the experimental results for the C_{60}-1 colloidal suspension. Nonlinear action begins with a sharp activation near 1 μJ. The nonlinear response is dominated by scattering, with a notable contribution from nonlinear absorption, much like CBS-1. The increase in scattering is stronger in C_{60}-1 than in CBS-1. Note that this sample has a significant amount of linear scattering, resulting in a hazy appearance. This is due to the high concentration of Triton X-100 surfactant, which was necessary to create a suspension this highly concentrated. Qualitatively, this sample seems to behave very much like a carbon black suspension. This is in keeping with the transient absorption spectroscopy results, indicating a very low triplet quantum yield for this sample.

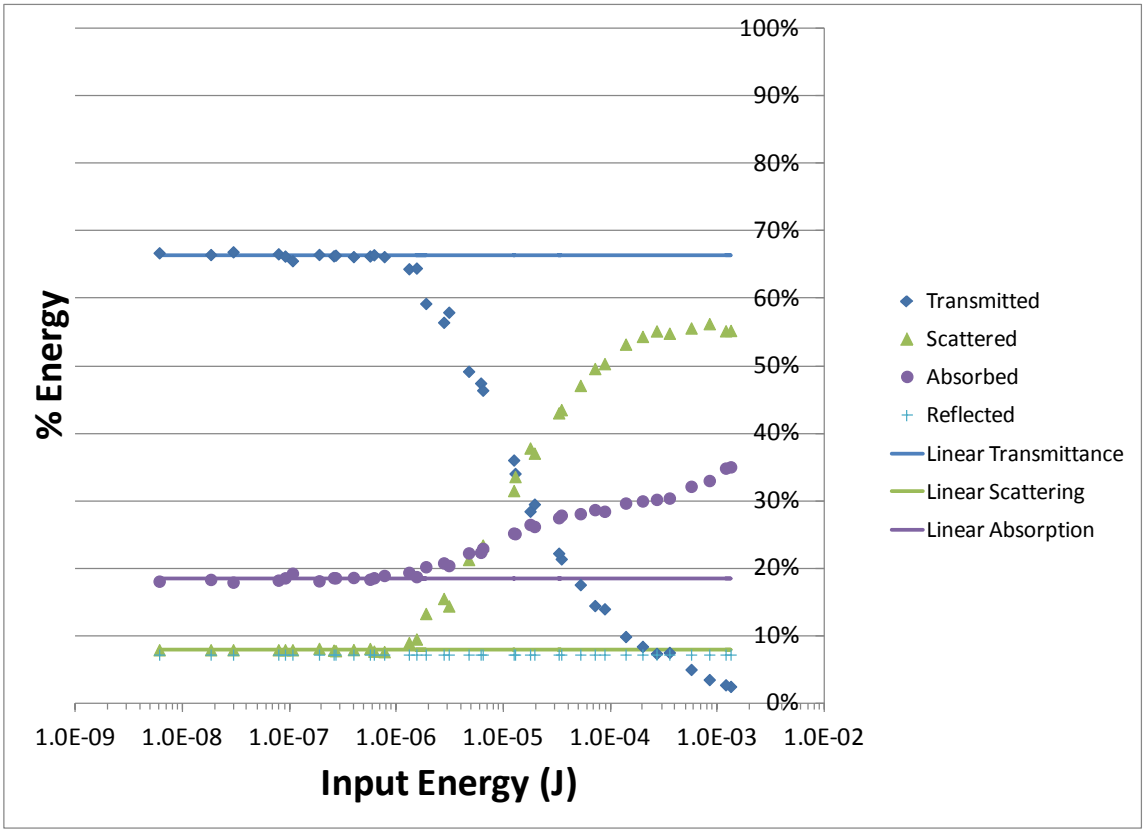

Figure 6-8. Percent of Input Energy Transmitted, Scattered, and Absorbed by C_{60}-1.

Figure 6-9 shows the experimental results for the C_{60}-2 colloidal suspension. Overall, the data look quite similar to the C_{60}-1 sample. However, instead of a sharp activation threshold, nonlinear action begins with a gradual roll near 1 μJ. This is indicative that the RSA mechanism is playing some part. Also note that, while nonlinear scattering is still the dominant mechanism in this sample, there is noticeably more nonlinear absorption and less nonlinear scattering in the C_{60}-2 sample than in C_{60}-1. This agrees with the z-scan study, which indicated that C_{60}-2 had stronger RSA behavior than C_{60}-1. Since the particle size distributions of these two samples are so similar, it is hard to argue that this difference in behavior is due to particle size. However, the syntheses of these two samples were significantly different, which apparently resulted in different particle morphologies, which could result in a difference in quenching rates. C_{60}-2 has a slightly lower concentration of Triton X-100 than C_{60}-1, but still enough to cause noticeable linear scattering.

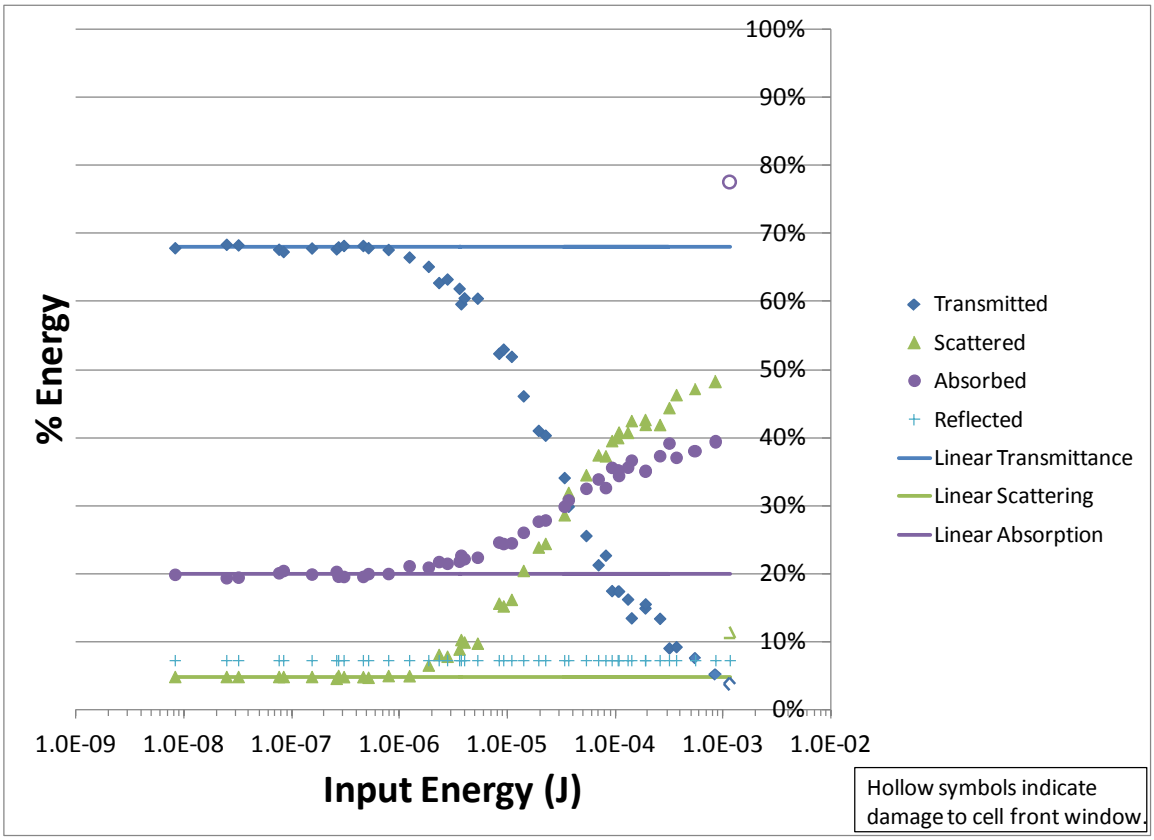

Figure 6-9. Percent of Input Energy Transmitted, Scattered, and Absorbed by C_{60}-2.

Figure 6-10 shows the experimental results for the C_{60}-3 suspension. The nonlinear behavior begins at about 200 nJ with pure nonlinear absorption. This sample clearly exhibits only RSA behavior at the beginning of its response. From about 10 to 40 μJ, a small amount of nonlinear scattering begins to contribute. Starting at about 70 μJ, nonlinear scattering increases significantly. Here, the particles have sublimed, creating strong scattering centers.

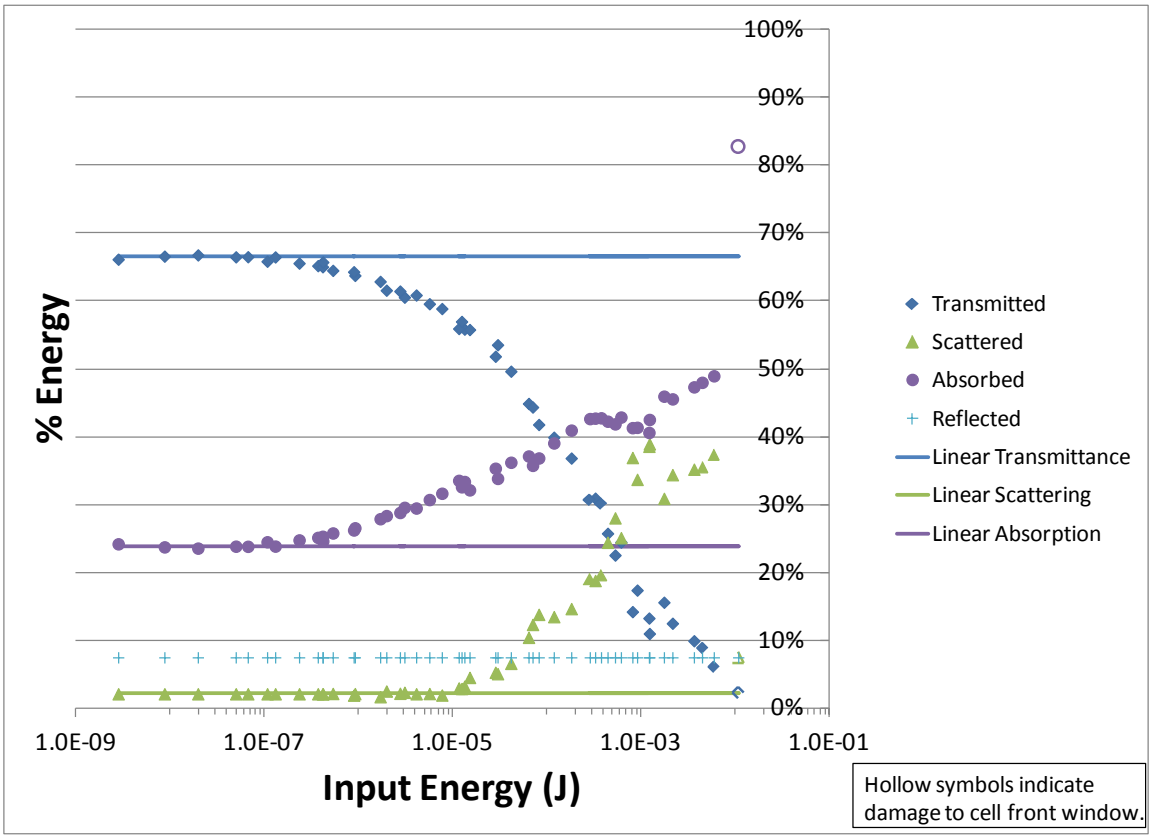

Figure 6-10. Percent of Input Energy Transmitted, Scattered, and Absorbed by C_{60}-3.

Figure 6-11 presents the percent transmittance of all the samples as a function of input energy. At the lowest input energies, C_{60} in toluene has the lowest NLO threshold and begins attenuating sooner than the other materials because it has the strongest RSA behavior. The C_{60}-2 and C_{60}-3 colloidal suspensions begin attenuating next, showing evidence of some RSA behavior at the beginning of their NLO response. In the middle range of energies, CBS-1, C_{60}-1, and C_{60}-2 reach their activation thresholds and begin increasing in attenuation more rapidly than the gradual roll of C_{60}-3 and C_{60} in toluene. For equal input energies, the C_{60} colloid materials have slightly less transmittance than CBS-1 in the nonlinear region. C_{60}-1 has the strongest attenuation in this region. One

possible explanation for this could be that since C_{60}-2 has a higher triplet quantum yield, more electrons are trapped in the long-lived triplet state and don't contribute to heating the particle as quickly as the more strongly quenched C_{60}-1 colloids. Another possibility is that the high concentration of Triton X-100 may come into play. Triton X-100 is a strong bubble promoter and its high concentration in C_{60}-1 may contribute to the stronger scattering behavior observed in this sample. Although C_{60}-3 started off attenuating well due to its RSA character, at the higher energies, it lags the other samples, likely because the scattering centers it forms are much smaller than the other samples because the size of its colloidal particles are much smaller. At the very highest input energies, the C_{60}-1 and C_{60}-2 colloids pull away from the CBS-1 curve and provide slightly more attenuation.

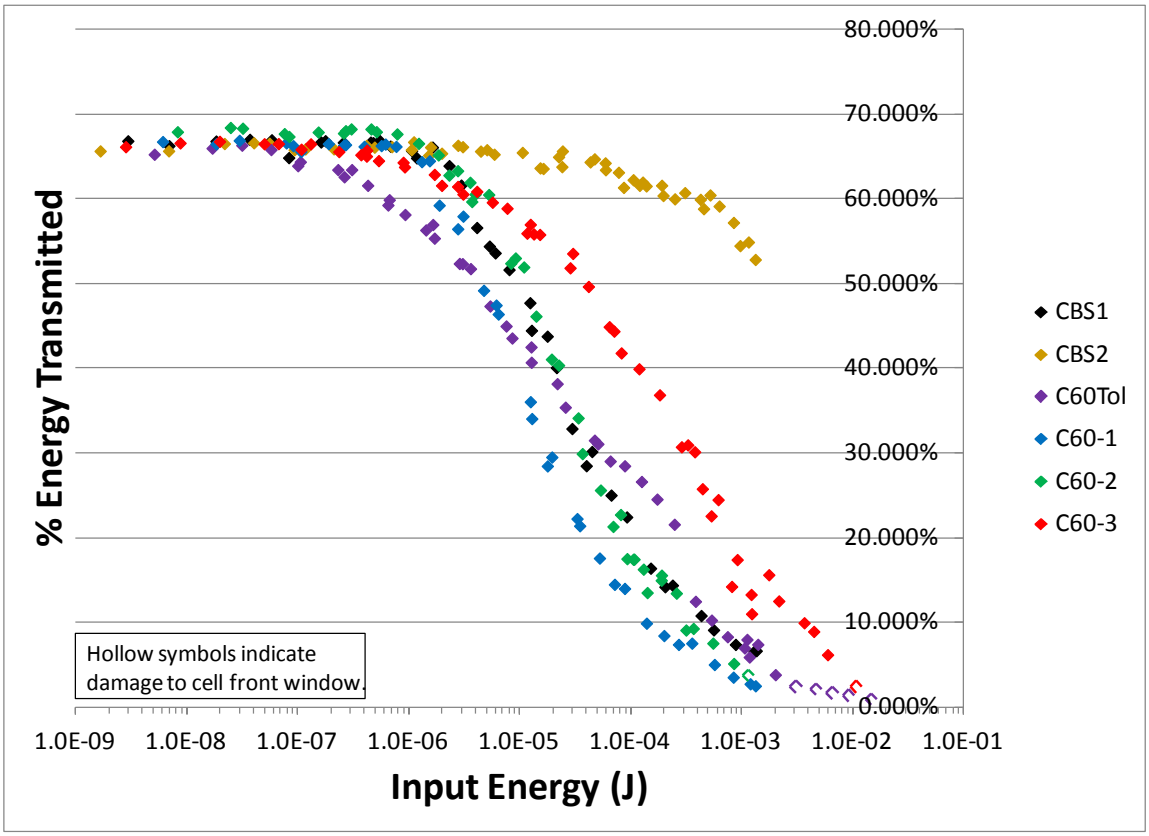

Figure 6-11. Percent of Input Energy Transmitted by All Samples.

Figure 6-12 re-plots the same data in term of optical density, which is defined as log base 10 of the inverse of the transmittance. This presentation makes it easier to see the separation in the data at the highest input energies, emphasizing the separation between the attenuations observed in C_{60}-1, C_{60}-2, and CBS-1.

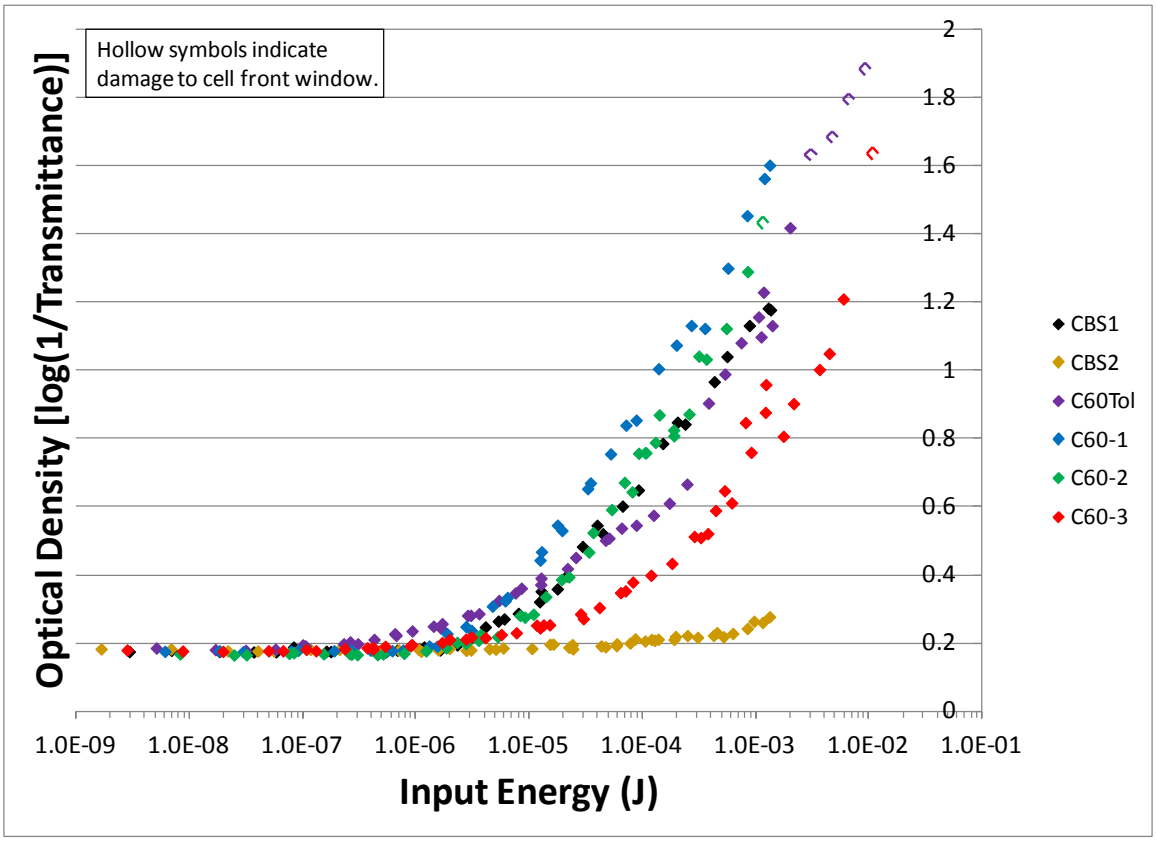

Figure 6-12. Optical Density vs. Input Energy for All Samples.

6.4. Conclusions

CBS-1 has a sharp onset of NLO behavior followed by a sharply dropping transmittance. This is consistent with the formation of scattering centers upon sublimation of the particles. The attenuation in the NLO regime is due to both nonlinear absorption (NLA) and nonlinear scattering (NLS), but dominated by scattering.

The higher NLO threshold of CBS-2 indicates that the light is interacting more strongly with the micron-sized agglomerates. The more gradual decrease in transmittance is probably due to the sparsity of these large particles in the bimodal distribution. The attenuation in CBS-2 is entirely due to NLS, with the absorption

remaining completely linear to even the highest input energies. It might be possible that the NLS observed in CBS-2 is due to water vapor bubbles and that the micron-sized particles have not sublimed at the highest input energies observed in this data. The lack of microplasmas could explain the lack of any nonlinear absorption in the response. Alternatively, assuming that the scattering centers form from micron-sized agglomerates, these centers will be at least that large, and Mie theory indicates that scattering will dwarf absorption for very large scattering centers. The physical properties of the carbon black starting materials may also play a role in the markedly different behaviors of CBS-1 and CBS-2. CBS-1 is made from a highly conductive, high surface area carbon black with very small primary particle size. CBS-2 is made from a low surface area carbon black with very large primary particle size and low conductivity.

C_{60} in toluene follows the expected RSA behavior with a very low NLO threshold and a gradual roll to the transmittance curve. The NLO response is completely due to RSA up to 20 μJ, where NLS begins to contribute in two distinct regions. The distinctiveness of the character of these two regions indicates that two different types of scattering centers form. One interpretation is that the first region corresponds to vapor bubbles while the second corresponds to sublimed molecules. An alternate interpretation is that the first region is due to bubble scattering, while the second region may be due to dielectric breakdown in the liquid.

C_{60}-1 behaves essentially like a carbon suspension, with a sharp onset and a sharp drop in transmittance. The NLO response is due to both NLA and NLS, but is dominated

by NLS. This result agrees with the low triplet quantum yield calculated from the transient absorption spectroscopy results.

C_{60}-2 has a soft roll at the beginning of its NLO response that looks like RSA behavior, but it quickly transitions to a NLS-dominated response. The indications of a stronger contribution from RSA in this sample agree with the z-scan findings.

The difference in behavior between C_{60}-1 and C_{60}-2 is more likely related to particle morphology than to particle size since TEM measurements confirmed different morphologies, but DLS and NTA measurements showed very similar particle size distributions. The tighter crystalline packing of C_{60}-1 likely leads to more efficient quenching of the first excited singlet state, which is why its RSA behavior is weaker.

C_{60}-3 clearly shows RSA-only behavior for much of its response, followed by a region where NLS contributes significantly. Since its TEM images also indicated an amorphous structure, this follows the trend of more amorphous particles having a higher triplet quantum yield and therefore stronger RSA behavior.

All three colloidal C_{60} suspensions have significant linear scattering, due to the high loading of Triton X-100 needed to achieve high colloid concentrations.

C_{60} in toluene provides the most attenuation at low input energies. C_{60}-1 provides the most attenuation at mid to high energies. Although they have similar particle sizes, C_{60}-1 attenuates more strongly than C_{60}-2, indicating that there may be an inverse correlation between triplet quantum yield and NLS performance in C_{60} colloids.

CHAPTER 7: MODELING OF NONLINEAR ABSORPTION, NONLINEAR SCATTERING, AND COMBINED EFFECTS

7.1. Introduction

This section draws from several approaches reported in the literature to develop simple numerical models for particulate suspensions and RSA materials, combining these into a hybrid approach to model suspensions of particles made up of RSA molecules. The output of these models is then compared to experimental data from the total scattering experiment to glean insight into the photophysical processes responsible for the observed behavior.

The models are limited in that they have several simplifying assumptions. However, they are useful in analyzing the experimental results. Furthermore, the basic building blocks of these models may be expanded in the future to a more complex model.

7.2. Theory: Nonlinear Scattering (Basic Model)

The dominant optical limiting mechanism in carbon black suspensions is nonlinear scattering. The black carbon particles have a strong linear absorption. Irradiation of such a suspension of particles by a strong pulse of light causes rapid heating and vaporization of the particles and surrounding solvent, resulting in explosive bubble growth, creating scattering centers which scatter (and absorb) much of the incoming light, thereby attenuating the light transmitted along the original beam path. [132-134]

Treating the particles as volumetric absorbers and assuming spherical symmetry, the volumetric density of the power absorbed by an individual particle is given by:

$$W(t) = \frac{3\sigma_{abs} I(t)}{4\pi R^3},$$

where σ_{abs} is the absorption cross section of the particle, I(t) is the irradiance incident on the particle as a function of time, and R is the particle radius. The absorption cross section, σ_{abs} is calculated by Mie theory and is dependent upon the complex refractive indices of both the particle and the surrounding fluid.[5] In the case of this work, the Mie calculations were done in code written in MATLAB®, which called a subroutine of the BHMIE program that was published in the appendix of Bohren and Huffman's treatise on absorption and scattering of light by small particles and translated to the MATLAB® language by Krzszystof Markowicz of the Atmospheric Physics Department, Institute of Geophysics, University of Warsaw. This version of BHMIE has been made publicly available on the internet.[135]

The temperature of a particle rises as a function of the power absorbed. As a simplifying assumption, the model neglects heat transfer from the particle to the liquid. As discussed in the results section, it was necessary to include a fitting parameter in the model to account for the fact that there is some heat transfer away from the particle in order to match the experimental data. The time evolution of the particle's temperature is given by:

$$\mathbb{T}(t) = \mathbb{T}_0 + \int_0^{t(W_{max})} \frac{H\, W(t)}{\rho C_p}\, dt,$$

where T_0 is the initial temperature, H is the "heating efficiency factor", ρ is the density of the carbon particle and C_p is the specific heat.[5]

The specific heat of carbon is strongly temperature dependent, so this value must be updated at each time slice in the model's code. In order to approximate a value for specific heat at any continuous value of temperature, data for the specific heat of graphite was analyzed using curve fitting software. The best fit equation is shown in Figure 7-1. Data for graphite was used, since data for amorphous carbon was not readily available at high temperatures and the values of graphite and amorphous carbon are close at lower temperatures.

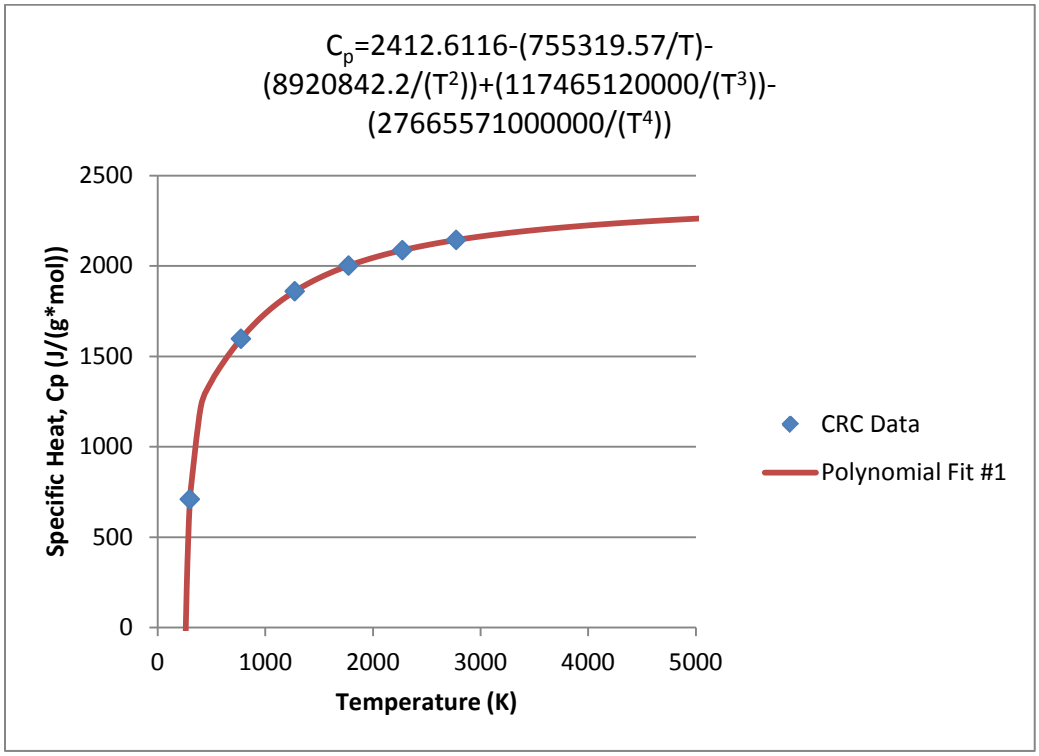

Figure 7-1. Specific Heat of Carbon as a Function of Temperature.

The model put forth here uses the basic framework of the model for nonlinear scattering in carbon black suspensions published by McEwan.[8] A particle is assumed to be in one of two possible states, each with a corresponding extinction coefficient. In the first state, the particle is considered to be in the linear region and the extinction coefficient is due to a combination of ground state absorption and linear scattering. When the particle has absorbed enough incident photons to be raised to carbon's sublimation temperature[5], a phase change is assumed and the extinction coefficient changes to account for nonlinear scattering from the bubble formed. The phase change is assumed to be instantaneous; scattering dynamics are not included. Riehl and Fougeanet reported a series of two thresholds in carbon black suspensions corresponding first to the boiling point of the host liquid and then to the sublimation temperature of the carbon black particle.[4, 5] This behavior was seen to be strongly dependent upon the thermodynamic properties of the host liquid. In the case of water, they observed only one threshold corresponding to the particle sublimation temperature. Since water was the host liquid for most of the samples in this study, the model was implemented based on a single threshold at the sublimation temperature of the nanoparticle (either carbon black or C_{60}). For the solution of C_{60} in toluene, the model was adapted for two activation thresholds: one at the boiling point of toluene and one at the sublimation temperature of C_{60}. The resulting layer-by-layer beam attenuation is assumed to follow the Beer-Lambert law with one of these two extinction coefficients.[136] This law may be expressed as either

$$I_{out} = I_{in} e^{-\alpha L}$$

or

$$I_{out} = I_{in}10^{-\alpha L},$$

where α is the extinction coefficient and L is the path length, depending on whether the extinction coefficient is defined in terms of the natural logarithm or in terms of log base 10.

The model assumes a circular flat-top beam profile. The irradiance does not change radially. It is treated as a uniform, average-irradiance disk. Some initial trials were run in which the beam was assumed to be collimated as the beam propagated through the material. For most of the modeling in this work, the radius was changed throughout the sample in order to approximate the experimental beam diameters measured as a function of distance along the propagation axis. The effective $1/e^2$ radius was measured at several positions and this data was analyzed via curve-fitting software to find an equation to approximate the beam diameter continuously for any z-position.

The model assumes a hyperbolic-secant-squared temporal pulse. This is used to approximate a Gaussian temporal pulse for reasons discussed below. Given a full-width-at-half-maximum (FWHM) Gaussian pulse width, the conversion to the equivalent hyperbolic-secant-squared FWHM pulse width (for equal integrated energy under the pulse) is:

$$t_{p\,hs} = t_{p\,Gaus}/\left(1.32856\left(\sqrt{2}\right)\right).$$

Given an input energy, E_{in}, and the beam radius in the focal zone of w_0, the amplitude factor for the irradiance (to give the correct integrated energy) is:

$$I_0 = E_{in}/\left([\pi\, {w_0}^2]\tau_{Gaus}\left[\sqrt{2\pi}\right]\right),$$

where

$$\tau_{Gaus} = t_{p\ Gaus}/\left(2\sqrt{2\log 2}\right)$$

is the time constant appearing in the analytical expression for a Gaussian that yields the correct FWHM pulse width.

The pulse is propagated through each spatial slice of the medium, keeping track of the irradiance incident on that slice, the resulting temperature rise, the extinction coefficient resulting from the current temperature-dependent phase of the particles in that slice, and the resulting decrement to the irradiance through that spatial slice according to the Beer-Lambert law. Note that since the specific heat is a function of temperature, this is updated at each calculation step.

The relationship between the temporal and spatial increment sizes depends on the velocity of light in the medium, according to:

$$\Delta t = \frac{\Delta z\, n_\lambda}{c},$$

where Δt is the time increment, Δz is the spatial increment in the direction of propagation, n_λ is the refractive index of the sample medium at the laser wavelength, and c is the speed of light in vacuum. This, however, is very computationally intensive, so this condition is not enforced prior to the generation of final data.

To determine what the layer thickness should be one can estimate the average inter-particle distance. The linear extinction coefficient, α_0, may be determined by a

transmission measurement at the laser wavelength and application of the Beer-Lambert law, according to:

$$\alpha_0 = -\frac{1}{L}\ln \mathcal{T}_\lambda,$$

where L is the sample path length and $\mathcal{T}_\lambda$ is the transmittance at the laser wavelength. Given information about the average particle size and complex refractive indices of the particle and surrounding medium, the absorption cross section, σ_{abs}, and scattering cross section, σ_{sca}, can be calculated via Mie theory. The extinction cross section for a particle is:

$$\sigma_{ext} = \sigma_{abs} + \sigma_{sca}.$$

The number density of particles in the medium may be estimated as:[137]

$$N = \frac{\alpha_0}{\sigma_{ext}}.$$

The average inter-particle distance may then be calculated as:

$$\mathrm{d} = \sqrt[3]{\frac{1}{N}}$$

and this distance may be used to set the layer thickness. Again, using these assumptions can be computationally intensive, so they are only used for generating final data.

7.3. Theory: Nonlinear Scattering (Alternate Model)

Unfortunately, the above model presents no method for estimating what the extinction coefficient should be. One must simply estimate its value from the experimental results. To overcome this shortcoming, a method was sought to estimate

the initial size of the bubble formed upon sublimation and from this to determine the extinction coefficient via Mie theory.

Based on a study of laser-irradiated gold nanoparticles in water, Egerev et al. present the following relation for estimating the initial radius of the vapor bubble around a nanoparticle that has been laser-heated above the threshold for boiling the surrounding liquid:[138]

$$R_0 = \left\{\frac{3}{4\pi\rho_{cl}}\left[\frac{(F-F_c)\sigma_{abs}}{E_{cl}}\right] + R_{np}^3\right\}^{1/3},$$

where R_0 is the initial bubble radius, ρ_{cl} is the critical density of the liquid, F is the fluence of the laser pulse, F_c is the critical fluence required to bring the liquid surrounding the nanoparticle to its boiling point, σ_{abs} is the absorption cross-section of the nanoparticle, E_{cl} is the internal energy of the liquid at the critical point, and R_{np} is the radius of the nanoparticle. At this point, the nanoparticle is assumed to still be intact, surrounded by a vapor bubble of boiled liquid.

Egerev gives the following equation for estimating the critical fluence for bubble formation:[138]

$$F_c = \frac{\chi_l \tau_L}{\sigma_{abs}} \frac{4\pi R_{np} c_l \rho_l T_b}{\left\{1+\frac{\xi_1}{\xi_2-\xi_1} erfcx\left(\xi_2\frac{\sqrt{\chi_l\tau_L}}{R_{np}}\right) - \frac{\xi_1}{\xi_2-\xi_1} erfcx\left(\xi_1\frac{\sqrt{\chi_l\tau_L}}{R_{np}}\right)\right\}},$$

where χ_l is the thermal diffusivity of the liquid, τ_L is the laser pulse length, c_l is the specific heat capacity of the liquid, ρ_l is the density of the liquid, and T_b is the boiling temperature of the liquid. The values for $\xi_{1,2}$ are given by:

$$\xi_{1,2} = \frac{3}{2}\left[\propto \mp\sqrt{\propto(\propto -4/3)}\right],$$

where

$$\alpha = \frac{c_l \rho_l}{c_{np} \rho_{np}}.$$

For short pulses ($\chi_l \tau_L << R_{np}^2$), the critical fluence relation simplifies to:

$$F_c = V_{np} c_{np} \rho_{np} T_b / \sigma_{abs},$$

where V_{np}, c_{np}, and ρ_{np} are the volume, specific heat capacity, and density of the nanoparticle. For long pulses ($\chi_l \tau_L >> R_{np}^2$), the critical fluence relation simplifies to:

$$F_c = 4\pi R_{np} c_l \rho_l T_b \chi_l \tau_L / \sigma_{abs}.$$

These expressions for the critical fluence assume a rectangular temporal pulse shape. For Gaussian temporal profiles of about 10 ns pulse width, the critical fluence is about two times that estimated for a rectangular pulse.[138] These expressions also assume that energy is absorbed by the particle during the entire pulse and that the excess energy beyond reaching the boiling temperature of the liquid goes into boiling more of the liquid surrounding the particle, creating a thicker vapor layer.

The relations above were used to estimate the size of the scattering center and the BHMIE subroutine was used to calculate the resulting extinction coefficient. As a first approximation, the bubbles were modeled as air in water, using a refractive index of 1 for the vapor. However, the model was also refined to treat the two layer concentric sphere (nanoparticle surrounded by vapor bubble) as a homogeneous sphere with an effective complex refractive index calculated via the Maxwell Garnett average dielectric function:[136]

$$\epsilon_{av} = \epsilon_m \left[1 + \left\{3f\left(\frac{\epsilon_i - \epsilon_m}{\epsilon_i + 2\epsilon_m}\right) / \left[1 - f\left(\frac{\epsilon_i - \epsilon_m}{\epsilon_i + 2\epsilon_m}\right)\right]\right\}\right],$$

where f is the volume fraction of the inclusion(s), ε_i is the dielectric permittivity of the inclusion (particle), ε_m is the dielectric permittivity of the medium (vapor bubble), and ε_{av} is the dielectric permittivity of the entire structure treated as one effective spherical particle. The complex refractive index can then be determined by:

$$N = c\sqrt{\epsilon\mu} = n + ik,$$

where N is the complex refractive index, c is the speed of light in vacuum, ε is the dielectric permittivity, μ is the magnetic permeability, n is the real part of the refractive index and k is the imaginary part of the refractive index. This complex refractive index for the effective particle can then be divided by the complex refractive index of the solvent to calculate the relative complex refractive index used in the BHMIE subroutine. From this and the size parameter, Mie calculations are then done via BHMIE to determine the resulting extinction coefficient. The size parameter is calculated as:

$$x = \frac{2\pi N R_0}{\lambda},$$

where x is the size parameter and λ is the laser wavelength.[136]

It should be noted for reference in discussions below that this model will produce estimates for scattering center sizes that increase as a function of input energy. Therefore, the corresponding extinction coefficients would be expected to increase as a function of input energy.

The following values were used for the numerical calculations in this investigation: E_{cl} = 2000 kJ/kg, ρ_{cl} = 322 kg/m^3, c_l = 4.18 kJ/(kg K), and χ_l = 1.4 x 10^{-7} m^2/s.[139]

7.4. Theory: Nonlinear Absorption

The dominant optical limiting mechanism in molecular solutions of C_{60} is reverse saturable absorption (RSA). RSA is a special case of excited state absorption (ESA) in which the absorption cross section of the excited state is much larger than the absorption cross section of the ground state, resulting in a decrease in transmittance with increasing input irradiance. RSA behavior is typically described by a five-level Jablonski diagram, as depicted in Figure 7-2.

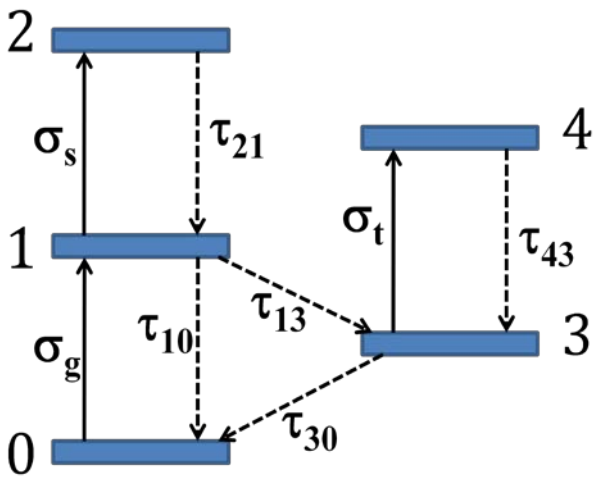

Figure 7-2. Jablonski diagram describing reverse saturable absorption (RSA).

At any instant and spatial location, the absorption is dictated by the population densities of each of these five energy bands. The dynamics of the population densities are related by a set of rate equations that take into account the absorption cross-sections of the optical transitions and the decay rates between bands. In most modeling of RSAs, a three-level approximation of this model is used, since the decay rates from the upper singlet and triplet excited states far exceed the rates at which they are populated by

absorption transitions, and thus these upper level populations may be ignored. The rate equations describing this three-level approximation are:

$$\frac{dN_0}{dt} = -\frac{\sigma_g I(t)}{\hbar\omega} N_0 + \frac{N_1}{\tau_{10}}$$

$$\frac{dN_1}{dt} = \frac{\sigma_g I(t)}{\hbar\omega} N_0 - \frac{N_1}{\tau_1}$$

$$\frac{dN_3}{dt} = \frac{N_1}{\tau_{13}}$$

where $N_{0,1,3}$ are the population densities in the ground, first excited singlet, and first excited triplet states, $\sigma_{g,s,t}$ are the ground-state, singlet excited-state, and triplet excited-state absorption cross sections, $\tau_{10,21,43,30}$ are the respective band lifetimes, τ_{13} is the inter-system crossing lifetime, and

$$\frac{1}{\tau_1} = \frac{1}{\tau_{10}} + \frac{1}{\tau_{13}}.$$

Kobyakov et al. have developed analytical solutions to describe the dynamics of these band populations and the model set forth here makes use of those relationships to reduce computational complexity.[140] Their solutions use the following notations to normalize the variables:

$$T = t/t_p,$$

where t_p is the temporal pulse width,

$$A = \sigma_g I_0 \, t_p/(\hbar\omega)$$

and

$$w = t_p/\tau_1.$$

The rate equations become:

$$\frac{dn_0}{dT} = -f(T)n_0 + w(1-\phi)n_1$$

$$\frac{dn_1}{dT} = f(T)n_0 - wn_1$$

$$\frac{dn_3}{dT} = w\phi n_1$$

where $n_j(T) = N_j(T)/N_0(T_0)$, j = 0, 1, 3, are fractional population densities, T_0 is the time when the light pulse begins to enter the material, and $\phi = \tau_1/\tau_{13}$ is the triplet quantum yield. The pulse is represented by $f(T) = A\hat{f}(T)$, where $\hat{f}(T)$ is a pulse shape with unit amplitude, given in the normalized time scale. The total population density is conserved, so:

$$n_0(T) + n_1(T) + n_3(T) = 1.$$

For mathematical convenience (because it lends itself more easily to the analytical derivation of Kobyakov), the hyperbolic-secant-squared function is used to approximate Gaussian temporal pulses, so the input pulse is described by:

$$f(T) = A\,\mathrm{sech}^2\,T.$$

The analytical solution derived for long pulses (≥ 10 ns), assuming hyperbolic-secant-squared input, is:

$$n_0(T) \approx \exp\left[-\phi A(\tanh T + 1)\right]$$

$$n_1(T) \approx \frac{A}{w}\mathrm{sech}^2\,T \exp[-\phi A(\tanh T + 1)].$$

This model uses the irradiance incident on each slice of the material to derive the population densities using the analytical expressions above. In general, the irradiance

will be a function of spatial coordinate in the beam cross-section as well (the size of which will change with propagation), but for simplicity this model assumes a uniform irradiance profile at each slice.

The population densities determine an effective absorption cross-section:

$$\sigma_{eff} = n_0 + \bar{\sigma}_S n_1 + \bar{\sigma}_T n_3$$

where $\bar{\sigma}_S = \sigma_s/\sigma_g$, $\bar{\sigma}_T = \sigma_t/\sigma_g$, σ_g is the ground state absorption cross-section, σ_s is the first excited singlet state absorption cross-section, and σ_t is the first excited triplet state absorption cross-section at a given wavelength. The population densities, and consequently the effective absorption cross-section, are functions of both time and distance along the propagation direction through the material.

The irradiance at each point in time and space is calculated according to the Beer-Lambert law, with the formulation:

$$I_{out} = I_{in} e^{-\sigma_{eff} dZ} ,$$

where dZ is a normalized spatial step in the propagation direction. The temperature at each point in time and propagation space is determined as described in section 0, with (σ_{eff} σ_g) replacing σ_{abs} in the equations. (The effective absorption cross-section as defined above is a normalized, unitless parameter and must be multiplied by the ground state absorption cross-section in the thermodynamic calculation.) The specific heat is approximated to be the same as that of graphite, and is updated at each calculation step as a function of the current temperature. If the sublimation temperature of C_{60} is exceeded, then the material is assumed to enter a scattering state and the irradiance equation is replaced by:

$$I_{out} = I_{in} e^{-\alpha_B dz} ,$$

where

$$\alpha_B = -\ln(\text{Ŧ}_B)/L ,$$

Ŧ_B is the transmittance of the material when it is fully in the scattering state, dz is a spatial step in the propagation direction, and L is the path length of the material.

7.5. Theory: Nonlinear Scattering from Nonlinearly Absorbing Particles

To estimate the response of particles composed of RSA molecules, such as colloidal C_{60}, a combination of the two approaches above is used. The aforementioned method based on the analytical solutions published by Kobyakov is used to model the absorption dynamics prior to sublimation of the particles.[140] After the particle temperature exceeds the sublimation temperature, attenuation of irradiance is modeled according to the nonlinear scattering method based on the published work of McEwan.[8] The sublimation temperature is assumed to be that of C_{60} (800 K).[112]

When the material is in the nonlinear absorbing state, all molecules in each colloid are assumed to participate in the absorption, since the particles of concern are assumed to be within the size regime where treatment as volumetric absorbers is reasonable. Therefore, the absorption calculations (and in particular the population densities) are treated on a per-molecule basis.

For this simple model, the absorption cross sections of molecular C_{60} are used. This will introduce some error into the model, since the ground state absorption cross section does change slightly upon colloid formation, as evidenced by the ground state

absorption spectrum. However, this is a reasonable first approximation. Likewise, the decay rates will be different upon colloid formation since some quenching processes are to be expected due to the close proximity of the C_{60} molecules to each other. This is accounted for by using rates from the transient absorption spectroscopy experiments for C_{60}-1 and approximating them for C_{60}-2 and C_{60}-3.

Although the RSA rate equations are done on a per molecule basis, the thermodynamic considerations take into account the heating of each particle as a whole. Since the particles are treated as volumetric absorbers, the effective absorption cross-section, σ_{eff}, as described in section 7.4. must be multiplied not only by σ_g but also by the number of C_{60} molecules within the colloid particle, N_{mp}. The atomic packing factor of the face-centered-cubic (FCC) structure (the most common structure for colloidal C_{60}) is 0.74. The number of molecules in a unit cell of FCC-packed C_{60} is:

$$N_{m\_uc} = APF\,\frac{V_{uc}}{V_m},$$

where V_{uc} is the volume of the unit cell and V_m is the volume of the C_{60} molecule. A C_{60} molecule has a radius of R_m = 0.88 nm. The volume of an FCC unit cell is:

$$V_{uc} = 22.62\,R_m^3.$$

The number of molecules in a particle, N_{mp}, is:

$$N_{mp} = N_{m\_uc}\,\frac{V_{np}}{V_{uc}},$$

where V_{np} is the volume of the colloidal nanoparticle.

7.6. Model Validation and Predictions

To check the models, they were compared to published data. For carbon black suspensions, input parameters were chosen to agree with the published work of Riehl and Fougeanet.[4, 5] An incident wavelength of 1064 nm was chosen to match the literature account. The refractive index of water at 1064 nm is 1.325. The particle radius was set at 85 nm. The absorption cross-section of carbon black in water is $1.033\ 10^{-14}$ m^2 for a particle of this radius at this wavelength, as calculated by Mie theory. The mass density of carbon black was 1800 kg/m^3. The sublimation temperature of carbon black is 3770 K. The fluence threshold for a carbon black particle to sublime near the peak of the laser pulse was given as 0.62 J/cm^2.[5] The input energy was chosen as 7.8 μJ and the beam focal radius was chosen as 20 μm to match this fluence and a collimated geometry was assumed. The laser pulse width was 10 ns FWHM hyperbolic-secant-squared, approximating a Gaussian. The initial temperature was assumed to be 298.16 K (25 degrees Celsius). The linear transmittance at the modeled wavelength was chosen to be 70% through a 2 mm path length. A transmittance in the nonlinear regime of 10% was arbitrarily chosen to represent the case of all layers having sublimed and transitioned to nonlinear scattering state. This assumption was made for all examples in this section, as they are all hypothetical. Figure 7-3 shows the results of the model.

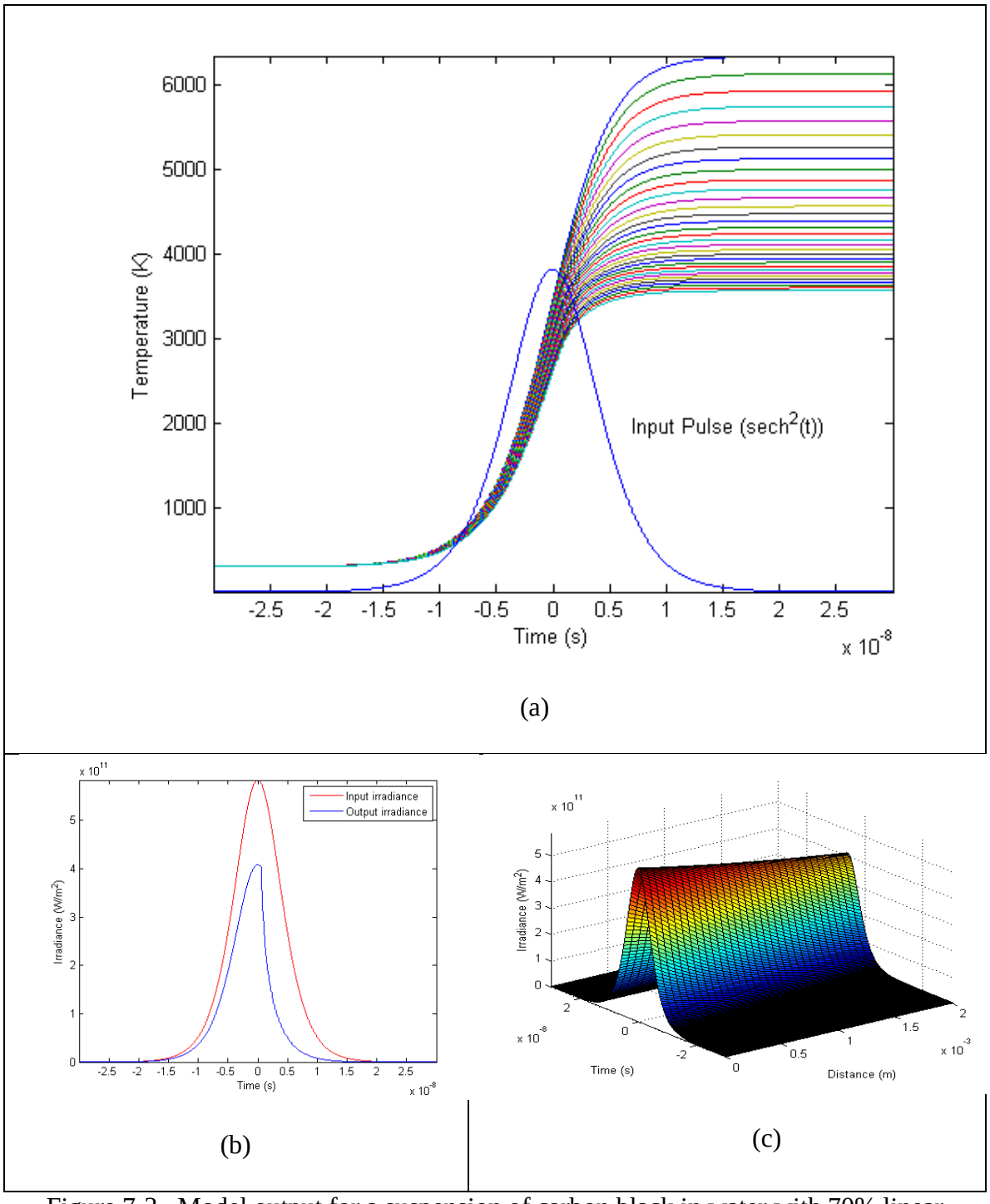

Figure 7-3. Model output for a suspension of carbon black in water with 70% linear transmittance at 532 nm through a 2 mm path length with 7.8 microJoules input energy, 20 micron spot radius, and 10 ns pulse width. (a) isolated particle temperature vs. time, (b) input and output pulse irradiance vs. time, and (d) surface plot showing the irradiance profile as the beam propagates through the material.

Figure 7-3(a) corresponds very well with Figure 4 of Riehl and Fougeanet's work.[5] The multi-colored lines represent the temperature at different slices along the propagation direction. The temperature of the particles in the first layer of the suspension reaches the sublimation temperature of 3770 K slightly after the peak of the pulse, agreeing with Riehl and Fougeanet's calculation of threshold. Note that deeper layers do not get as hot as the input layer, as expected, because some irradiance has been subtracted from the pulse by the time it reaches those layers. Figure 7-3(b) shows that the transmittance of the material rapidly goes down as more and more layers reach the sublimation threshold and begin to participate in bubble scattering. Figure 7-3(c) shows the irradiance as a function of time and propagation distance through the material.

The transmittance of the pulse energy in this case was 51.3%.

A solution of C_{60} was modeled for direct comparison using the same path length, linear transmittance, scattering-state transmittance, focal spot radius, pulse length, and input energy. Note that C_{60} has a very low solubility in water, so it is not possible to achieve a concentration yielding 70% linear transmittance in a 2 mm path. But, again, this is a simplified model which does not treat the dynamics of heat transfer from the particle to the liquid, and thus these results can be applied to approximate the behavior of C_{60} in liquids in which it has a higher solubility, such as toluene. The wavelength was assumed to be 532 nm, since data is readily available in the literature for the absorption cross-sections and decay rates of the states at that wavelength. The values used are listed in Table 7-1.[31]

Table 7-1. Lifetimes and Cross-sections for C_{60} RSA Dynamics at 532 nm.

Ground state absorption cross-section	$2.87\ 10^{-22}\ m^2$
1^{st} excited singlet absorption cross-section	$1.57\ 10^{-21}\ m^2$
1^{st} excited triplet absorption cross-section	$9.22\ 10^{-22}\ m^2$
Lifetime of the 1^{st} excited singlet state	$30\ 10^{-9}$ s
Inter-system crossing lifetime from singlet to triplet	$1.2\ 10^{-9}$ s

The refractive index of water at 532 nm is 1.33538 at 20 degrees Celsius.[141]

The same initial temperature was assumed. The mass density of C_{60} is 1720 kg/m^3. The sublimation temperature of C_{60} is 800 K.[112] As an approximation, the same relationship between specific heat and temperature as that of carbon black was assumed.

Figure 7-4 shows the output of the model.

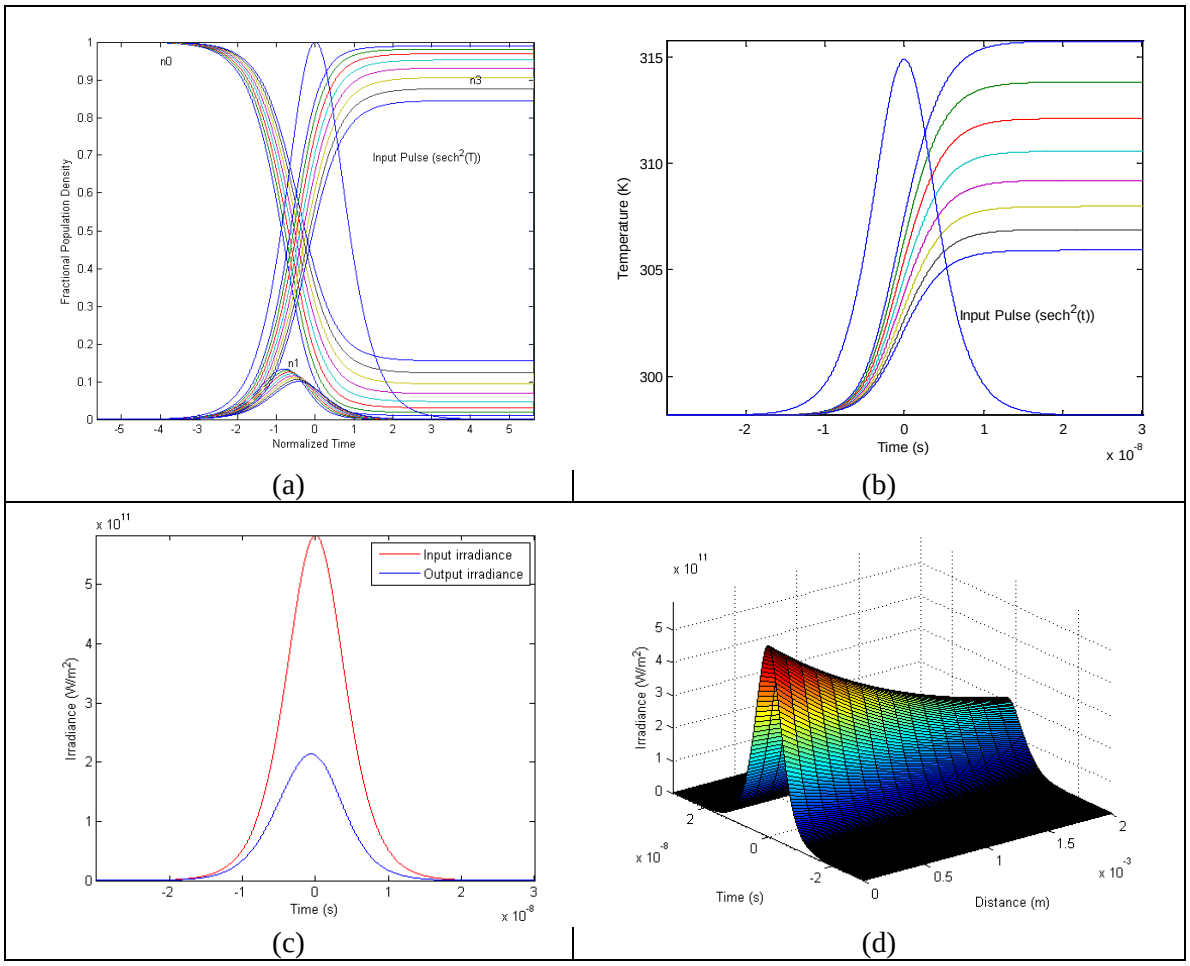

Figure 7-4. Model output for a solution of C_{60} with 70% linear transmittance at 532 nm through a 2 mm path length with 7.8 microJoules input energy, 20 micron spot radius, and 10 ns pulse width. (a) Fractional population density vs. normalized time, (b) isolated molecule temperature vs. time, (c) input and output pulse irradiance vs. time, and (d) surface plot showing the irradiance profile as the beam propagates through the material.

Figure 7-4(a) shows the expected behavior of the fractional population densities of the states. The population starts out entirely in the ground state, is absorbed into the first excited singlet state, and then rapidly transitions into the first excited triplet state, where it remains for a long time (on the order of microseconds). The population of the singlet state is small and short-lived due to the high triplet quantum yield and the low inter-system crossing lifetime. The behavior in this plot agrees well with several figures

in Kobyakov.[140] Figure 7-4(b) shows that at this input energy, the molecules heat up, but minimally. This is because the absorption cross-sections of the C_{60} molecule are much smaller than that of the previously modeled carbon black particles. As before, the deeper layers into the material are heated less due to the depletion of the beam's irradiance. Figure 7-4(c) shows a smooth attenuation of the input beam at this input energy, with slightly more attenuation present later in the pulse, when the triplet state has been fully populated. Figure 7-4(d) shows the irradiance as a function of time and propagation distance through the material.

The transmittance of the pulse energy in this case was 40.4%.

A suspension of C_{60} colloids was modeled for direct comparison using the same path length, linear transmittance, scattering-state transmittance, focal spot radius, pulse length, and input energy. The wavelength was assumed to be 532 nm, and the data in Table 7-1 for the absorption cross-sections and decay rates of the states of C_{60} at that wavelength were used. (Quenching was not taken into account for this notional example.)

A particle radius of 85 nm was assumed, for comparison with the carbon black result above. The same initial temperature was assumed. The mass density and sublimation temperature were assumed to be the same as C_{60}. The same relationship between specific heat and temperature was assumed.

Figure 7-5 shows the output of the model.

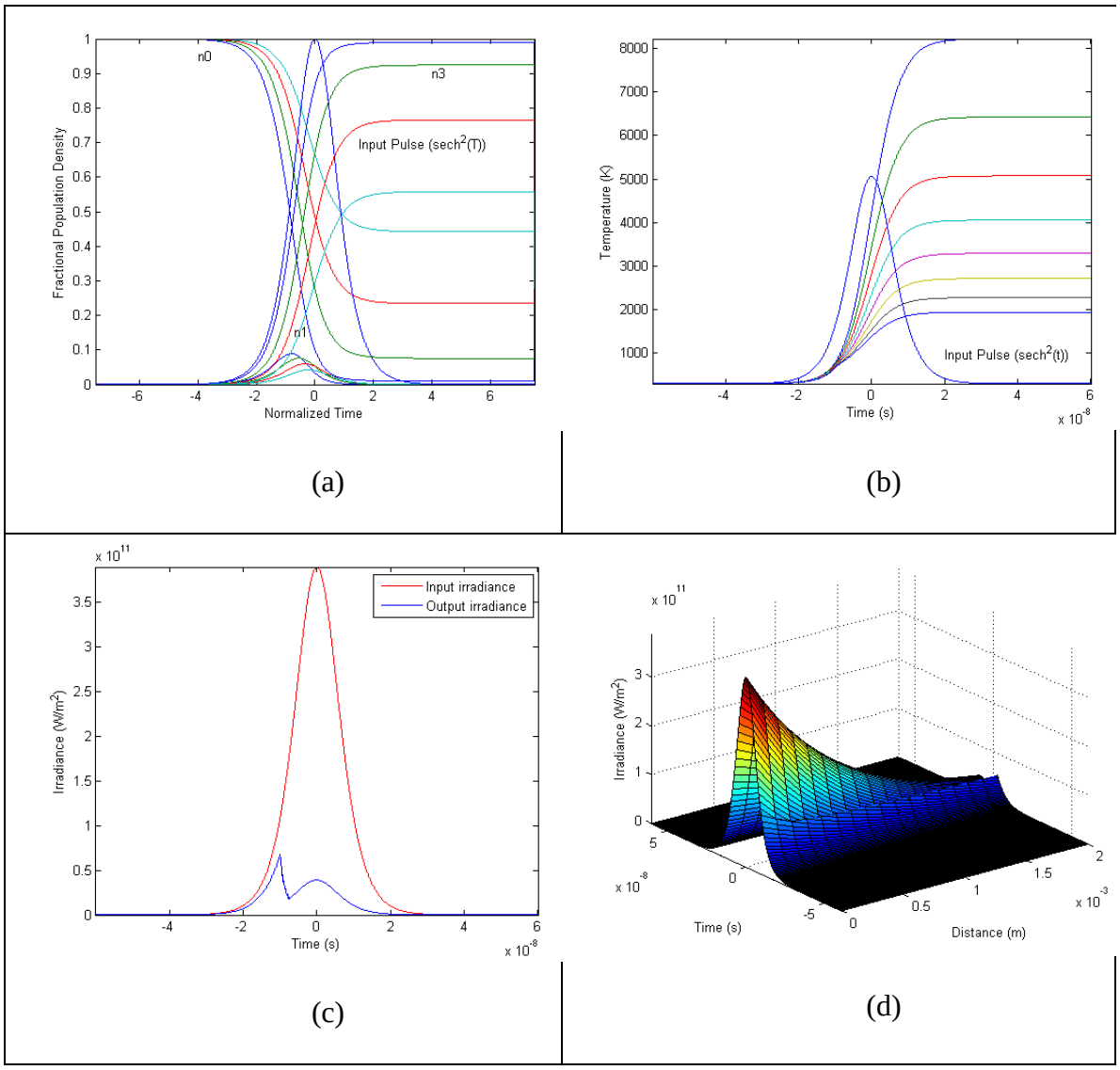

Figure 7-5. Model output for a suspension of C_{60} colloids in water with 70% linear transmittance at 532 nm through a 2 mm path length with 7.8 microJoules input energy, 20 micron spot radius, and 10 ns pulse width. (a) Fractional population density vs. normalized time, (b) isolated particle temperature vs. time, (c) input and output pulse irradiance vs. time, and (d) surface plot showing the irradiance profile as the beam propagates through the material.

Figure 7-5(b) shows that, at this energy, all layers in the material reach the sublimation threshold before the peak of the pulse. This is due to stronger absorption from the RSA behavior of C_{60} in comparison to the carbon black suspension and because

of the larger particle size when comparing the colloidal particle to the C_{60} molecule. (Note that this hypothetical case assumed that all of the absorbed light was converted to heat and that the experimental results seem to indicate that C_{60} colloids with higher triplet quantum yield appear to be less efficient at reaching the sublimation temperature than C_{60} colloids with lower triplet quantum yields. But, also keep in mind that C_{60} has a lower sublimation temperature than carbon black.) Figure 7-5(a) shows that the deeper layers in the sample are screened by the early attenuation of irradiance, resulting in them being less fully populated into the triplet state. The peaky feature in the transmitted irradiance in Figure 7-5(c) indicates the region of time where the colloids vaporize sublime and the dominant mechanism transitions from RSA to nonlinear scattering. Figure 7-5(d) shows the irradiance as a function of time and propagation distance through the material.

The transmittance of the pulse energy in this case was 15.1%.

Figure 7-6 shows the model output for a carbon black suspension with the same parameters, but at ten times the previous input energy. The transmittance of the pulse energy was 14.2%.

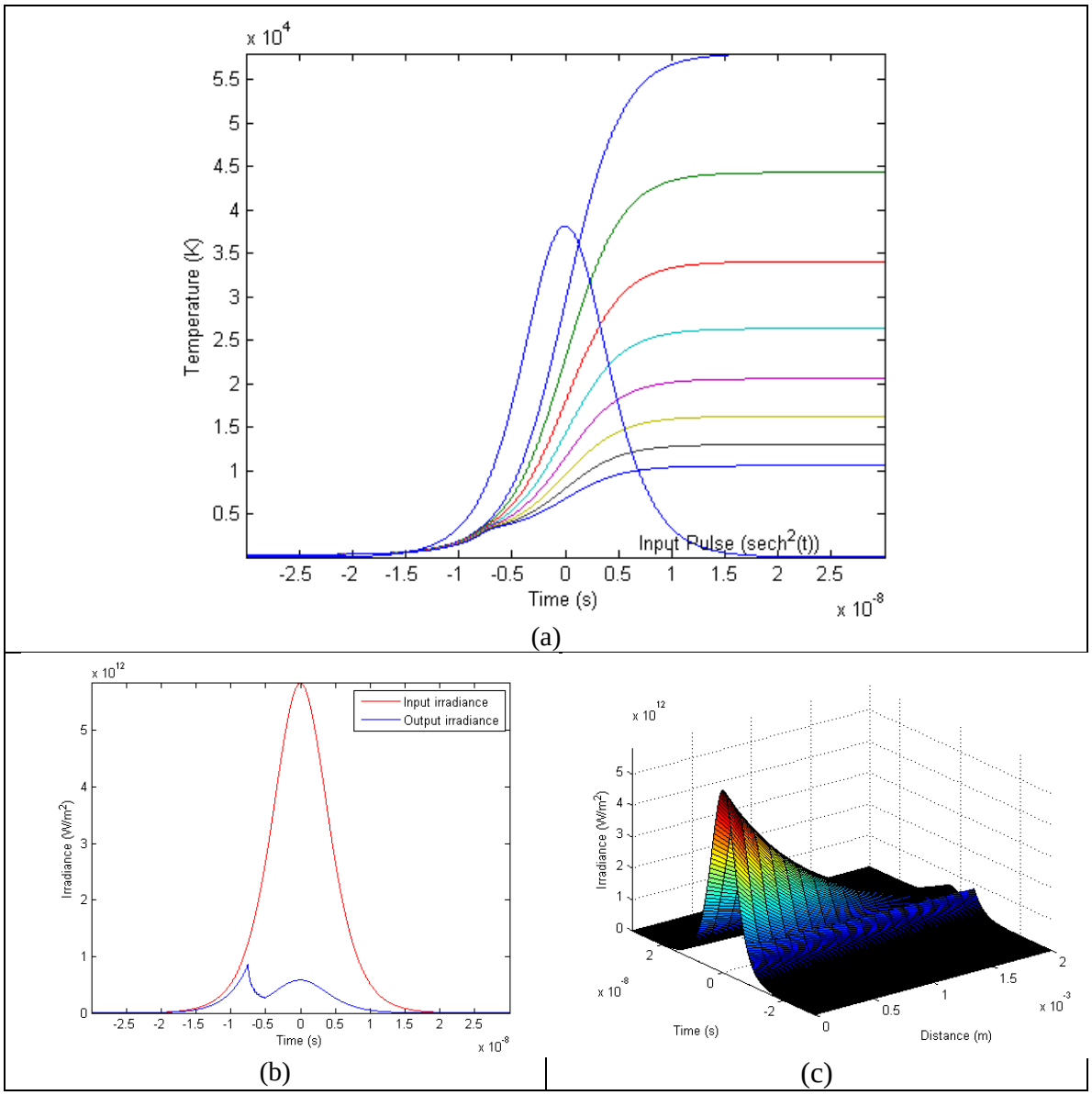

Figure 7-6. Model output for a suspension of carbon black in water with 70% linear transmittance at 532 nm through a 2 mm path length with 78 microJoules input energy, 20 micron spot radius, and 10 ns pulse width. (a) isolated particle temperature vs. time, (b) input and output pulse irradiance vs. time, and (d) surface plot showing the irradiance profile as the beam propagates through the material.

As can be seen by the inflection point in Figure 7-6(a) and the peaky feature in Figure 7-6(b), particle sublimation occurs much earlier in this higher energy pulse. Comparing Figure 7-6(b) to Figure 7-5(c), the gentler roll-off from the output irradiance

peak here indicates that the deeper layers are reaching sublimation more slowly than above in the colloidal C_{60} case. (Again, note that the above notional case assumed that RSA would make heating more efficient and does not take into account the observed behavior in the experimental data to the contrary.)

Figure 7-7 shows the model output for a 78 microJoule pulse into a C_{60} solution. The transmittance of the pulse energy was 32.5%.

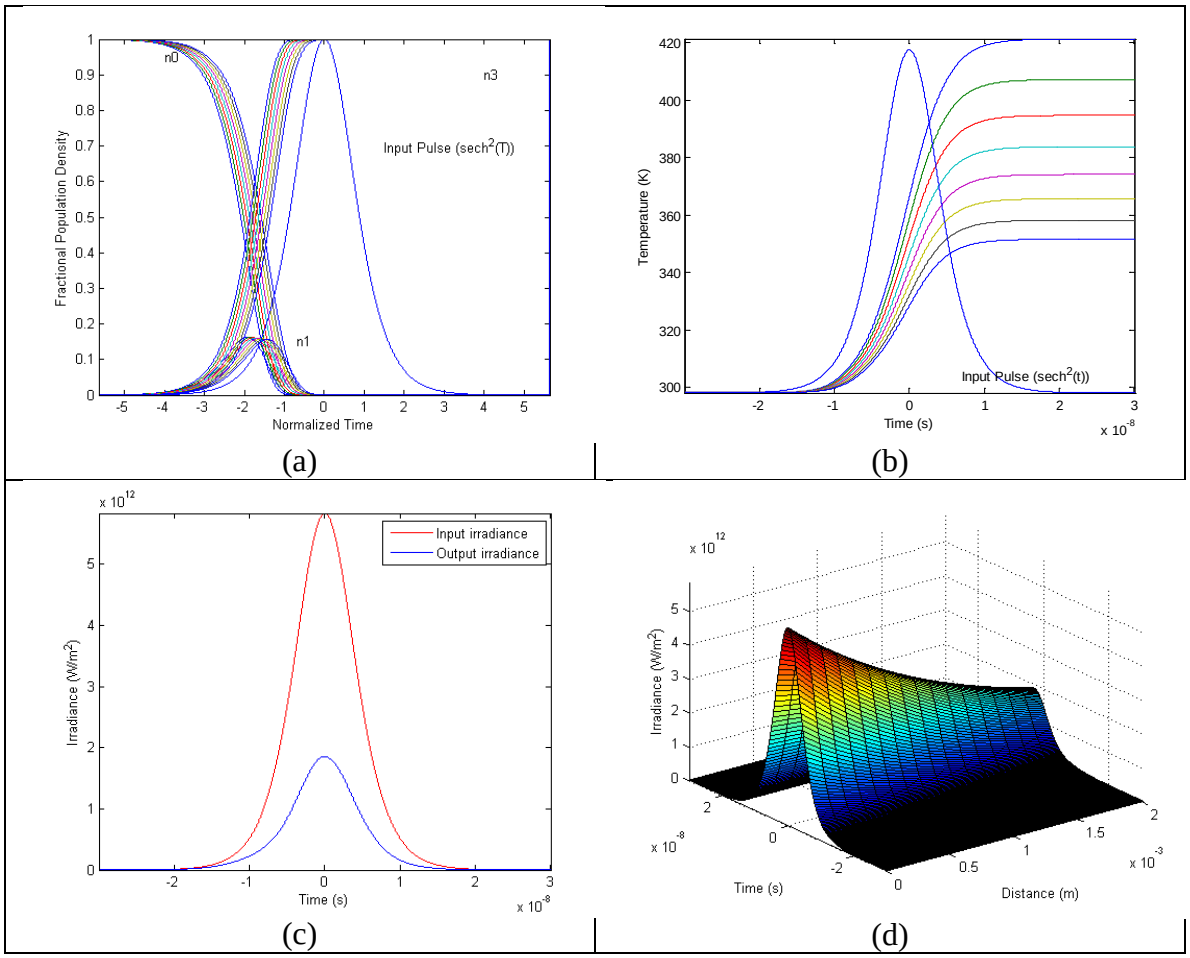

Figure 7-7. Model output for a solution of C_{60} with 70% linear transmittance at 532 nm through a 2 mm path length with 78 microJoules input energy, 20 micron spot radius, and 10 ns pulse width. (a) Fractional population density vs. normalized time, (b) isolated molecule temperature vs. time, (c) input and output pulse irradiance vs. time, and (d) surface plot showing the irradiance profile as the beam propagates through the material.

Figure 7-7(a) shows that the population is driven to the triplet state much earlier in the pulse at this higher energy. However, Figure 7-7(c) shows that the transmittance has not been significantly reduced compared to the lower energy case. (Note that the ratio of the absorption cross-sections of the first excited triplet state and the ground state is about 3 to 1. Thus, with the triplet state almost fully populated, the transmitted irradiance is about 1/3 of the incident irradiance.) Figure 7-7(b) shows that the molecules are heating up, but have not yet reached the sublimation temperature at this input energy. Scattering has been noted as a contributing factor to the optical limiting performance of C_{60} solutions, however this notional case predicts that the NLS mechanism does not contribute until higher energies are reached.

Figure 7-8 shows the model output for a suspension of C_{60} colloids in water for a 78 microJoule pulse. The transmittance of the pulse energy was 10.5%.

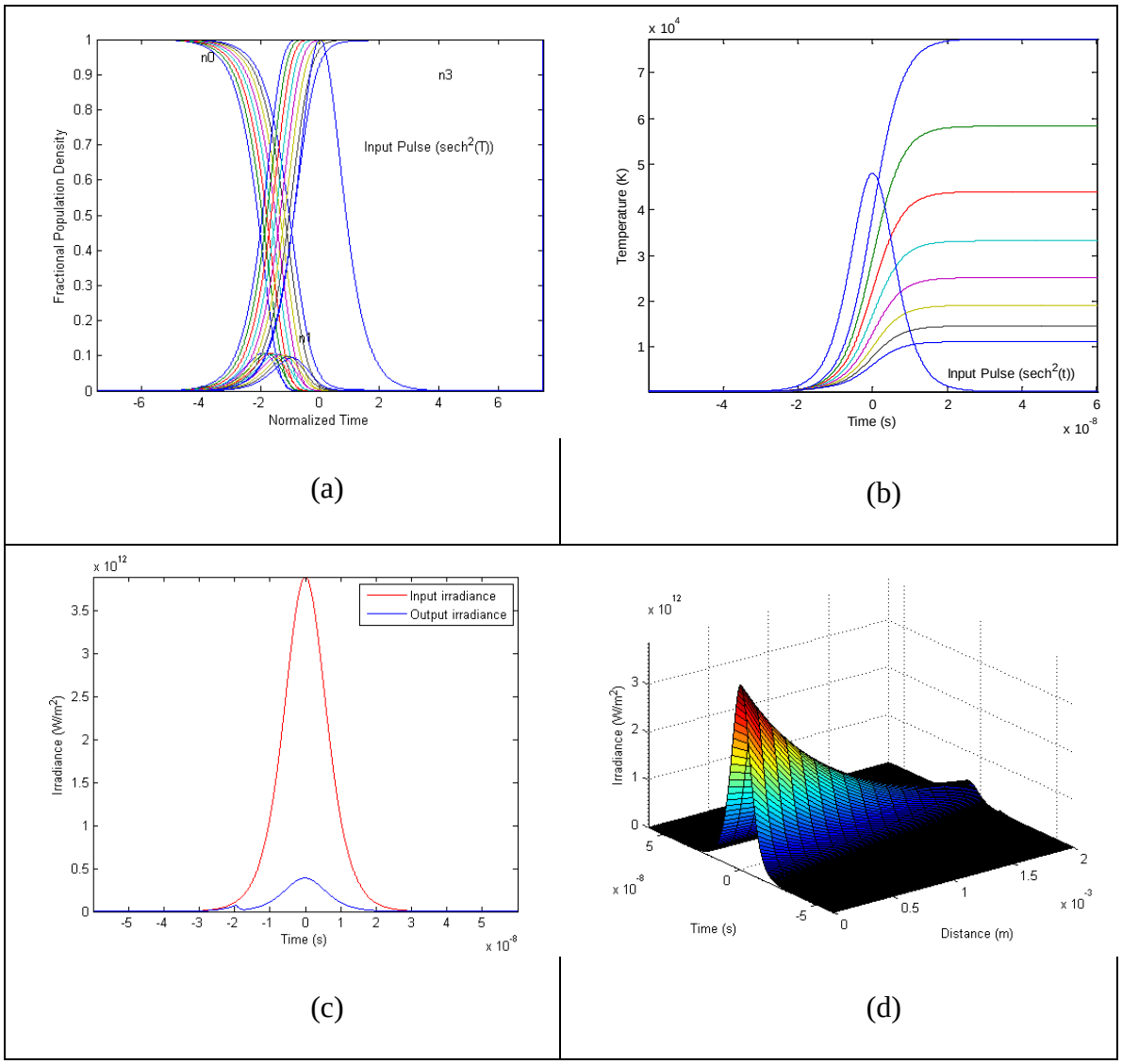

Figure 7-8. Model output for a suspension of C_{60} colloids in water with 70% linear transmittance at 532 nm through a 2 mm path length with 78 microJoules input energy, 20 micron spot radius, and 10 ns pulse width. (a) Fractional population density vs. normalized time, (b) isolated particle temperature vs. time, (c) input and output pulse irradiance vs. time, and (d) surface plot showing the irradiance profile as the beam propagates through the material.

Figure 7-8(a) indicates that the population is driven into the triplet state very early, along the rising edge of the pulse. Figure 7-8(b) and Figure 7-8(c) show that the sublimation temperature is reached very early in the pulse and that contribution of the

leading edge of the pulse toward the total transmitted energy is significantly reduced compared to the equivalent carbon black particle.

7.7. Modeling Analysis of Total Scattering Experimental Results

In order to compare the output of the models to the total scattering experimental data, a loop was added to vary the input energy over the same range as the experimental input energies.

The following numerical values were used in the modeling. In all cases, the FWHM Gaussian pulse width was assumed to be 10 ns. The density of carbon black was assumed to be 1800 kg/m^3 and the density of C_{60} was assumed to be 1720 kg/m^3. The sublimation temperature of carbon black was assumed to be 3770 K and the sublimation temperature of C_{60} was assumed to be 800 K. The wavelength was 560 nm. The complex refractive index of water at 560 nm was taken as $1.334320952 + 2.8693937 \times 10^{-9}i$.[141, 142] The complex refractive index for carbon black was assumed to be $1.84 + 0.85i$.[115] The complex refractive index of C_{60} was assumed to be $2.2 + 0.06i$.[112, 114]

Figure 7-9 shows the output of the models compared to the CBS-1 data. As a first approximation, the basic nonlinear scattering model was run in a collimated geometry using the experimental transmittance at the highest input energy to determine the value of the high-energy extinction coefficient. The model was run for different beam diameters. The model agreed with the experimental activation threshold when a $1/e^2$ beam radius of 30 μm was selected, but the shape of the transmittance curve did not agree. When the model was modified such that the $1/e^2$ beam radius varied as a function of position along the axis of propagation according to the experimental measurements, the shape of the

curve matched the experimental data, but the activation threshold was too low. This discrepancy is likely due to the fact that one of the simplifying assumptions of the model is that the particles are completely thermally isolated. In reality, they do dissipate heat to the surrounding medium, and thus it takes more energy to raise them to the sublimation temperature than a thermally isolated model would predict.[138] To compensate for this, a "heating efficiency factor" (HEF) was added to the model and adjusted until the model output agreed with the experimental data. The correction factor necessary to match the CBS-1 data was a factor of 1/8. With this correction, the model fit the experimental data extremely well.

Finally, a version of the model that used the input energy to estimate the initial size of the bubble created upon sublimation and then calculated the extinction coefficient based on the Mie scattering properties of a vapor bubble in the medium of the predicted size was run. This did not agree with the experimental data very well at all. The method drawn from the literature that was used to estimate the initial bubble size appears to overestimate the size of the bubbles dramatically and predicts more attenuation than was achieved in the experiment. In addition, the bubble model did not include a heating efficiency factor, so the activation threshold is also skewed.

An important insight is gleaned from these data. The basic nonlinear scattering model uses a single extinction coefficient that is independent of input pulse energy. This implies that there is a characteristic size to the scattering center that is formed and that, once created, the remaining energy in the input pulse is not strongly coupled into it to effect further growth. The relation given by Egerev for estimating the initial bubble size

resulting from an irradiated nanoparticle assumes that all of the energy in the pulse goes into creating the bubble, which is why this model fails to accurately fit the experimental data. The shape of the transmittance curve after the activation threshold has been reached is related to more and more layers in the focal volume reaching the sublimation threshold and taking on the higher NLS extinction coefficient, taking into account the fact that deeper layers are shielded by the attenuation resulting from the linear and nonlinear extinction of previous layers.

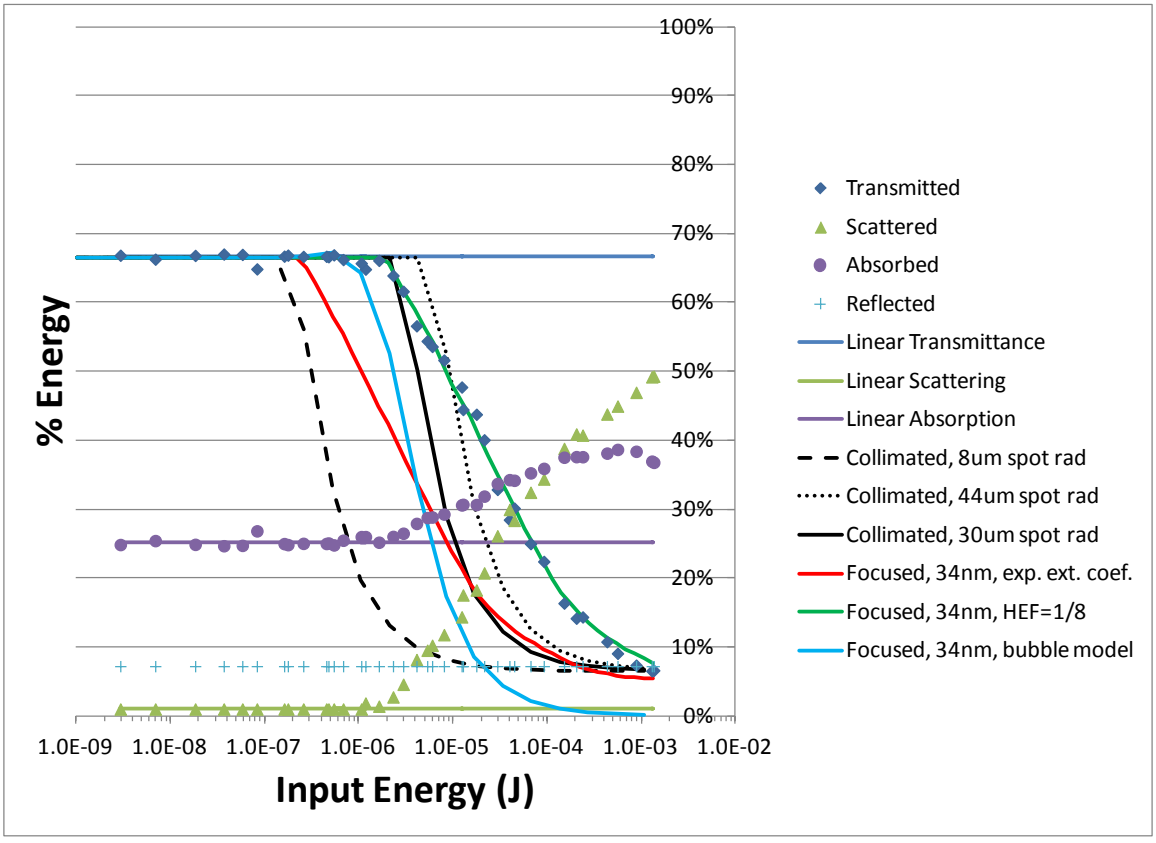

Figure 7-9. Modeling Results for CBS-1.

Figure 7-10 shows the modeling results compared to the experimental data for CBS-2. Because of CBS-2's less than ideal particle size distribution, the results are not

straightforward to interpret. Starting with a simple collimated model and using the 30 μm beam radius that fit the threshold behavior of CBS-1 (and the RSA behavior of C_{60} in toluene) quite well, different particle sizes were modeled and the activation threshold examined. The particle size distribution was bimodal with peaks at 102 and 1600 nm diameter on a number basis according to DLS. So, these two sizes were modeled. Neither of these sizes seemed to compare well with the experimental activation threshold. Rather, this was best matched in the model by particle diameter of 500 nm. Any of these sizes could be fit to the experimental results as long as a compensating factor was applied to account for the fact that the particles are not truly thermally isolated. The general trend is that smaller particles require a smaller HEF ratio to fit the observed activation threshold. The reader should keep in mind that these samples (particularly CBS-2) have broad particle size distributions and that the model assumes a monodisperse particle size. Although clear conclusions are hard to draw due to the makeup of this sample, the modeling results tend to point toward a view that the light interacts predominantly with the larger mode in the size distribution in this sample. As with CBS-1, the Mie-based bubble model is a poor fit to the experimental data, predicting far too much attenuation. It should be pointed out that the larger particle sizes in the CBS-2 distribution are much larger than the skin depth of electromagnetic penetration of carbon black for visible light, which violates the model's assumption that the particles can be treated as volumetric absorbers. So, one should not form any strong conclusions based on this particular sample's modeling analysis. The only strong conclusion one can make is that the nonlinear scattering behavior is best fit assuming a single extinction coefficient for the

NLO region, which implies that the scattering centers are to first order independent of the input pulse energy, so long as the threshold energy has been exceeded.

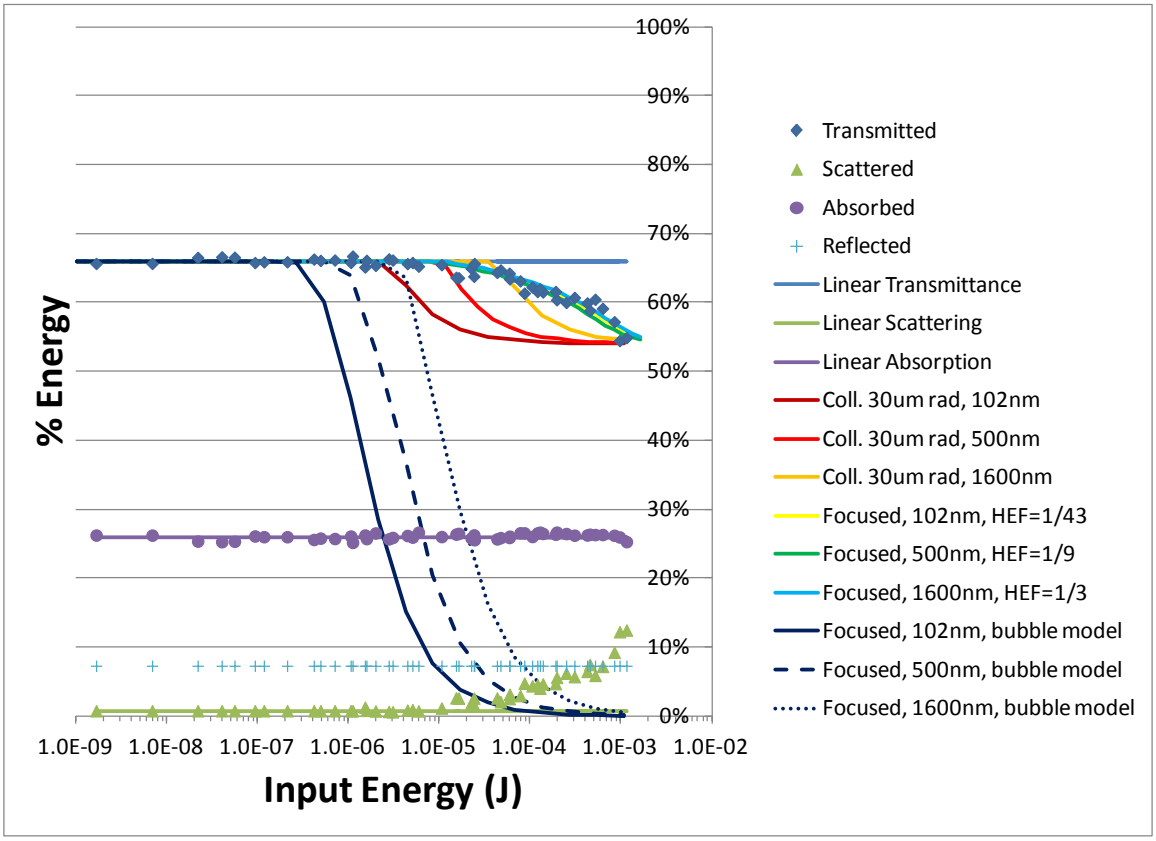

Figure 7-10. Modeling Results for CBS-2.

Figure 7-11 shows the modeling results for a solution of C_{60} in toluene. Briefly examining the model's output assuming a collimated beam with a 30 µm radius, a fairly good fit to the experimental data is found, lending credence to the approach taken in the analysis of the CBS-2 data to estimate an "effective" particle diameter of 500 nm as somewhat representative of the overall size distribution. Taking into account the focal geometry, the experimental data matches the theory for pure RSA behavior extremely well up to about 20 µJ. After this, the transmittance breaks below the predicted RSA

behavior. This corresponds to two regions of mild and stronger nonlinear scattering. Invoking the hybrid RSA-driven nonlinear scattering model and assuming the molecular diameter of 0.88 nm as the equivalent particle size, either section of nonlinear scattering can be fit to the model with an appropriate HEF compensation factor. Without appropriate thermal compensation factors, the model predicts sublimation at much lower input energies than observed. Using 1/600 as the HEF and accounting for the boiling point of toluene and the sublimation temperature of C_{60}, 384 K and 800 K, respectively, a good fit to the two separate regions of nonlinear scattering is obtained. Thus, the interpretation that the first section of nonlinear scattering may be attributed to the formation of vapor bubbles in toluene and that the second section of nonlinear scattering may be attributed to sublimation of individual C_{60} molecules, forming stronger scattering centers, appears to be reasonable. The necessary compensation factor of 1/600 is quite dramatic. However, whereas the assumption of thermal isolation may be somewhat valid for large particles, it is not a valid assumption for individual molecules in solution. So, significant correction is to be expected. Also, as will be discussed below, there seems to be some evidence pointing to an interpretation that populations in the triplet band contribute somewhat less to heating than populations in the singlet state. Molecular solutions of C_{60} have a triplet quantum yield near unity, so this would also point towards a smaller HEF. In addition, fluorescence and phosphorescence could consume a portion of the electron population that would otherwise go into generating heat. Likewise, the triplet state is long-lived and electron population in this state would not be available for generating heat via decay to the ground state until well after the duration of the input

pulse. So, such extreme compensation factors may not be completely outlandish. One thing is certain: the observed behavior is consistent with pure RSA followed by two regions of nonlinear scattering with successively higher attenuation coefficients. Like the carbon black suspensions, these regions of nonlinear scattering are each best fit with a single extinction coefficient, indicating that there is a characteristic scattering center size that is independent of the input energy. (Once formed, the pulse is only weakly coupled to it and does not deposit enough energy after the phase change to cause it to grow significantly.)

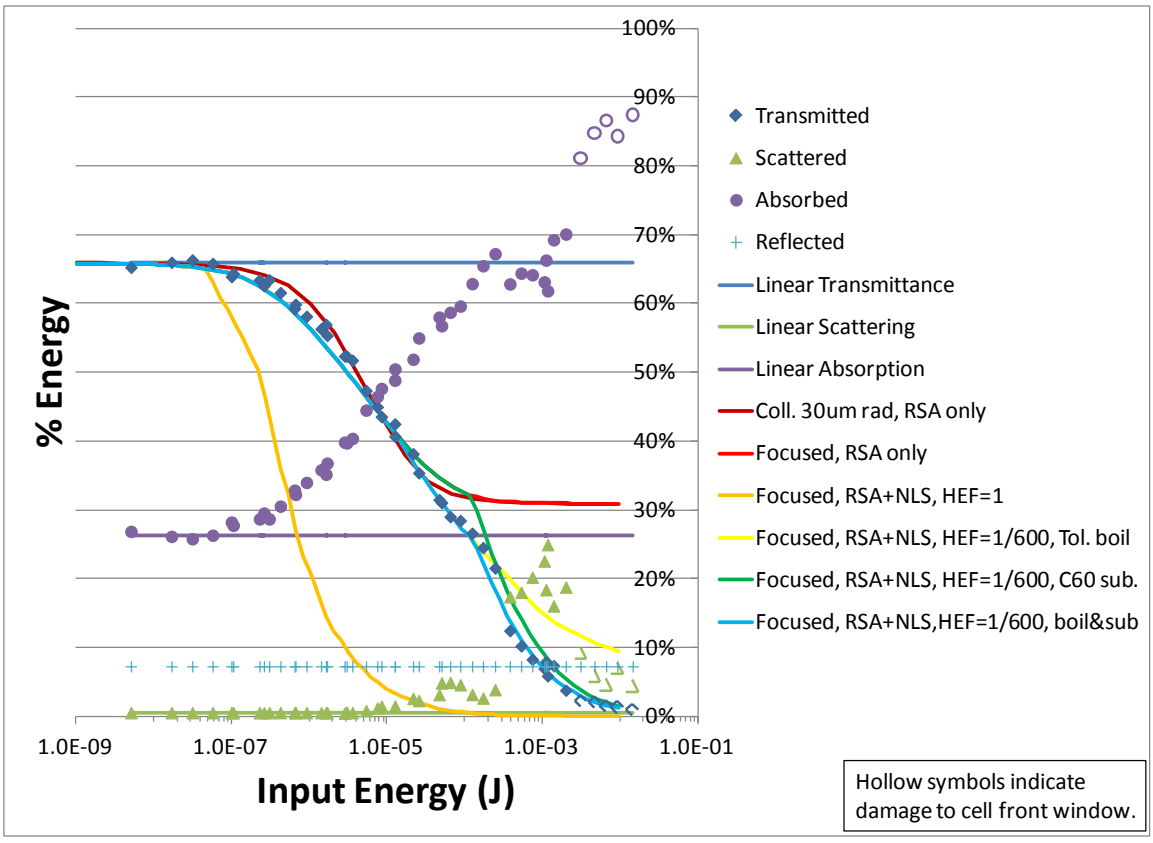

Figure 7-11. Modeling Results for C_{60} in Toluene.

Figure 7-12 shows the modeling output for C_{60}-1. The rates determined by the transient absorption spectroscopy experiments were used. The absorption cross-sections for C_{60} were used and the number of molecules was calculated from the volume of a 69 nm diameter particle, assuming face-centered-cubic (FCC) packing, the most common structure for colloidal C_{60}. All molecules were assumed to be participating in absorption. By modeling only the RSA component of the response and comparing this with the experimental data, it is obvious that particle vaporization occurs before the RSA mechanism can contribute significantly. With no compensation factor for heat dissipation, the shape of the curve is matched very well, with the activation threshold being only slightly lower than observed. With a compensation factor of only 1/2.5, the model matches the experimental data almost perfectly. A first impression upon examination of the C_{60}-1 experimental data is that this looks qualitatively very much like the CBS-1 curve. This is not unexpected, because the transient absorption spectroscopy results indicated that quenching in this colloid suspension is very high, resulting in a low triplet quantum yield, and the model indicates that sublimation occurs before there is any significant population of the triplet state. For comparison, a carbon black suspension of the same particle size (69nm diameter) was modeled, using all of the material parameters for carbon black. With a thermal compensation factor of 1/5, the CBS model results are nearly identical to the C_{60}-1 model and the observed behavior, with the exception of the very highest input energies, where the C_{60}-1 transmittance is slightly lower than the equivalent CBS particle. This is interesting, since the exact same high-energy extinction coefficient was modeled in both cases. One possible explanation for this behavior is that

C_{60}'s sublimation temperature is significantly lower than that of carbon black, which may allow more of the layers farther from focus in the focal cone to vaporize and participate in nonlinear scattering in C_{60}-1 than in the equivalent CBS suspension. However, a more likely explanation, considering the upward trend in the nonlinear absorption experimental data, is at these higher energies, the irradiance is high enough in the leading edge of the pulse to promote a significant portion of the electron population to the triplet state to enhance absorption before sublimation occurs.

Some authors have attributed the presence of an absorption peak near 350 nm in the UV-Vis spectrum of C_{60} colloids to monomeric C_{60} existing in some of the micelles.[94, 96] Therefore, modeling was done of a two-component system. Since the triplet quantum yield measured in the transient absorption spectroscopy experiments was about 4% for C_{60}-1, 4% of the total number of C_{60} molecules were modeled with the same parameters used above to model the solution of C_{60}, while the remaining 96% of the total number of C_{60} molecules were assumed to exist in 69 nm diameter particles with the triplet quantum yield of zero—essentially a carbon black suspension—but using the material parameters (e.g., complex refractive index, density, etc.) of C_{60}. The resulting transmittances of these two subcomponents were multiplied together and are shown in dark blue on the plot below. The transmittance of the monomeric C_{60} alone is shown as the dotted line. There is negligible attenuation due to the low concentration of monomeric C_{60} until the monomers sublime. Either interpretation, whether particles in which all molecules participate in RSA but with significant quenching to the first excited singlet band or a subpopulation of monomeric C_{60} acting as strong RSA absorbers and a

subpopulation of particles with essentially no RSA behavior, could be seen to fit this data set.

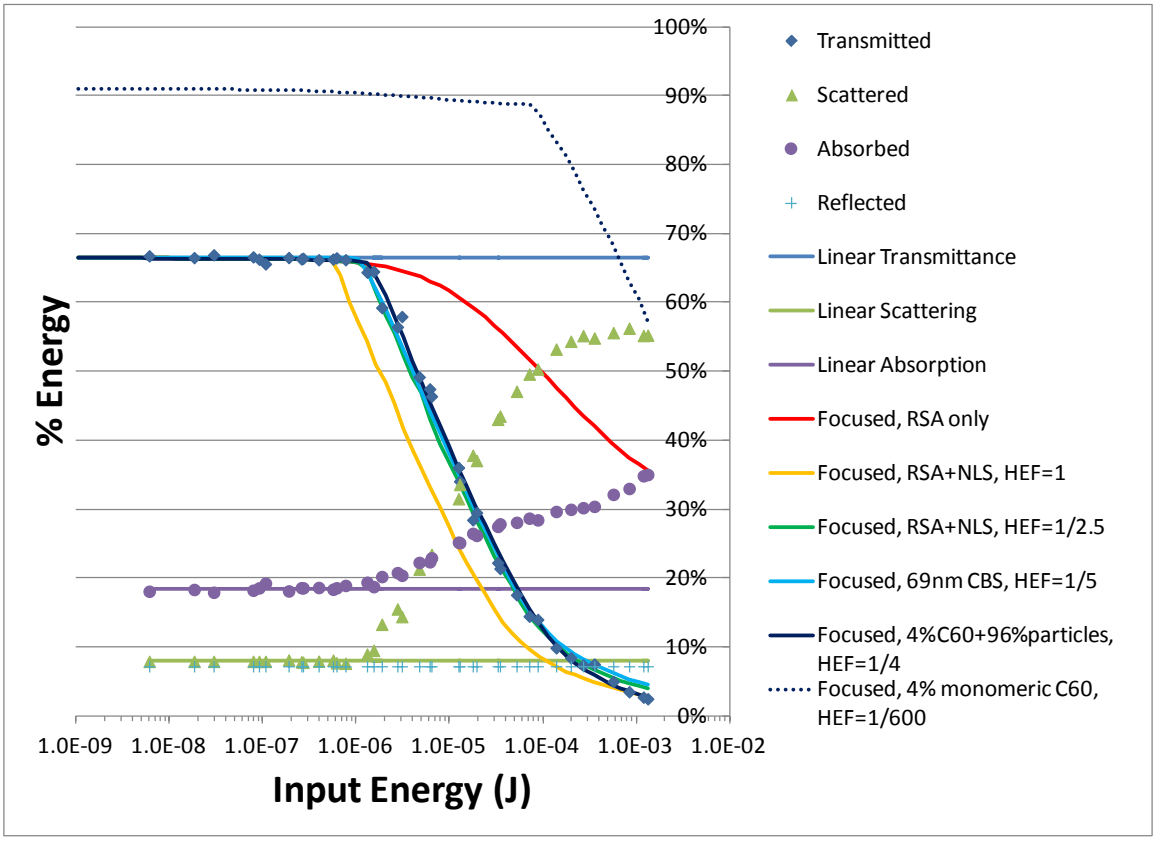

Figure 7-12. Modeling Results for C_{60}-1.

Figure 7-13 shows the modeling output for C_{60}-2. Since transient absorption spectroscopy results were not available for this sample, the hybrid RSA and nonlinear scattering model was first run using the rates for C_{60}-1. A heating efficiency factor of 1/7 was used to fit the model to the data. The data at the onset of nonlinear action obviously has a roll to it that is characteristic of RSA behavior, which falls under the knee predicted by the model assuming a 4% triplet quantum yield. The decay rate of the first excited singlet band in the model was manipulated until the shape fit the experimental data. The

best fit was at a triplet quantum yield of about 11%. Using these parameters, the hybrid RSA and nonlinear scattering model fit the data quite well, assuming a heating efficiency factor of 1/12.

The need to apply a different correction factor when the only parameter that has changed is the triplet quantum yield seems to indicate that the greater the population in the first excited triplet band, the less efficiently the colloid is heated. This is plausible since the lifetime of the first excited triplet band is on the order of about a microsecond—much longer than the duration of the laser pulse. Much of the absorbed energy that would otherwise convert to heat remains stored as electronic energy. There may be other competing processes such as triplet phosphorescence that would "rob" electrons that would otherwise thermalize. Note also that in Figure 6-11, the data for C_{60}-2 lies to the right of the data for C_{60}-1, indicating that for the same linear transmittance it takes more input energy to bring C_{60}-2 to the sublimation threshold than C_{60}-1. So, for the same amount of input energy, C_{60}-2 is not getting as hot as C_{60}-1. Since the particle size distributions are so close to each other, the most likely explanation is the difference in triplet quantum yield resulting in less efficient heating for C_{60}-2.

This sample was also modeled as a two-component system: 11% of the C_{60} molecules existing as monomeric C_{60} with near unity triplet quantum yield and 89% of the C_{60} molecules existing as particles with zero triplet quantum yield. In this case, there is a noticeable roll to the transmission curve before sublimation is reached. The sublimation of monomeric C_{60} near 100 μJ may explain the points that fall lower than the modeled curve at the highest input energies. However, CBS-1, C_{60}-1, C_{60}-2, and C_{60}-3 all

show some points at the highest input energies with transmittances below the line predicted for a constant extinction coefficient. A more likely explanation for these high-energy points is that some weak coupling of the laser pulse to the scattering centers may exist, allowing a small portion of the energy yet to be deposited after sublimation to contribute to growing the scattering centers. The data below the sublimation threshold has a better fit to the model that assumes that all of the C_{60} molecules exist in colloidal particles that are quenched to a lower triplet quantum yield. Still, neither interpretation can be completely refuted.

These results confirm the finding in the z-scan experiment that the C_{60}-2 sample had stronger RSA behavior than C_{60}-1. Also, C_{60}-2 had a much stronger absorption peak near 350 nm in the UV-Vis spectrum than did C_{60}-1. If this feature is indeed indicative of monomeric C_{60}, then the latter set of modeling results would agree with this view.

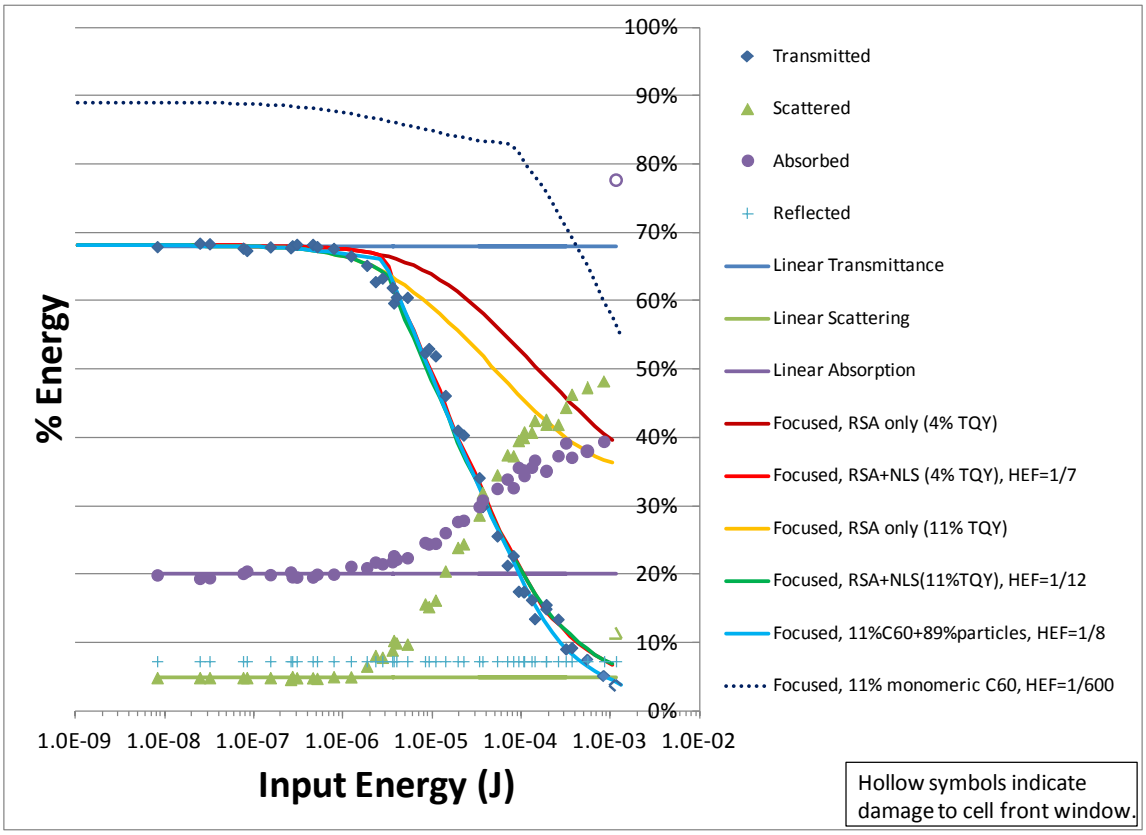

Figure 7-13. Modeling Results for C_{60}-2.

Figure 7-14 shows the modeling results for C_{60}-3. For reference, the RSA curve for pure C_{60} is shown. This data has a pronounced RSA band which, coincidently, fits best assuming an 11% triplet quantum yield. The hybrid RSA and nonlinear scattering model fits the data well, assuming a heating efficiency factor of 1/300. The average particle diameter in this sample is 6 nm. In a particle this small, all of the molecules are close to the surface boundary, less thermally isolated and therefore able to dissipate heat to the medium more quickly than in much larger particles, where most of the molecules are deep in the particle and more thermally isolated. This may explain why such a significant correction factor is necessary. In addition, there is significant population in

the triplet state, which seems to contribute less to heating. One aspect in which the model does not fit the data well is that the sublimation threshold chosen to best fit the inflection in the experimental transmittance curve does not correspond to the onset of nonlinear scattering. The model was rerun with the compensation factor of 1/60 so that the sublimation threshold would correspond to the onset of nonlinear scattering, but in this case, the remainder of the transmittance curve did not fit the typical NLS behavior of following a constant extinction coefficient. This might be attributable to a two-stage process of water vaporization followed by particle sublimation. The general behavior, though, is consistent with a colloidal particle in which all of the C_{60} molecules are contributing to reverse saturable absorption, but with significant quenching of the singlet band, which becomes a strong scattering center upon sublimation. The UV-Vis spectrum of this sample was notably different than that of the other colloids, with almost no feature at 350 nm. Therefore, it is unlikely that any significant portion of this sample is in monomeric form.

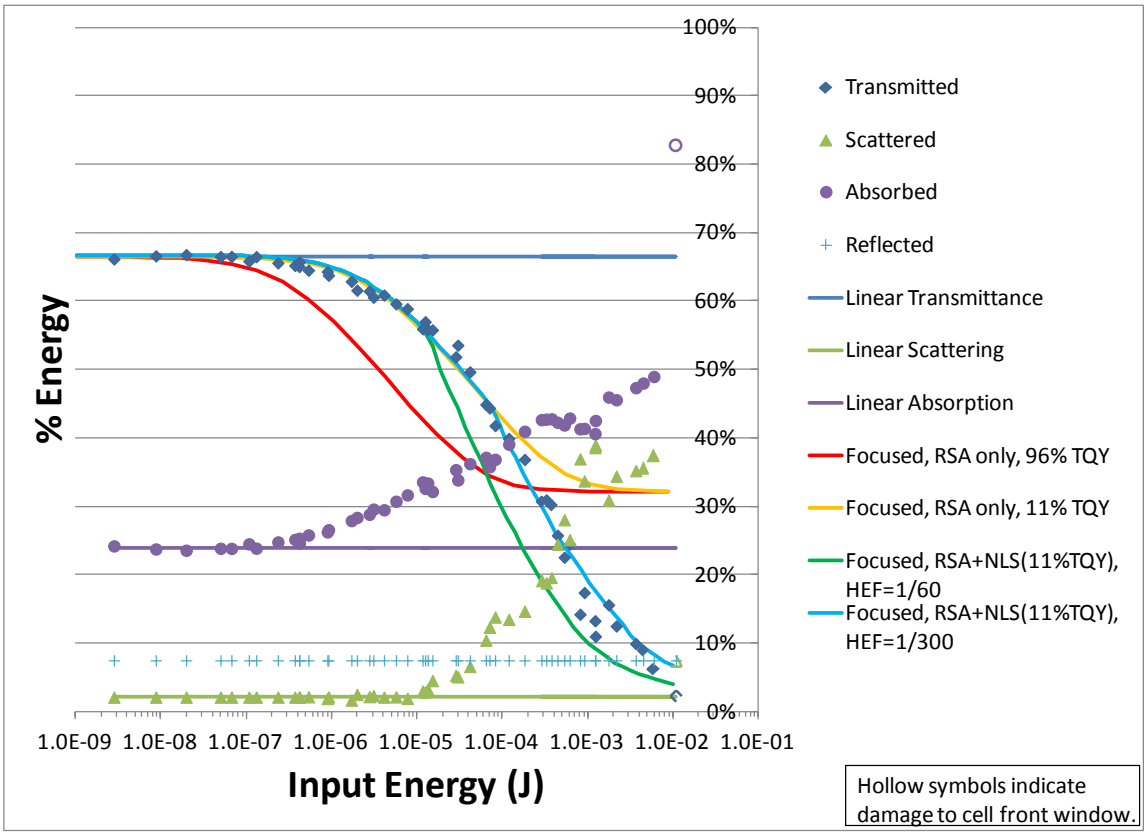

Figure 7-14. Modeling Results for C_{60}-3.

Egerev discuss the dissipation of heat to the medium as a function of particle size. The particle sizes for which heat exchange with the surroundings is negligible are on the order of $R_{np}^2 >> (\chi_l \tau_L)$.[138] In the case where the solvent is water and the pulse length is 10 ns, $\chi_l \tau_L$ is 1.4 x 10^{-15} m^2, and the corresponding particle radius is 37.4 nm. For particles much larger than this, the energy (or fluence) required to reach the vaporization or sublimation threshold should be proportional to R_{np}. All of the samples in this investigation except for CBS-2 have particle radii less than this, so all of the samples can be expected to require some correction for heat dissipation. CBS-2 requires a correction factor because it is really too large to be treated as a volumetric absorber. For particle

radii much smaller than 37.4 nm, the energy (or fluence) required to reach the vaporization or sublimation threshold should be proportional to $1/R_{np}$. However, most of the particle sizes are near the middle of this range, so no clear trend in HEF correction factors was observed. The relationship between HEF factors may have been further complicated by the apparent trend indicating that the triplet population is less efficient at heating than the singlet population. To truly understand the underlying thermodynamics, a model should be developed with full thermodynamic differential equation solving.

7.8. Conclusions

Modeling collimated vs. focused cases highlighted the fact that the shape of the input energy vs. transmittance curve is a strong function of the geometry of the focal region.

Using the McEwan approach of modeling a particle suspension with a digital response, assuming a single low-energy extinction coefficient in the linear region and a single high-energy extinction coefficient in the nonlinear scattering region, reproduces the shape of the input energy vs. transmittance curve well for all samples in the NLS regime. This indicates that, to first order, the scattering centers formed are of a characteristic size and independent of the input energy. From this, it follows that when these scattering centers form, the remainder of the energy in the input pulse yet to be deposited does not cause the scattering center to grow significantly further.

The model based on estimating the initial bubble size from the relationship suggested by Egerev does not agree with the experimental data. This is because of the

inherent assumption that all of the energy in the pulse goes into creating the vapor bubble.

A “heating efficiency factor” (HEF) was required to fit the models to the observed sublimation thresholds. This was necessary because of the simplified assumption of thermally isolated particles. Although there is a trend that smaller particles need a smaller HEF to fit the data (as a result of being less thermally isolated than larger particles), a clear relationship between HEF and particle size was not obtained, because size was not the only factor that seemed to affect the efficiency of heating the particles to sublimation. Samples with higher triplet quantum yields also seemed to be less efficient at heating to sublimation than particles with strong singlet quenching. This is at least partially justified by the fact that some of the absorbed energy remains stored as electronic energy in the triplet state until long after the pulse and thus cannot contribute to heating.

The model of nonlinear scattering due to particles heating to sublimation fit the experimental data for CBS-1 and CBS-2 with appropriate choices for HEF and high-energy extinction coefficient.

The experimental data for C_{60} in toluene fit the RSA-only model very well in the RSA portion of its response. A very low HEF was required to fit the observed thresholds for the onset of nonlinear scattering in this sample. This sample had the smallest “particle” size (an individual molecule) and was therefore the least thermally isolated of the samples. It was also the strongest triplet former. Both of these would trend toward a low HEF.

The separation in the input energy thresholds for the onsets of the two regions of NLS in C_{60} in toluene corresponds approximately to the difference between the boiling point of toluene and the sublimation point of C_{60}. So, these two mechanisms could explain the source of the scattering in each NLS region.

Modeling confirms that sublimation occurs before any significant population of the triplet state in C_{60}-1.

C_{60}-2 has a short region of RSA behavior prior to sublimation, which fits best assuming a triplet quantum yield of 11%.

A lower HEF is required to fit the C_{60}-2 data than C_{60}-1. Since the particle size distributions of these two samples are so similar, this lower heating efficiency is likely correlated with a higher triplet population.

C_{60}-3 has a significant region of RSA prior to sublimation, which fits best assuming a triplet quantum yield of 11%.

Since the best-fit triplet quantum yield of C_{60}-2 and C_{60}-3 is so similar and their average particle sizes are so different, it is likely that the singlet quenching processes are more a function of morphology than of particle size. Both C_{60}-2 and C_{60}-3 appear amorphous via TEM observation. It may be that this amorphous packing results in significant quenching upon the association of even a small number of molecules. As seen in the C_{60}-1 sample, tighter packing into crystalline symmetry results in even stronger singlet quenching.

The higher onset of NLS behavior in C_{60}-3 than C_{60}-2 is most directly related to the smaller particle size of C_{60}-3 and its lower degree of thermal isolation. Since it loses

heat more quickly to its environment, it takes more input energy to raise it to its sublimation temperature.

The shapes of the input energy vs. transmittance curves are more consistent with a view that all C_{60} molecules in the agglomerates are participating in reverse saturable absorption, but with singlet quenching due to molecular proximity, than with a view that the observed RSA is due solely to molecular C_{60} in monomeric micelles with no RSA contribution from the agglomerates. There may very well be monomeric C_{60} micelles present in the C_{60}-1 and C_{60}-2 suspensions, but if so, these are not the only C_{60} molecules that participate in RSA.

7.9. Future Improvements to the Model

As emphasized above, the model is very simple and there is much room to build upon it. One of the chief improvements would be to include a thermodynamic treatment with full differential equation solving, which would hopefully reduce or eliminate the need for any thermal fitting parameter. The model could be improved to include heat transfer from the particle to the fluid and track both liquid vaporization and carbon sublimation temperature. A better understanding is needed of the efficiencies of heat generation in each of the states associated with the RSA process. An efficiency parameter could possibly be assigned to each of these processes as a result of laboratory measurements. For example, one would expect the portion of the light absorbed from the ground state that undergoes ISC to the triplet state to have almost no contribution to heating. One would expect that the absorption from the first excited singlet and triplet states would be fairly efficient at heating, since relaxation from these processes is

primarily due to intramolecular vibrational relaxation. Fluorescence and phosphorescence are other processes by which excited states relax without generating heat, which could also be accounted for in the model. The model could be expanded to include a radial dependence of the irradiance rather than a simple uniform disk. The model could be expanded to include another spatial coordinate to allow modeling of non-rotationally symmetric irradiance profiles. The model could be modified to include full beam propagation and refractive effects. The general approach of estimating a scattering center size based on the energy absorbed up to the sublimation point and calculating the resulting absorption and scattering cross sections via Mie theory would be a viable and valuable addition, so long as the energy in the pulse after sublimation is not assumed to contribute to the scattering center size. The growth dynamics of the scattering center beyond its initial size could also be modeled, since some growth is known to occur on the timescales of the pulse and could account for the slight divergence seen from the constant extinction coefficient assumption seen for the very highest data points. For higher accuracy and application to all time regimes, it could be modified to include a full treatment of the system of differential equations for reverse saturable absorption rather than the analytical solutions described above.

CHAPTER 8: SUMMARY

The goal of this dissertation was to examine the photophysics of colloidal C_{60} suspensions to determine if they might offer a nonlinear optical response that was in some way improved over benchmark NLO materials such as carbon black suspensions and molecular solutions of C_{60}. C_{60} molecules are known to be very efficient reverse saturable absorbers and it was posited that particles composed of C_{60} molecules might reasonably be expected to retain at least some RSA behavior as agglomerates. Carbon black suspensions are known to have strong nonlinear scattering behavior, driven by strong linear absorption. Colloidal C_{60} particles are very similar to carbon black particles when they are of similar size, so it was posited that C_{60} colloids would also show a nonlinear scattering behavior when heated to sublimation. The hope at the outset of this investigation was that the interaction of the processes of nonlinear absorption and nonlinear scattering would result in a material that was more strongly attenuating than either C_{60} or CBS on their own—either by RSA providing extra absorbed energy to make the NLS effect stronger or by simply attenuating more via NLA than the equivalent linear absorber would.

Several samples of colloidal C_{60} suspensions were obtained and characterized in comparison to two carbon black suspensions and a solution of C_{60} in toluene as benchmark materials.

Examination of the colloidal C_{60} samples via transmission electron microscopy revealed broad size distributions with small particles on the order of 5 nm diameter as

well as larger agglomerates in all three samples. The large agglomerates in the C_{60}-1 sample had notably strong crystalline packing of either FCC or hexagonal close-packed structure, as evidenced via Fourier transforms of the lattice fringes in high resolution TEM images. The very small particles as well as the agglomerates in the C_{60}-2 and C_{60}-3 samples lacked crystalline character.

The particle size distributions of the colloidal C_{60} and CBS samples were characterized via dynamic light scattering and nanoparticle tracking analysis. The DLS results indicated that all of the samples had broad size distributions. CBS-1 had an average particle diameter (on a number density basis) of around 35 nm. CBS-2 was a very poor sample with a bimodal size distribution with the center of the two modes being about 100 nm and 1600 nm (on a number density basis) in diameter. There was also some spurious evidence for some very small particles near 1 nm in this sample. C_{60}-1 and C_{60}-2 had very similar particle size distributions with the average diameter being in the 60-70 nm range (on a number density basis). C_{60}-3 showed an average particle diameter of near 6 nm, with a small amount of larger contaminant particles near 200nm in diameter. The NTA instrument has difficulty with particle sizes below 50 nm and above 1 μm. It agreed very well with the DLS data for C_{60}-1 and C_{60}-2, but the results by this technique for CBS-1, CBS-2, and C_{60}-3 were questionable.

UV-Vis ground state absorption spectra confirmed the characteristic absorption spectrum for C_{60} in toluene that is well known in the literature: a pronounced absorption feature near 350 nm, a small, sharp absorption feature near 410 nm, and a broad absorption band in the 500-600 nm region with a distinctive feature near 600nm. The

spectra for C_{60}-1 and C_{60}-2 both had the characteristic C_{60} feature near 350 nm—although much subdued compared to the pure C_{60} solution. They also had a distinct bump near 450 nm which is recognized in the literature as evidence for the formation of C_{60} colloids. Some authors view the presence of the peaks near 350 nm in these samples as evidence for the existence of molecular C_{60} in monomeric micelles. The C_{60}-3 sample had an almost featureless absorption spectrum that rose sharply as it approached the ultraviolet, with a hint of a feature near 350 nm. Although it lacked the characteristic bump near 450 nm, it was a very good match for a spectrum reported in the literature for a sample that is completely in the colloidal state. The UV-Vis spectra for CBS-1 and CBS-2 followed a gradual roll that is typical for absorbing particle suspensions.

C_{60}-1 was thoroughly characterized via both femtosecond pump-probe spectroscopy and nanosecond laser flash photolysis, with rates for the processes involved in the 5-level RSA model being determined. C_{60}-2 and C_{60}-3 were briefly characterized by nanosecond laser flash photolysis. The results here showed that the first excited singlet state in C_{60}-1 was very strongly quenched, leading to very inefficient inter-system crossing to the triplet manifold, with an estimated triplet quantum yield of only 4.4%, compared to the 96% yield of molecular C_{60} solutions. The absorption spectrum of the first excited singlet state in C_{60}-1 was notably different than that of C_{60} in toluene. Flash photolysis showed that the absorption spectrum of the first excited triplet state was very similar in all three C_{60} colloid samples to that of molecular C_{60} solutions. Therefore, all three colloidal samples would be expected to exhibit some RSA behavior if the triplet state were to become sufficiently populated.

Z-scans were conducted on the C_{60}-1 and C_{60}-2 samples, with CBS-1 and C_{60} in toluene also run as benchmark references. As expected, C_{60} in toluene showed strong nonlinear absorption with an average triplet-triplet absorption cross-section obtained by simplified 3-level analysis of the results that was in keeping with the values reported in the literature (7.5×10^{18} cm^2). CBS-1 showed a z-scan pattern that is typical of nonlinear scattering and did not submit itself to 3-level RSA analysis. The C_{60}-1 sample showed a z-scan pattern that was similar to CBS-1 and did not submit itself to RSA analysis. The C_{60}-2 sample did show a z-scan with characteristic RSA behavior, yielding triplet-triplet excited state absorption cross-sections of 2.71×10^{-19} cm^2 and 3.15×10^{-19} cm^2 at input energies of 12.8 μJ and 18.7 μJ, respectively. The z-scan result for C_{60}-1 is consistent with the transient absorption spectroscopy results, predicting very weak RSA behavior from this sample. The z-scan result for C_{60}-2 indicates that this sample has stronger RSA behavior than C_{60}-1. This correlates with the stronger peak at 350 nm in the C_{60}-2 ground state absorption spectrum and with the fact that it has a more amorphous character than C_{60}-1 via TEM.

All six samples were studied in an experiment that simultaneously measured, as a function of input energy, the percent of energy transmitted, scattered, and absorbed by the sample.

The CBS-1 sample showed a sharp activation threshold followed by a sharp decrease in transmittance that was a result of both nonlinear scattering and nonlinear absorption, but dominated by nonlinear scattering. This is consistent with a model that assumes that the light absorbed by the particle results in heating of the particle to the

sublimation temperature and the explosive formation of scattering centers. The presence of nonlinear absorption could indicate the presence of absorbing plasmas in the scattering centers.

The experimental data only fits the model if a constant high-energy extinction coefficient is assumed. This implies that the scattering centers have a characteristic size that is independent of the input energy. This indicates that energy is strongly coupled into the particles up to the point of sublimation, but once the scattering centers form, the remainder of the input energy does not have a mechanism with which to increase their size. This trend was found in all samples beyond the onset of nonlinear scattering behavior.

The CBS-2 sample showed a much higher threshold for the onset of nonlinear scattering and the transmittance fell off much more gradually, fitting to a much lower NLS extinction coefficient. The higher activation threshold is explained by the significant population of micron-sized agglomerates, which absorb most of the light due to their higher absorption cross-section than the 100 nm particle population. The rate of heating is inversely proportional to the cube of the particle radius, so it takes more input energy to raise a large particle to the sublimation threshold. The lower attenuation is likely due to the sparsity of the micron-sized particles. Unlike CBS-1, CBS-2 showed no evidence of nonlinear absorption whatsoever.

The C_{60} in toluene sample is dominated by strong reverse saturable absorption, followed by two distinct regions of nonlinear scattering. The reverse saturable absorption matches established RSA theory very well. The two regions of nonlinear scattering may

be due to the formation of vapor bubbles at the boiling point of toluene and the sublimation of C_{60} molecules.

C_{60}-1 performed essentially like a carbon black suspension. It had a sharp onset of nonlinear behavior that consisted of both nonlinear absorption and nonlinear scattering, but was dominated by nonlinear scattering. This is consistent with its low triplet quantum yield as determined by transient absorption spectroscopy and with its lackluster z-scan performance.

C_{60}-2 had a short region of RSA-dominated attenuation followed by a NLS-dominated mechanism. Fitting of the curve to a numerical model in the RSA region yielded an estimated triplet quantum yield of 11%. The fact that C_{60}-2 has a stronger RSA performance than C_{60}-1 is consistent with the z-scan results and correlated to the higher peak at 350 nm in the ground state spectrum and to a particle morphology that is more amorphous than C_{60}-1. C_{60}-2 exhibits a higher sublimation energy threshold than C_{60}-1. Since their particle size distributions are so similar, this is likely not explained by differences in thermal dissipation due to differences in particle size. Rather, it is more likely due to the higher population of triplet states in C_{60}-2. Much of the absorbed energy that would otherwise go into heat generation is stored as electronic energy in the triplet state until long after the laser pulse. There may also be other decay processes associated with the triplet state such as phosphorescence which do not result in heat generation. The result of the higher sublimation threshold is that at each input energy, the transmittance of C_{60}-2 is slightly higher than C_{60}-1. So, it appears that the stronger RSA behavior of C_{60}-2 actually makes it a slightly worse attenuator than C_{60}-1 overall.

C_{60}-3 exhibited an extended region in which RSA alone dominated its NLO response. Fitting of this part of the data to a numerical model yielded an estimated triplet quantum yield of 11%. The fact that the triplet quantum yields of C_{60}-2 and C_{60}-3 are so similar but their average particle diameters are so different (62 nm and 6 nm, respectively) argues against the triplet quantum yield being a function of particle size. Rather, it is more likely a function of morphology. C_{60}-2 and C_{60}-3 both appeared rather amorphous in the TEM images, whereas C_{60}-1 (which had a lower triplet quantum yield) was extremely crystalline. This indicates that significant quenching occurs when C_{60} molecules come together to form particles at even small particle sizes. But, when the packing is denser—as in crystalline structures—the closer proximity of molecules leads to more efficient quenching of the first singlet excited state.

At higher energies, C_{60}-3 also undergoes a phase change to form scattering centers when the particles heat to the sublimation temperature. As with all the other samples, this scattering behavior is best fit by assuming a constant extinction coefficient in the NLS region. The onset of NLS is at a higher energy in C_{60}-3 than in C_{60}-2. This is because the C_{60}-3 particles are so much smaller and, thus, less thermally isolated from the medium. They dissipate heat more readily, so it takes a higher input energy for them to be heated to sublimation.

When the data were compared to numerical models, a “heating efficiency factor” needed to be included as a fitting parameter in order to match the observed sublimation thresholds. Although an exact relationship was not found for this fitting parameter, two general trends were observed. First, lower heating efficiency factors were required for

smaller particles. Second, lower heating efficiency factors were required for samples with higher triplet quantum yields. This is interpreted as smaller particles being farther from the models' assumption of thermal isolation; the smaller the particles, the more heat they dissipate to their surroundings, so the smaller the HEF required so that the model would not raise the particles' temperature too quickly. Also, samples with a higher triplet quantum yield seem to heat up less efficiently than strongly quenched or linearly absorbing particles, so a smaller HEF is required to compensate for the energy not converted to heat due to being stored as electronic energy or lost to other non-thermal decay processes.

The sample in this study that provided the most overall attenuation was C_{60}-1. This indicates that C_{60} colloids do present a marginal advantage over the benchmark materials of carbon black suspensions and molecular C_{60}, but not for the reasons originally contemplated. Although molecular solutions of C_{60} are by far the best performers at very low input energies, their change in transmittance with input energy is much more gradual than that of the particle suspensions. Compared to carbon black suspensions, C_{60} colloids have a lower sublimation temperature and therefore their sublimation threshold occurs for a lower input energy. While C_{60} colloids do exhibit some RSA behavior and one might intuitively think that this would make them more efficient attenuators of light, the data in this study would indicate that the higher the triplet quantum yield, the slower the particles will heat, thus raising their threshold for the onset of nonlinear scattering. This interpretation would seem to indicate that the optimum design of a C_{60} colloid for maximum attenuation would be highly crystalline.

This would take advantage of the low sublimation threshold of C_{60}, maximize the energy converted to heat in the particle by avoiding the triplet state, and also benefit from a bit of extra absorption due to population of the triplet state at very high input energies.

In summary, this study showed that both reverse saturable absorption and nonlinear scattering contribute to the nonlinear optical response of C_{60} colloids and that C_{60} colloids can indeed have a stronger nonlinear optical response than benchmark materials such as carbon black suspensions and molecular C_{60} solutions, particularly if they are highly crystalline. However, this improvement is primarily due to the lower sublimation temperature of C_{60} compared to carbon black rather than to the influence of reverse saturable absorption. Reverse saturable absorption actually weakens the nonlinear scattering response by reducing the rate at which particles are heated by the light they absorb. (This is a lesson that can be applied to all RSA materials. The threshold for NLS will be higher in materials with higher triplet quantum yields and long-lived triplet states because the energy stored as electronic energy in the triplet state cannot contribute to raising the temperature during the pulse if the triplet lifetime exceeds the pulse length.) A highly crystalline colloid morphology results in faster quenching of the excited singlet state. This in turn results in a lower triplet quantum yield and ensures that the maximum amount of absorbed energy is converted into heat, thereby driving the nonlinear scattering process efficiently.

APPENDIX A: PARTICLE SIZE DISTRIBUTION PLOTS FROM DYNAMIC LIGHT SCATTERING AND NANOPARTICLE TRACKING ANALYSIS MEASUREMENTS

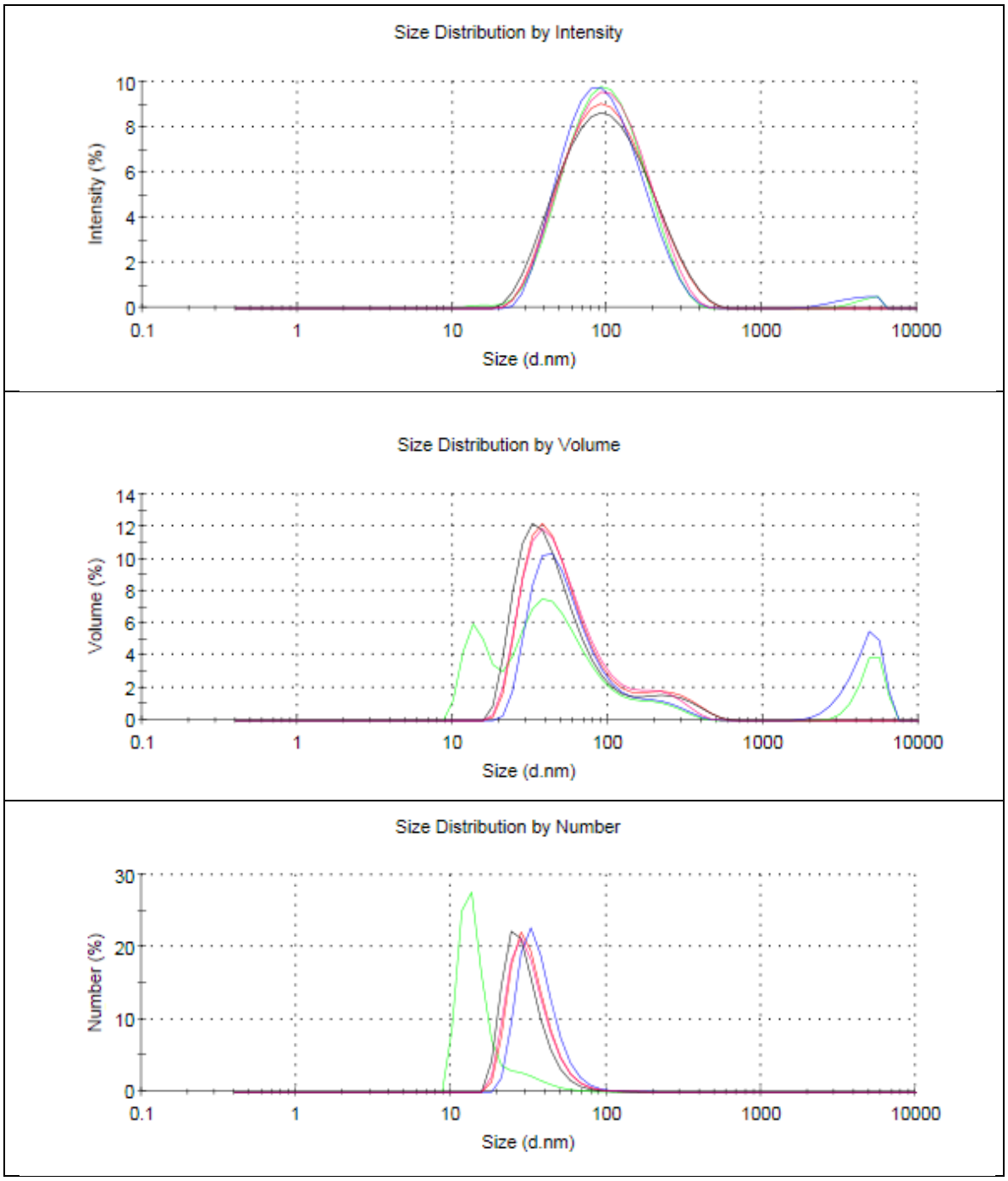

Figure A-1. DLS Size Distribution Plots for CBS-1.

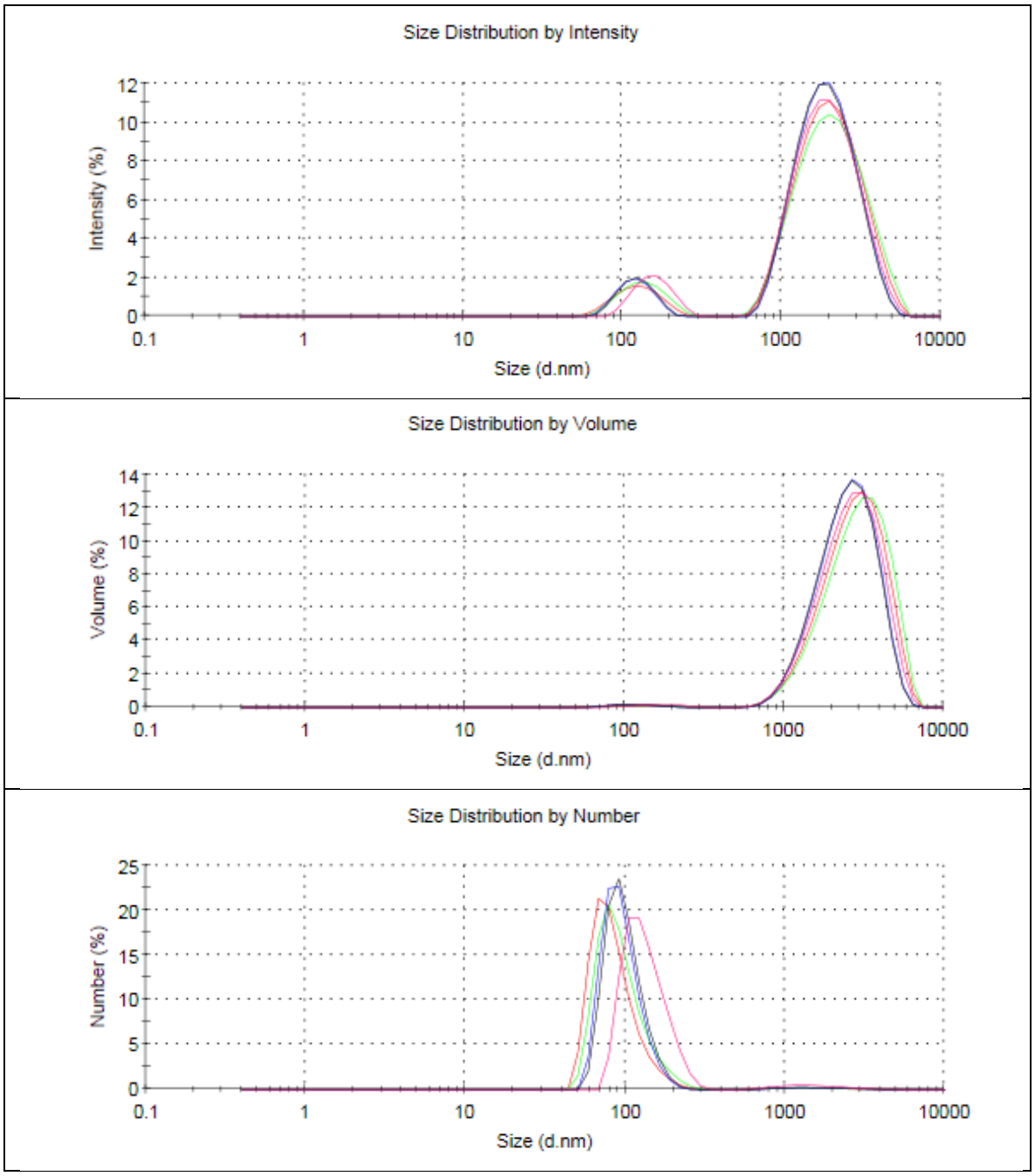

Figure A-2. DLS Size Distribution Plots for CBS-2.

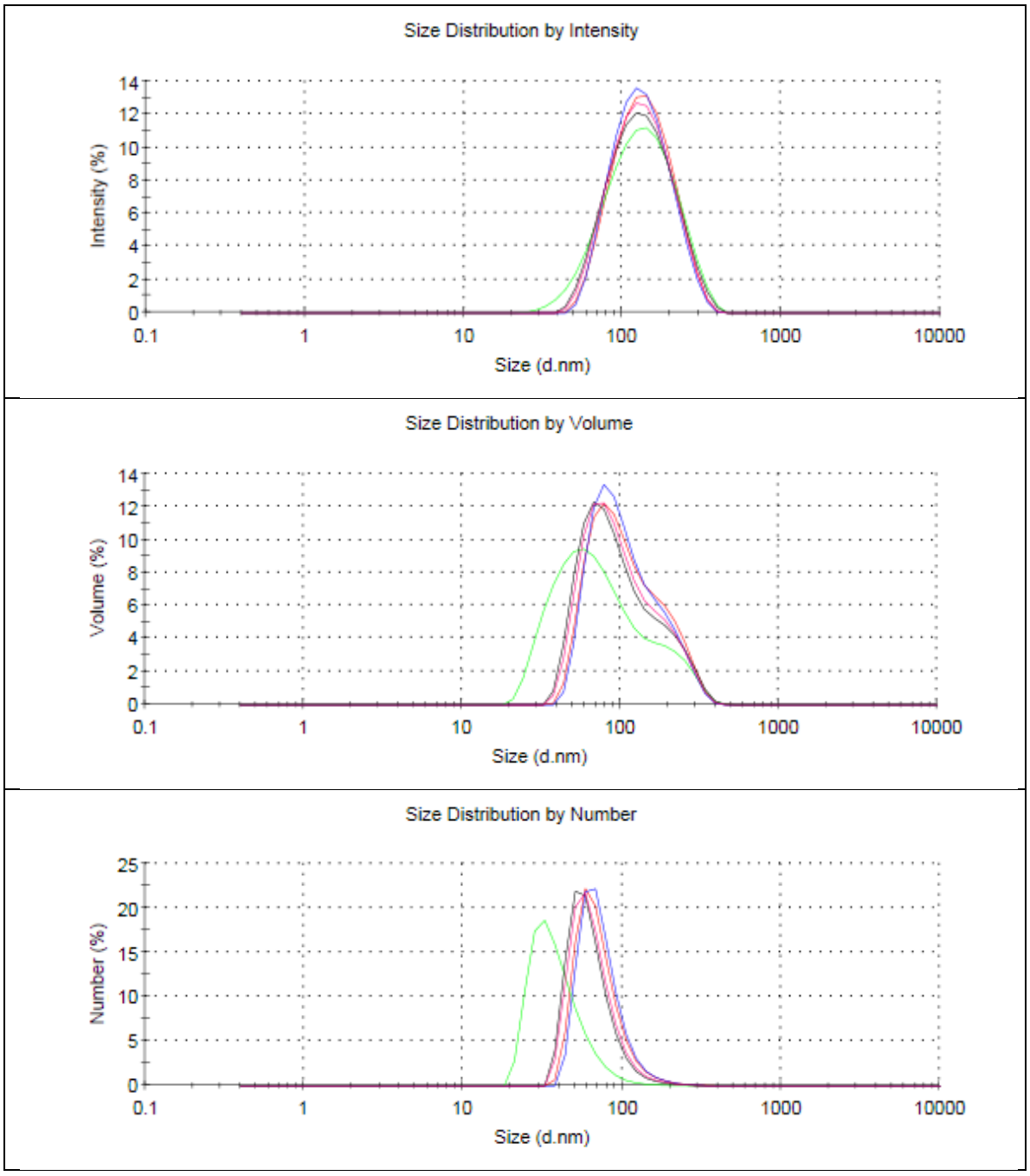

Figure A-3. DLS Size Distribution Plots for C_{60}-1.

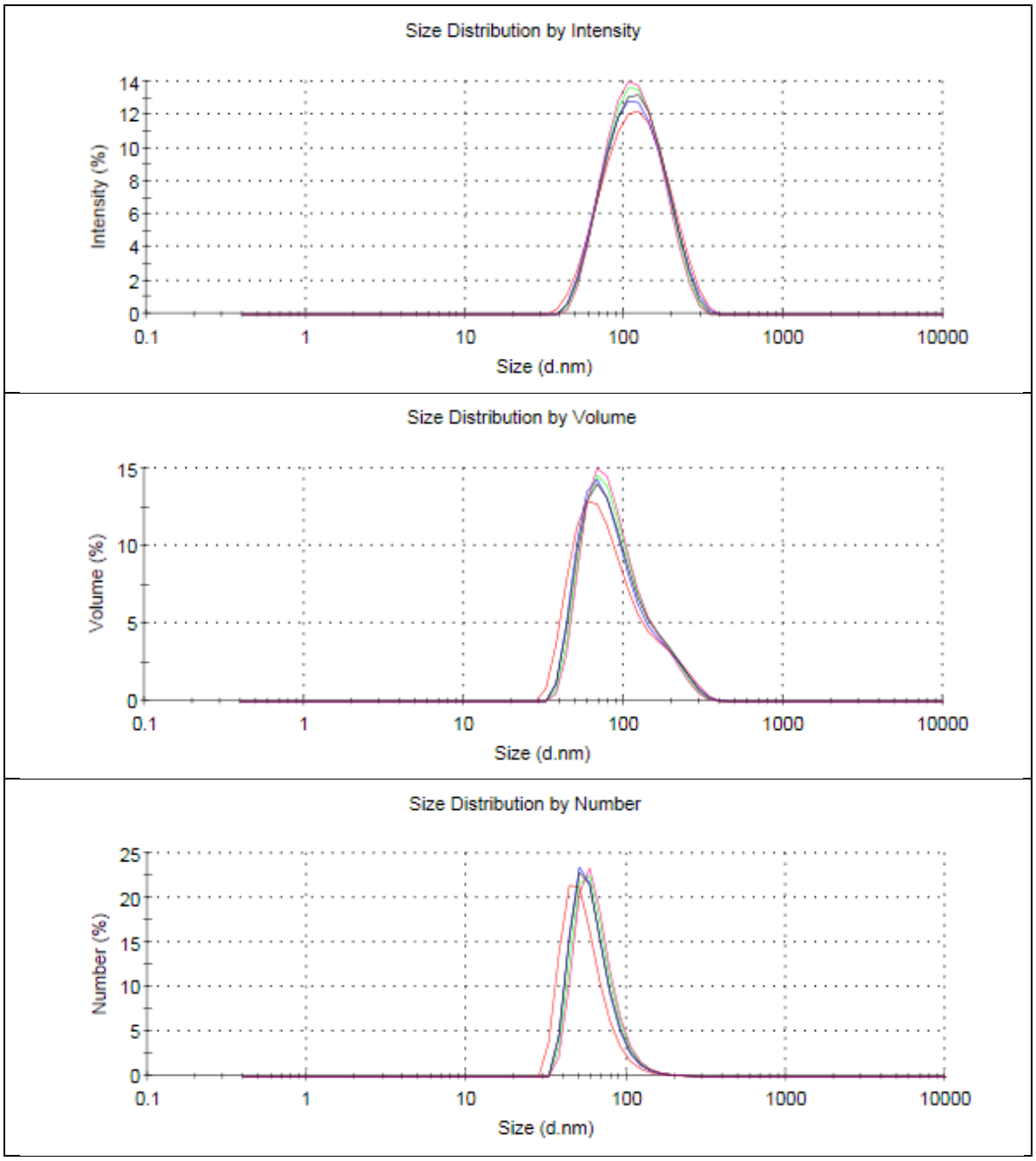

Figure A-4. DLS Size Distribution Plots for C_{60}-2.

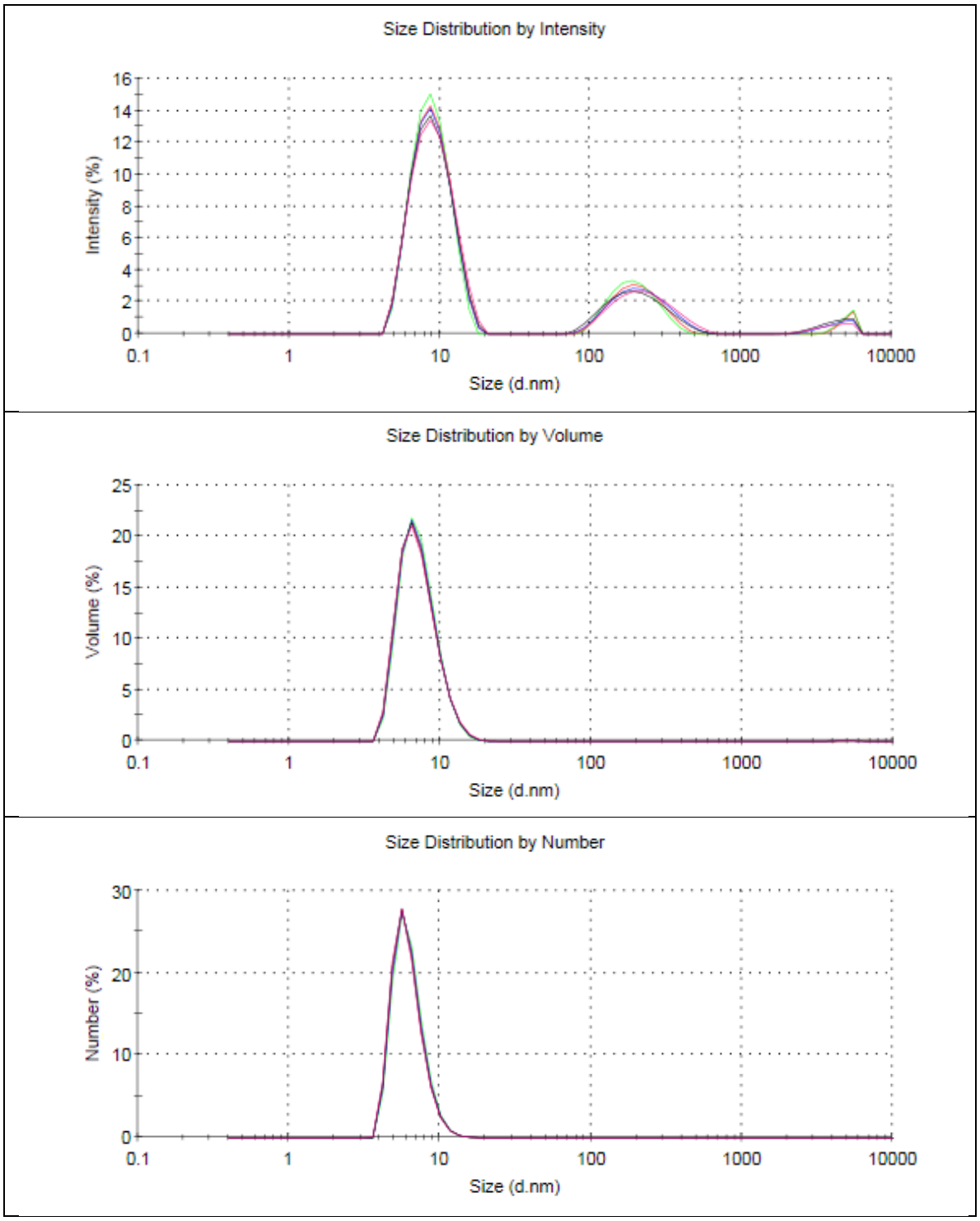

Figure A-5. DLS Size Distribution Plots for C_{60}-3.

NANOSIGHT

ANALYSIS REPORT

Nanoparticle Tracking Analysis (NTA) Version 2.3 Build 0011 RC1

Sample:	4as246a acidified carbon black
Date/Time of Capture:	16 August 2012 14:11
Video File:	4as246a_unfiltered_2500x_16aug12.avi analysis no: 003
Operator:	andy clements
Comments:	

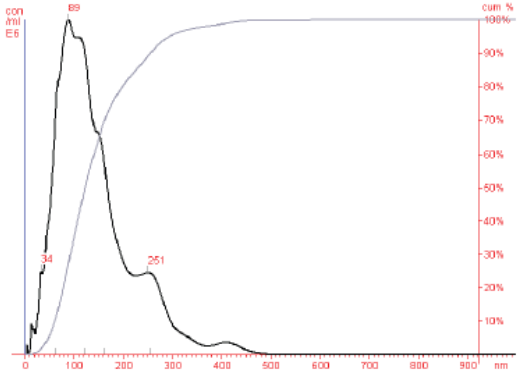

Particle Size / Concentration

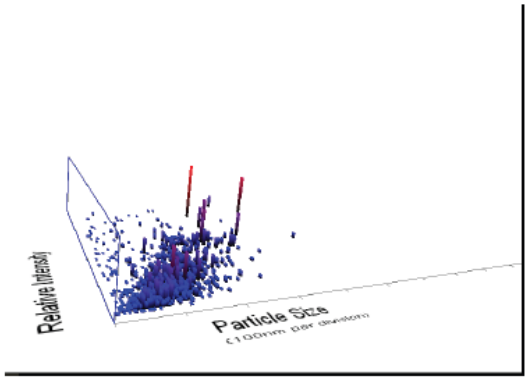

Particle Size / Relative Intensity 3D plot

Bin Centre (nm)	Concentration (E6 particles/ml)	Percentile Undersize (%)
10	0.581	0.448
30	3.029	2.784
50	7.677	8.703
70	14.796	20.111
90	18.029	34.012
110	17.431	47.452
130	14.988	59.009
150	12.161	68.386
170	9.030	75.348
190	6.144	80.085
210	4.734	83.735
230	4.380	87.112
250	4.509	90.589
270	3.936	93.623
290	2.403	95.476
310	1.413	96.565
330	1.016	97.349
350	0.678	97.872
370	0.491	98.251
390	0.575	98.694
410	0.671	99.211
430	0.536	99.624
450	0.290	99.848
470	0.125	99.944
490	0.050	99.982
510	0.018	99.996
530	0.005	99.999
550	0.001	100.000
570	0.000	100.000
590	0.000	100.000
610	0.000	100.000
630	0.000	100.000
650	0.000	100.000
670	0.000	100.000

Bin Centre (nm)	Concentration (E6 particles/ml)	Percentile Undersize (%)
690	0.000	100.000
710	0.000	100.000
730	0.000	100.000
750	0.000	100.000
770	0.000	100.000
790	0.000	100.000
810	0.000	100.000
830	0.000	100.000
850	0.000	100.000
870	0.000	100.000
890	0.000	100.000
910	0.000	100.000
930	0.000	100.000
950	0.000	100.000
970	0.000	100.000
990	0.000	100.000
1000-2000	0.000	100.000

Results

Mean:	143 nm
Mode:	89 nm
SD:	78 nm
D10:	62 nm
D50:	123 nm
D90:	256 nm
User Lines:	0 nm, 0 nm
Concentration:	1.30 E8 particles/ml
Completed Tracks:	1115

Measurement Conditions

Temperture:	23.70 °C
Viscosity:	0.92 cP
Frames Per Second:	30.00
Measurement Time:	215 of 215 s
Drift Velocity:	571 nm/s
Camera Shutter:	30 ms

Analysis Conditions

Blur:	Auto
Detection Threshold:	4 Multi
Min Track Length:	Auto
Min Expected Size:	30nm

Figure A-6. NTA Size Distribution Analysis for CBS-1.

NANOSIGHT

Nanoparticle Tracking Analysis (NTA) Version 2.3 Build 0011 RC1

ANALYSIS REPORT

Sample: 2DG103009-1
Date/Time of Capture: 16 August 2012 15:31
Video File: 2DG103009-1_unfiltered_2500x_16aug12.avi analysis no: 005
Operator: andy clements
Comments:

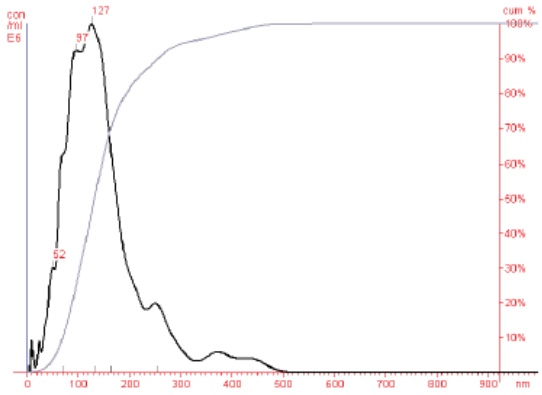

Particle Size / Concentration

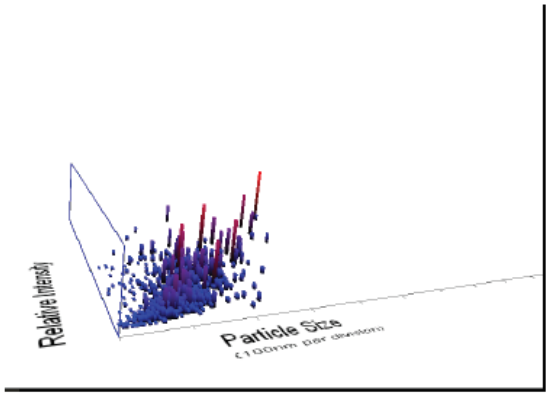

Particle Size / Relative Intensity 3D plot

Bin Centre (nm)	Concentration (E6 particles/ml)	Percentile Undersize (%)
10	0.374	0.400
30	1.194	1.678
50	3.695	5.633
70	7.990	14.184
90	11.690	26.696
110	12.742	40.332
130	13.469	54.747
150	11.739	67.311
170	7.933	75.801
190	4.912	81.058
210	3.508	84.813
230	2.615	87.612
250	2.668	90.468
270	2.150	92.769
290	1.309	94.170
310	0.753	94.976
330	0.480	95.490
350	0.610	96.143
370	0.795	96.994
390	0.711	97.754
410	0.582	98.377
430	0.573	98.990
450	0.499	99.524
470	0.298	99.843
490	0.114	99.965
510	0.028	99.995
530	0.004	100.000
550	0.000	100.000
570	0.000	100.000
590	0.000	100.000
610	0.000	100.000
630	0.000	100.000
650	0.000	100.000
670	0.000	100.000

Bin Centre (nm)	Concentration (E6 particles/ml)	Percentile Undersize (%)
690	0.000	100.000
710	0.000	100.000
730	0.000	100.000
750	0.000	100.000
770	0.000	100.000
790	0.000	100.000
810	0.000	100.000
830	0.000	100.000
850	0.000	100.000
870	0.000	100.000
890	0.000	100.000
910	0.000	100.000
930	0.000	100.000
950	0.000	100.000
970	0.000	100.000
990	0.000	100.000
1000-2000	0.000	100.000

Results

Mean:	151 nm
Mode:	127 nm
SD:	80 nm
D10:	71 nm
D50:	133 nm
D90:	256 nm
User Lines:	0 nm, 0 nm
Concentration:	0.93 E8 particles/ml
Completed Tracks:	755

Measurement Conditions

Temperture:	22.90 °C
Viscosity:	0.93 cP
Frames Per Second:	30.00
Measurement Time:	215 of 215 s
Drift Velocity:	497 nm/s
Camera Shutter:	30 ms

Analysis Conditions

Blur:	Auto
Detection Threshold:	4 Multi
Min Track Length:	Auto
Min Expected Size:	30nm

Figure A-7. NTA Size Distribution Analysis for CBS-2.

NANOSIGHT

ANALYSIS REPORT

Nanoparticle Tracking Analysis (NTA) Version 2.3 Build 0011 RC1

Sample:	EIC Aug2007 C60 Colloids
Date/Time of Capture:	17 August 2012 11:22
Video File:	aug2007_unfiltered_17aug12.avi analysis no: 002
Operator:	andy clements
Comments:	

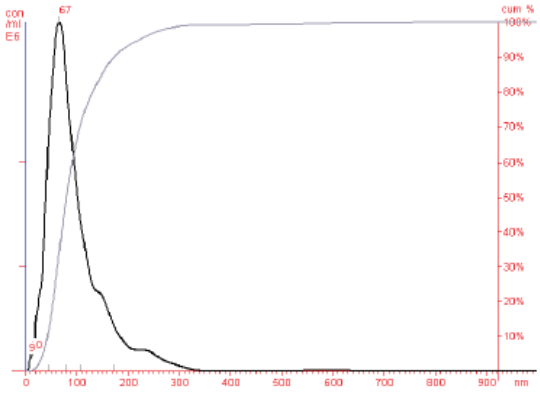

Particle Size / Concentration

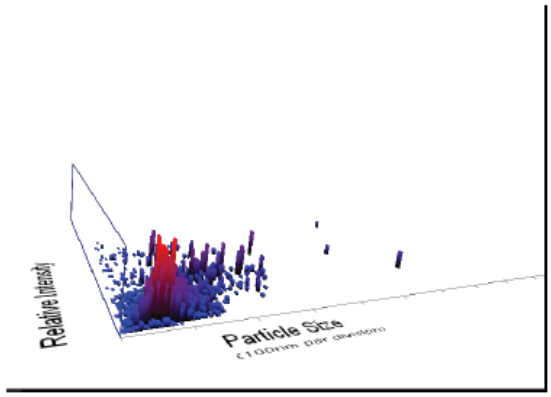

Particle Size / Relative Intensity 3D plot

Bin Centre (nm)	Concentration (E6 particles/ml)	Percentile Undersize (%)
10	1.988	0.730
30	16.580	6.815
50	49.210	24.875
70	63.987	48.359
90	45.765	65.155
110	28.373	75.569
130	17.817	82.108
150	14.325	87.365
170	9.769	90.950
190	6.100	93.189
210	4.340	94.782
230	4.067	96.274
250	3.402	97.523
270	2.199	98.330
290	1.399	98.843
310	0.800	99.137
330	0.311	99.251
350	0.099	99.288
370	0.050	99.306
390	0.025	99.315
410	0.017	99.321
430	0.037	99.335
450	0.080	99.365
470	0.122	99.410
490	0.134	99.459
510	0.122	99.504
530	0.127	99.550
550	0.171	99.613
570	0.233	99.699
590	0.264	99.795
610	0.237	99.882
630	0.168	99.944
650	0.093	99.978
670	0.041	99.993

Bin Centre (nm)	Concentration (E6 particles/ml)	Percentile Undersize (%)
690	0.014	99.998
710	0.004	100.000
730	0.001	100.000
750	0.000	100.000
770	0.000	100.000
790	0.000	100.000
810	0.000	100.000
830	0.000	100.000
850	0.000	100.000
870	0.000	100.000
890	0.000	100.000
910	0.000	100.000
930	0.000	100.000
950	0.000	100.000
970	0.000	100.000
990	0.000	100.000
1000-2000	0.000	100.000

Results

Mean:	100 nm
Mode:	67 nm
SD:	66 nm
D10:	44 nm
D50:	81 nm
D90:	173 nm
User Lines:	0 nm, 0 nm
Concentration:	2.72 E8 particles/ml
Completed Tracks:	3181

Measurement Conditions

Temperture:	21.60 °C
Viscosity:	0.96 cP
Frames Per Second:	30.00
Measurement Time:	0 of 215 s
Drift Velocity:	598 nm/s
Camera Shutter:	30 ms

Analysis Conditions

Blur:	Auto
Detection Threshold:	4 Multi
Min Track Length:	Auto
Min Expected Size:	30nm

Figure A-8. NTA Size Distribution Analysis for C_{60}-1.

NANOSIGHT

ANALYSIS REPORT

Nanoparticle Tracking Analysis (NTA) Version 2.3 Build 0011 RC1

Sample:	EIC May 2008 C60 Colloids
Date/Time of Capture:	17 August 2012 16:32
Video File:	may2008_unfiltered_12500x_17aug12-3.avi analysis no: 004
Operator:	andy clements
Comments:	

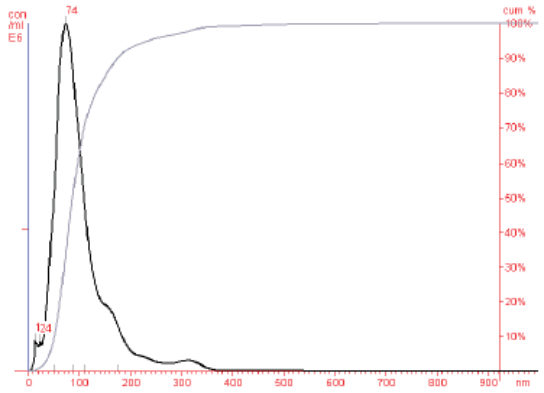

Particle Size / Concentration

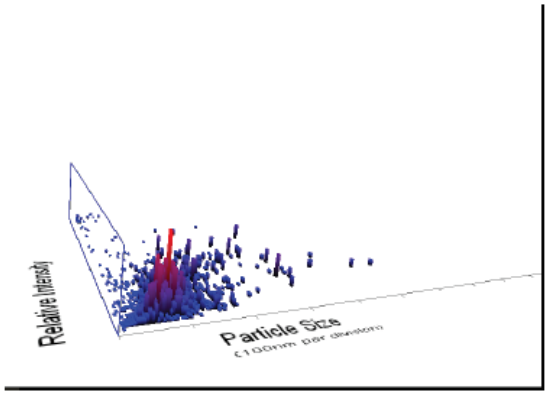

Particle Size / Relative Intensity 3D plot

Bin Centre (nm)	Concentration (E6 particles/ml)	Percentile Undersize (%)
10	1.535	0.799
30	5.714	3.774
50	23.643	16.085
70	46.321	40.204
90	41.120	61.615
110	25.227	74.750
130	13.500	81.780
150	9.568	86.762
170	7.564	90.701
190	4.300	92.940
210	2.545	94.265
230	2.017	95.315
250	1.416	96.053
270	1.148	96.651
290	1.260	97.307
310	1.521	98.099
330	1.247	98.748
350	0.583	99.052
370	0.209	99.160
390	0.168	99.248
410	0.201	99.352
430	0.210	99.462
450	0.200	99.566
470	0.184	99.662
490	0.168	99.750
510	0.148	99.827
530	0.123	99.891
550	0.093	99.939
570	0.062	99.972
590	0.034	99.989
610	0.014	99.997
630	0.005	99.999
650	0.001	100.000
670	0.000	100.000

Bin Centre (nm)	Concentration (E6 particles/ml)	Percentile Undersize (%)
690	0.000	100.000
710	0.000	100.000
730	0.000	100.000
750	0.000	100.000
770	0.000	100.000
790	0.000	100.000
810	0.000	100.000
830	0.000	100.000
850	0.000	100.000
870	0.000	100.000
890	0.000	100.000
910	0.000	100.000
930	0.000	100.000
950	0.000	100.000
970	0.000	100.000
990	0.000	100.000
1000-2000	0.000	100.000

Results

Mean:	106 nm
Mode:	74 nm
SD:	65 nm
D10:	52 nm
D50:	88 nm
D90:	175 nm
User Lines:	0 nm, 0 nm
Concentration:	1.92 E8 particles/ml
Completed Tracks:	2161

Measurement Conditions

Temperture:	22.30 °C
Viscosity:	0.95 cP
Frames Per Second:	30.00
Measurement Time:	215 of 215 s
Drift Velocity:	558 nm/s
Camera Shutter:	30 ms

Analysis Conditions

Blur:	Auto
Detection Threshold:	4 Multi
Min Track Length:	Auto
Min Expected Size:	30nm

Figure A-9. NTA Size Distribution Analysis for C_{60}-2.

NANOSIGHT

ANALYSIS REPORT

Nanoparticle Tracking Analysis (NTA) Version 2.3 Build 0011 RC1

Sample: EIC P52 C60 Colloids
Date/Time of Capture:
Video File: p52_unfiltered_12500x_17aug12.avi analysis no: 002
Operator: andy clements
Comments:

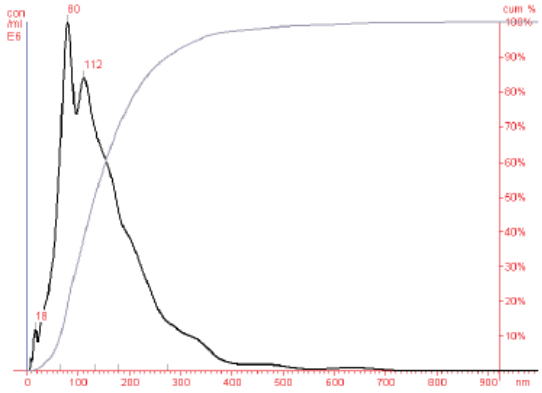

Particle Size / Concentration

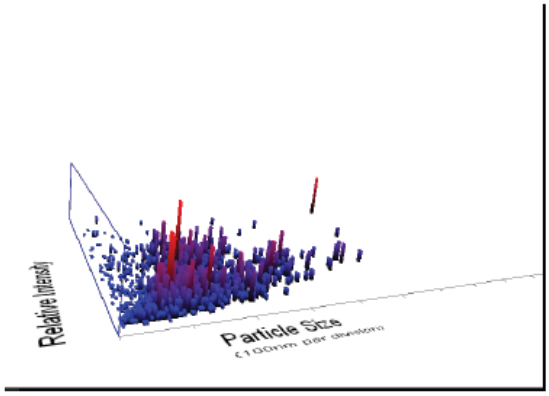

Particle Size / Relative Intensity 3D plot

Bin Centre (nm)	Concentration (E6 particles/ml)	Percentile Undersize (%)
10	1.065	0.637
30	3.536	2.752
50	7.560	7.274
70	18.316	18.228
90	20.810	30.675
110	19.770	42.499
130	17.683	53.075
150	15.299	62.225
170	12.931	69.959
190	10.171	76.043
210	8.719	81.258
230	6.824	85.339
250	5.015	88.339
270	3.702	90.553
290	3.089	92.400
310	2.619	93.967
330	2.284	95.333
350	1.737	96.372
370	1.063	97.007
390	0.664	97.404
410	0.501	97.704
430	0.445	97.970
450	0.448	98.238
470	0.453	98.509
490	0.403	98.750
510	0.300	98.929
530	0.200	99.049
550	0.148	99.138
570	0.145	99.225
590	0.175	99.329
610	0.215	99.458
630	0.242	99.603
650	0.235	99.743
670	0.190	99.856

Bin Centre (nm)	Concentration (E6 particles/ml)	Percentile Undersize (%)
690	0.126	99.932
710	0.069	99.973
730	0.030	99.991
750	0.011	99.998
770	0.003	99.999
790	0.001	100.000
810	0.000	100.000
830	0.000	100.000
850	0.000	100.000
870	0.000	100.000
890	0.000	100.000
910	0.000	100.000
930	0.000	100.000
950	0.000	100.000
970	0.000	100.000
990	0.000	100.000
1000-2000	0.000	100.000

Results

Mean:	157 nm
Mode:	80 nm
SD:	96 nm
D10:	66 nm
D50:	133 nm
D90:	274 nm
User Lines:	0 nm, 0 nm
Concentration:	1.67 E8 particles/ml
Completed Tracks:	1339

Measurement Conditions

Temperture:	22.00 °C
Viscosity:	0.95 cP
Frames Per Second:	30.00
Measurement Time:	215 of 215 s
Drift Velocity:	451 nm/s
Camera Shutter:	30 ms

Analysis Conditions

Blur:	Auto
Detection Threshold:	4 Multi
Min Track Length:	Auto
Min Expected Size:	30nm

Figure A-10. NTA Size Distribution Analysis for C_{60}-3.

REFERENCES

1. C. P. Singh and S. Roy, "Dynamics of all-optical switching in C[sub 60] and its application to optical logic gates," Optical Engineering **43**(2), 426-431 (2004).

2. K. Mansour, M. J. Soileau, and E. W. Vanstryland, "Nonlinear optical-properties of carbon-black suspensions (ink)," Journal of the Optical Society of America B-Optical Physics **9**(7), 1100-1109 (1992).

3. A. Fein, Z. Kotler, J. Bar-Sagi, S. Jackel, P. Shaier, and B. Zinger, "Nonlinear transmission characteristics of carbon-black suspensions," presented at the FRISNO 3. 3rd French-Israeli Symposium on Nonlinear-Optics. Dead Sea, Israel. 6-10 Feb. 1994., 1995.

4. F. Fougeanet and D. Riehl, "Investigation of optical limiting mechanisms in carbon-black suspensions," Molecular Crystals and Liquid Crystals Science and Technology Section B: Nonlinear Optics **21**(1-4), 435-446 (1999).

5. D. Riehl and F. Fougeanet, "Thermodynamic modeling of optical limiting mechanisms in carbon-black suspensions (CBS)," Molecular Crystals and Liquid Crystals Science and Technology Section B: Nonlinear Optics **21**(1-4), 391-398 (1999).

6. O. Durand, V. Grolir-Mazza, and R. Frey, "Temporal and angular analysis of nonlinear scattering in carbon-black suspensions in water and ethanol," Journal of the Optical Society of America B (Optical Physics) **16**(9), 1431-1438 (1999).

7. I. M. Belousova, N. G. Mironova, A. G. Scobelev, and M. S. Yur'ev, "The investigation of nonlinear optical limiting by aqueous suspensions of carbon nanoparticles," Optics Communications **235**(4-6), 445-452 (2004).

8. K. J. McEwan, P. K. Milsom, and D. B. James, "Nonlinear optical effects in carbon suspension," presented at the Nonlinear Optical Liquids for Power Limiting and Imaging. San Diego, CA, SPIE. 22 July, 1998.

9. H. W. Kroto, J. R. Heath, S. C. Obrien, R. F. Curl, and R. E. Smalley, "C-60 - Buckminsterfullerene," Nature **318**(6042), 162-163 (1985).

10. T. W. Ebbesen, K. Tanigaki, and S. Kuroshima, "Excited-state properties of C60," Chemical Physics Letters **181**(6), 501-504 (1991).

11. R. J. Sension, C. M. Phillips, A. Z. Szarka, W. J. Romanow, A. R. McGhie, J. P. McCauley, A. B. Smith, and R. M. Hochstrasser, "Transient absorption studies of carbon (C60) in solution," J. Phys. Chem. **95**(16), 6075-6078 (1991).

12. W. J. Blau, H. J. Byrne, D. J. Cardin, T. J. Dennis, J. P. Hare, H. W. Kroto, R. Taylor, and D. R. M. Walton, "Large infrared nonlinear optical response of C60," Physical Review Letters **67**(11), 1423 (1991).

13. K. M. Creegan, J. L. Robbins, W. K. Robbins, J. M. Millar, R. D. Sherwood, P. J. Tindall, D. M. Cox, A. B. Smith, J. P. McCauley, D. R. Jones, and R. T. Gallagher, "Synthesis and characterization of (C60)O, the 1st fullerene epoxide," Journal of the American Chemical Society **114**(3), 1103-1105 (1992).

14. R. V. Bensasson, T. Hill, C. Lambert, E. J. Land, S. Leach, and T. G. Truscott, "Pulse-radiolysis study of buckminsterfullerene in benzene solution - Assignment of the C-60 Triplet-Triplet Absorption-Spectrum," Chemical Physics Letters **201**(1-4), 326-335 (1993).

15. M. R. Fraelich and R. B. Weisman, "Triplet-states of C-60 and C-70 in solution - long intrinsic lifetimes and energy pooling," Journal of Physical Chemistry **97**(43), 11145-11147 (1993).

16. M. Fujitsuka, A. Watanabe, O. Ito, K. Yamamoto, and H. Funasaka, "Laser flash photolysis study on photochemical generation of radical cations of fullerenes C-60, C-70, and C-76," Journal of Physical Chemistry A **101**(43), 7960-7964 (1997).

17. V. Klimov, L. Smilowitz, H. Wang, M. Grigorova, J. M. Robinson, A. Koskelo, B. R. Mattes, F. Wudl, and D. W. McBranch, "Femtosecond to nanosecond dynamics in fullerenes: Implications for excited-state optical nonlinearities," Research on Chemical Intermediates **23**(7), 587-600 (1997).

18. J. W. Arbogast, A. P. Darmanyan, C. S. Foote, Y. Rubin, F. N. Diederich, M. M. Alvarez, S. J. Anz, and R. L. Whetten, "Photophysical properties of C60," Journal of Physical Chemistry **95**(1), 11-12 (1991).

19. S. V. Rao, D. N. Rao, J. A. Akkara, B. S. DeCristofano, and D. Rao, "Dispersion studies of non-linear absorption in C-60 using Z-scan," Chemical Physics Letters **297**(5-6), 491-498 (1998).

20. T.-H. Wei, T.-H. Huang, T.-T. Wu, P.-C. Tsai, and M.-S. Lin, "Studies of nonlinear absorption and refraction in C60/toluene solution," Chemical Physics Letters **318**(1-3), 53-57 (2000).

21. C.-C. Wu, T.-M. Liu, T.-Y. Wei, L. Xin, Y.-C. Li, L.-S. Lee, C.-K. Chang, J.-L. Tang, S. S. Yang, and T.-H. Wei, "Kramers-Kronig relation between nonlinear absorption and refraction of C60 and C70," Opt. Express **18**(22), 22637-22650.

22. D. G. McLean and M. C. Brant, "Triplet-triplet nonlinear absorption dynamics in C60," presented at the Laser Radiation Photophysics, Los Angeles, CA, USA, 1993.

23. D. G. McLean, R. L. Sutherland, M. C. Brant, D. M. Brandelik, P. A. Fleitz, and T. Pottenger, "Nonlinear absorption study of a C60-toluene solution," Opt. Lett. **18**(11), 858-860 (1993).

24. J. Barroso, A. Costela, I. GarcÃ-a-Moreno, and J. L. Saiz, "Wavelength dependence of the nonlinear absorption of C60 and C70 toluene solutions," The Journal of Physical Chemistry A **102**(15), 2527-2532 (1998).

25. A. Nakamura, M. Ichida, and T. Yajima, "Ultrafast relaxation dynamics of photoexcitations in fullerenes," Progress in Crystal Growth and Characterization of Materials **33**(1-3), 169-173 (1996).

26. A. F. Hebard, R. C. Haddon, R. M. Fleming, and A. R. Kortan, "Deposition and characterization of fullerene films," Applied Physics Letters **59**(17), 2109-2111 (1991).

27. V. P. Dravid, S. Liu, and M. M. Kappes, "Transmission electron microscopy of chromatographically purified solid state C60 and C70," Chemical Physics Letters **185**(1-2), 75-81 (1991).

28. W. I. F. David, R. M. Ibberson, J. C. Matthewman, K. Prassides, T. J. S. Dennis, J. P. Hare, H. W. Kroto, R. Taylor, and D. R. M. Walton, "Crystal structure and bonding of ordered C60," Nature **353**(6340), 147-149 (1991).

29. M. J. Rosker, H. O. Marcy, T. Y. Chang, J. T. Khoury, K. Hansen, and R. L. Whetten, "Time-resolved degenerate 4-wave-mixing in thin-films of C-60 and C-70 using femtosecond optical pulses," Chemical Physics Letters **196**(5), 427-432 (1992).

30. T. Ichihashi, K. Tanigaki, T. W. Ebbesen, S. Kuroshima, and S. Iijima, "Structures of C60 thin films fabricated on alkali halide substrates by organic MBE," Chemical Physics Letters **190**(3-4), 179-183 (1992).

31. T. W. Ebbesen, Y. Mochizuki, K. Tanigaki, and H. Hiura, "Direct observation of C-60 exciton," Europhysics Letters **25**(7), 503-508 (1994).

32. K. Tanigaki, S. Kuroshima, and T. W. Ebbesen, "Crystal-growth and structure of fullerene thin-films," Thin Solid Films **257**(2), 154-165 (1995).

33. M. Ichida, M. Sakai, T. Yajima, and A. Nakamura, "Luminescence properties and relaxation dynamics of photoexcited states in C60 solids," Progress in Crystal Growth and Characterization of Materials **33**(1-3), 125-128 (1996).

34. R. A. Cheville and N. J. Halas, "Time-resolved carrier relaxation in solid C-60 thin-films," Physical Review B **45**(8), 4548-4550 (1992).

35. N. J. Halas, V. Papanyan, R. D. Averitt, P. Pippenger, and R. A. Cheville, "Solvent-free high-purity solid C-60 - optical-properties," Molecular Crystals and Liquid Crystals Science and Technology Section a-Molecular Crystals and Liquid Crystals **256**, 225-232 (1994).

36. S. L. Dexheimer, W. A. Vareka, D. Mittleman, A. Zettl, and C. V. Shank, "Nonexponential relaxation in solid C-60 via time-dependent singlet exciton annihilation," Chemical Physics Letters **235**(5-6), 552-557 (1995).

37. S. R. Flom, F. J. Bartoli, H. W. Sarkas, C. D. Merritt, and Z. H. Kafafi, "Resonant nonlinear-optical properties and excited-state dynamics of pristine, oxygen-doped, and photopolymerized C-60 in the solid-state," Physical Review B **51**(17), 11376-11381 (1995).

38. A. Nakamura, M. Ichida, T. Yajima, H. Shinohara, and Y. Saitoh, "Ultrafast relaxation of excitons and photopolymerization in C-60 and C-70," Journal of Luminescence **66-7**(1-6), 383-388 (1995).

39. G. Gu, W. C. Zhang, H. Zen, Y. W. Du, Y. N. Han, W. J. Zhang, F. Z. Dong, and Y. X. Xia, "Large nonlinear absorption in C-60 thin-films," Journal of Physics B-Atomic Molecular and Optical Physics **26**(15), L451-L455 (1993).

40. R. A. Ganeev, A. I. Ryasnyansky, M. K. Kodirov, and T. Usmanov, "Nonlinear optical characteristics of C60 and C70 films and solutions," Optics Communications **185**(4-6), 473-478 (2000).

41. R. A. Ganeev, A. I. Ryasnyansky, V. I. Redkorechev, K. Fostiropoulos, G. Priebe, and T. Usmanov, "Variations of nonlinear optical characteristics of C-60 thin films at 532 nm," Optics Communications **225**(1-3), 131-139 (2003).

42. R. A. Ganeev, A. I. Ryasnyansky, V. I. Redkorechev, K. Fostiropoulos, G. Priebe, and T. Usmanov, "Nonlinear-optical parameters of thin C-60 films at 532 nm," Quantum Electronics **34**(1), 81-85 (2004).

43. S. D. Brorson, M. K. Kelly, U. Wenschuh, R. Buhleier, and J. Kuhl, "Femtosecond pump-probe investigation of electron dynamics in solid C-60 films," Physical Review B **46**(11), 7329-7332 (1992).

44. M. Sakai, M. Ichida, and A. Nakamura, "Raman scattering study of photopolymerization kinetics in C60 crystals," Chemical Physics Letters **335**(5-6), 559-566 (2001).

45. M. Sakai, M. Ichida, and A. Nakamura, "Photopolymerization and thermal decomposition of polymerized phase in C60 crystals under strong laser illumination," Fullerenes, Nanotubes and Carbon Nanostructures **9**(3), 351 - 361 (2001).

46. A. Kost, L. W. Tutt, M. B. Klein, T. K. Dougherty, and W. E. Elias, "Optical limiting with C60 in polymethyl methacrylate," Optics Letters **18**(5), 334-336 (1993).

47. L. W. Tutt and A. Kost, "Optical limiting performance in C60 and C70 solutions," Nature **356**, 225-226 (1992).

48. S. Couris, E. Koudoumas, A. A. Ruth, and S. Leach, "Concentration and wavelength dependence of the effective 3rd-order susceptibility and optical limiting of C-60 in toluene solution," Journal of Physics B-Atomic Molecular and Optical Physics **28**(20), 4537-4554 (1995).

49. M. P. Joshi, S. R. Mishra, H. S. Rawat, S. C. Mehendale, and K. C. Rustagi, "Investigation of optical limiting in C-60 solution," Applied Physics Letters **62**(15), 1763-1765 (1993).

50. M. P. Joshi, S. R. Mishra, H. S. Rawat, S. C. Mehendale, and K. C. Rustagi, "Investigation of optical limiting in C-60 solution (VOL 62, PG 1763, 1993)," Applied Physics Letters **63**(18), 2578-2578 (1993).

51. S. S. Harilal, C. V. Bindhu, V. P. N. Nampoori, and C. P. G. Vallabhan, "Optical limiting and thermal lensing studies in C60," Journal of Applied Physics **86**(3), 1388-1392 (1999).

52. Y. P. Sun, S. Gavrilyuk, J. C. Liu, C. K. Wang, H. Agren, and F. Gel'mukhanov, "Optical limiting and pulse reshaping of picosecond pulse trains by fullerene C60," Journal of Electron Spectroscopy and Related Phenomena **174**(1-3), 125-130 (2009).

53. Y. P. Sun and J. E. Riggs, "Organic and inorganic optical limiting materials. From fullerenes to nanoparticles," International Reviews in Physical Chemistry **18**(1), 43-90 (1999).

54. J. Schell, R. Levy, and B. Honerlage, "Limiting dynamics of C-60 in solid matrices," Journal of Nonlinear Optical Physics & Materials **9**(3), 315-342 (2000).

55. D. Vincent and J. Cruickshank, "Optical limiting with C60 and other fullerenes," Appl. Opt. **36**(30), 7794-7798 (1997).

56. S. R. Mishra, H. S. Rawat, and S. C. Mehendale, "Reverse saturable absorption and optical limiting in C-60 solution in the near-infrared," Applied Physics Letters **71**(1), 46-48 (1997).

57. J. E. Wray, K. C. Liu, C. H. Chen, W. R. Garrett, M. G. Payne, R. Goedert, and D. Templeton, "Optical power limiting of fullerenes," Applied Physics Letters **64**(21), 2785-2787 (1994).

58. A. Kost, J. E. Jensen, M. B. Klein, S. W. McCahon, M. B. Haeri, and M. E. Ehritz, "Optical limiting with C60 solutions," Proceedings of SPIE - The International Society for Optical Engineering **2229**, 78-90 (1994).

59. A. Kost, J. E. Jensen, M. B. Klein, J. C. Withers, R. O. Loufty, M. B. Haeri, and M. E. Ehritz, "Fullerene-based large-area passive broadband laser filters," Proceedings of SPIE - The International Society for Optical Engineering **2284**, 208-219 (1994).

60. R. V. Goedert, T. A. Whittaker, A. F. Clements, and G. Bourhill, "Imaging the response of an organic nonlinear optical material," Chemical Physics Letters **332**(3-4), 225-230 (2000).

61. S. R. Mishra, H. S. Rawat, M. P. Joshi, and S. C. Mehendale, "The role of nonlinear scattering in optical limiting in C60 solutions," Journal of Physics B-Atomic Molecular and Optical Physics **27**(8), L157-L163 (1994).

62. S. R. Mishra, H. S. Rawat, M. P. Joshi, and S. C. Mehendale, "On the contribution of nonlinear scattering to optical limiting in C-60 solution," Applied Physics a-Materials Science & Processing **63**(3), 223-226 (1996).

63. K. M. Nashold and D. P. Walter, "Investigations of optical limiting mechanisms in carbon particle suspensions and fullerene solutions," Journal of the Optical Society of America B (Optical Physics) **12**(7), 1228-1237 (1995).

64. Q. Ying, J. Marecek, and B. Chu, "Slow aggregation of buckminsterfullerene (C60) in benzene solution," Chemical Physics Letters **219**(3-4), 214-218 (1994).

65. Q. C. Ying, J. Marecek, and B. Chu, "Solution behavior of buckminsterfullerene (C-60) in benzene," Journal of Chemical Physics **101**(4), 2665-2672 (1994).

66. S. Nath, H. Pal, D. K. Palit, A. V. Sapre, and J. P. Mittal, "Aggregation of fullerene, C-60, in benzonitrile," Journal of Physical Chemistry B **102**(50), 10158-10164 (1998).

67. S. Nath, H. Pal, and A. V. Sapre, "Effect of solvent polarity on the aggregation of fullerenes: a comparison between C-60 and C-70," Chemical Physics Letters **360**(5-6), 422-428 (2002).

68. S. Nath, H. Pal, and A. V. Sapre, "Effect of solvent polarity on the aggregation of C-60," Chemical Physics Letters **327**(3-4), 143-148 (2000).

69. A. D. Bokare and A. Patnaik, "C-60 aggregate structure and geometry in nonpolar o-xylene," Journal of Physical Chemistry B **109**(1), 87-92 (2005).

70. A. D. Bokare and A. Patnaik, "Evidence for C-60 aggregation from solvent effects in [Ps-C-60] molecular complex formation," Carbon **41**(13), 2643-2651 (2003).

71. A. D. Bokare and A. Patnaik, "Microscopic diffusion model applied to C-60 fullerene fractals in carbon disulphide solution," Journal of Chemical Physics **119**(8), 4529-4538 (2003).

72. A. D. Bokare and A. Patnaik, "Self-organization of C-60 nanoparticles in carbon disulfide solution," Journal of Physical Chemistry B **107**(25), 6079-6086 (2003).

73. R. G. Alargova, S. Deguchi, and K. Tsujii, "Stable colloidal dispersions of fullerenes in polar organic solvents," Journal of the American Chemical Society **123**(43), 10460-10467 (2001).

74. H. N. Ghosh, A. V. Sapre, and J. P. Mittal, "Aggregation of C-7O in solvent mixtures," Journal of Physical Chemistry **100**(22), 9439-9443 (1996).

75. A. Mrzel, A. Mertelj, A. Omerzu, M. Copic, and D. Mihailovic, "Investigation of encapsulation and solvatochromism of fullerenes in binary solvent mixtures," Journal of Physical Chemistry B **103**(51), 11256-11260 (1999).

76. T. Rudalevige, A. H. Francis, and R. Zand, "Spectroscopic studies of fullerene aggregates," Journal of Physical Chemistry A **102**(48), 9797-9802 (1998).

77. Y. P. Sun and C. E. Bunker, "Formation and properties of C(70) solid-like species in room-temperature solutions," Chemistry of Materials **6**(5), 578-580 (1994).

78. Y. P. Sun and C. E. Bunker, "C-70 in solvent mixtures," Nature **365**(6445), 398-398 (1993).

79. J. D. Fortner, D. Y. Lyon, C. M. Sayes, A. M. Boyd, J. C. Falkner, E. M. Hotze, L. B. Alemany, Y. J. Tao, W. Guo, K. D. Ausman, V. L. Colvin, and J. B. Hughes, "C60 in water: Nanocrystal formation and microbial response," Environ. Sci. Technol. **39**(11), 4307-4316 (2005).

80. C. M. Sayes, J. Fortner, D. Lyon, K. D. Ausman, W. H. Guo, and V. Colvin, "Environmental implications of water-soluble nanoparticles," Abstracts of Papers of the American Chemical Society **227**, U1564-U1564 (2004).

81. C. M. Sayes, J. D. Fortner, W. Guo, D. Lyon, A. M. Boyd, K. D. Ausman, Y. J. Tao, B. Sitharaman, L. J. Wilson, J. B. Hughes, J. L. West, and V. L. Colvin, "The differential cytotoxicity of water-soluble fullerenes," Nano Letters **4**(10), 1881-1887 (2004).

82. C. M. Sayes, A. M. Gobin, K. D. Ausman, J. Mendez, J. L. West, and V. L. Colvin, "Nano-C-60 cytotoxicity is due to lipid peroxidation," Biomaterials **26**(36), 7587-7595 (2005).

83. Z. Markovic, B. Todorovic-Markovic, D. Kleut, N. Nikolic, S. Vranjes-Djuric, M. Misirkic, L. Vucicevic, K. Janjetovic, A. Isakovic, L. Harhaji, B. Babic-Stojic, M. Dramicanin, and V. Trajkovic, "The mechanism of cell-damaging reactive oxygen generation by colloidal fullerenes," Biomaterials **28**(36), 5437-5448 (2007).

84. J. Lee, J. D. Fortner, J. B. Hughes, and J. H. Kim, "Photochemical production of reactive oxygen species by C-60 in the aqueous phase during UV irradiation," Environmental Science & Technology **41**(7), 2529-2535 (2007).

85. G. V. Andrievsky, V. K. Klochkov, A. B. Bordyuh, and G. I. Dovbeshko, "Comparative analysis of two aqueous-colloidal solutions of C60 fullerene with help of FTIR reflectance and UV-Vis spectroscopy," Chemical Physics Letters **364**(1-2), 8-17 (2002).

86. G. V. Andrievsky, V. K. Klochkov, E. L. Karyakina, and N. O. McHedlov-Petrossyan, "Studies of aqueous colloidal solutions of fullerene C-60 by electron microscopy," Chemical Physics Letters **300**(3-4), 392-396 (1999).

87. G. V. Andrievsky, M. V. Kosevich, O. M. Vovk, V. S. Shelkovsky, and L. A. Vashchenko, "On the Production of an Aqueous Colloidal Solution of Fullerenes," J. Chem. Soc., Chem. Commun., 1281-1282 (1995).

88. J. Brant, H. Lecoanet, M. Hotze, and M. Wiesner, "Comparison of electrokinetic properties of colloidal fullerenes (n-C-60) formed using two procedures," Environmental Science & Technology **39**(17), 6343-6351 (2005).

89. A. Dhawan, J. S. Taurozzi, A. K. Pandey, W. Q. Shan, S. M. Miller, S. A. Hashsham, and V. V. Tarabara, "Stable colloidal dispersions of C-60 fullerenes in water: Evidence for genotoxicity," Environmental Science & Technology **40**(23), 7394-7401 (2006).

90. W. A. Scrivens, J. M. Tour, K. E. Creek, and L. Pirisi, "Synthesis of 14C-Labeled C60, Its Suspension in Water, and Its Uptake by Human Keratinocytes," J. Am. Chem. Soc. **116**(10), 4517-4518 (1994).

91. S. K. Ghosh, R. G. Alargova, S. Deguchi, and K. Tsujii, "Dispersion stability of colloids in sub- and supercritical water," Journal of Physical Chemistry B **110**(51), 25901-25907 (2006).

92. S. Deguchi, R. G. Alargova, and K. Tsujii, "Stable dispersions of fullerenes, C60 and C70, in water. Preparation and characterization," Langmuir **17**(19), 6013-6017 (2001).

93. L. K. Duncan, J. R. Jinschek, and P. J. Vikesland, "C60 colloid formation in aqueous systems: Effects of preparation method on size, structure, and surface charge," Environ. Sci. Technol. **42**(1), 173-178 (2008).

94. A. Beeby, J. Eastoe, and R. K. Heenan, "Solubilization of C-60 in aqueous micellar solution," Journal of the Chemical Society-Chemical Communications (2), 173-175 (1994).

95. H. Hungerbuhler, D. M. Guldi, and K. D. Asmus, "Incorporation of C-60 into artificial lipid-membranes," Journal of the American Chemical Society **115**(8), 3386-3387 (1993).

96. J. Eastoe, E. R. Crooks, A. Beeby, and R. K. Heenan, "Structure and photophysics in C-60-micellar solutions," Chemical Physics Letters **245**(6), 571-577 (1995).

97. D. M. Guldi, R. E. Huie, P. Neta, H. Hungerbühler, and K.-D. Asmus, "Excitation of C60, solubilized in water by triton X-100 and [gamma]-cyclodextrin, and subsequent charge separation via reductive quenching," Chemical Physics Letters **223**(5-6), 511-516 (1994).

98. D. M. Guldi, H. Hungerbuhler, and K. D. Asmus, "Radiolytic reduction of a water-soluble fullerene cluster," Journal of Physical Chemistry A **101**(10), 1783-1786 (1997).

99. M. Fujitsuka, H. Kasai, A. Masuhara, S. Okada, H. Oikawa, H. Nakanishi, A. Watanabe, and O. Ito, "Laser flash photolysis study on photochemical and photophysical properties of C-60 fine particle," Chemistry Letters (12), 1211-1212 (1997).

100. E. R. Crooks, J. Eastoe, and A. Beeby, "Photoexcited fullerene species in Triton-X100 micelles," Journal of the Chemical Society-Faraday Transactions **93**(23), 4131-4136 (1997).

101. A. W. Jensen, S. R. Wilson, and D. I. Schuster, "Biological applications of fullerenes," Bioorganic & Medicinal Chemistry **4**(6), 767-779 (1996).

102. V. P. Belousov, I. M. Belousova, E. A. Gavronskaya, V. A. Grigor'ev, O. B. Danilov, A. G. Kalintsev, N. G. Mironova, E. N. Sosnov, V. N. Zgonnik, and A. N. Ponomarev, "Broadband optical limiters based on fullerene-containing media with a fast nonlinear response in the visible region," Journal of Optical Technology **66**(8), 713-717 (1999).

103. V. P. Belousov, I. M. Belousova, E. A. Gavronskaya, V. A. Grigor'ev, A. G. Kalintsev, A. V. Kris'ko, D. A. Kozlovskii, N. G. Mironova, A. G. Skobelev, and M. S. Yur'ev, "Some regularities of nonlinear-optical limitation of laser radiation by fullerene-containing materials," Journal of Optical Technology **68**(12), 876-881 (2001).

104. I. M. Belousova, V. P. Belousov, O. B. Danilov, N. G. Mironova, T. D. Murav'eva, V. V. Ryl'kov, A. G. Skobelev, M. S. Yur'ev, and A. N. Ponomarev, "Nonlinear-optical limiters of laser radiation based on suspensions of carbon and fulleroid nanoparticles," Journal of Optical Technology **71**(3), 130-135 (2004).

105. I. M. Belousova, V. A. Grigor'ev, O. B. Danilov, A. G. Kalintsev, A. V. Kris'ko, N. G. Mironova, and M. S. Yur'ev, "Role of light-induced scattering in the optical limitation of laser radiation on the basis of fullerene-containing media," Optics and Spectroscopy **90**(2), 292-301 (2001).

106. I. M. Belousova, N. G. Mironova, A. G. Skobelev, and M. S. Yur'ev, "Femtosecond optical switches based on fullerene-containing media: Numerical simulation," Optics and Spectroscopy **102**(5), 760-764 (2007).

107. I. M. Belousova, N. G. Mironova, and M. S. Yur'ev, "Theoretical investigation of stimulated scattering mechanism in fullerene-containing media," Optics Communications **223**(1-3), 201-210 (2003).

108. I. M. Belousova, N. G. Mironova, and M. S. Yur'ev, "Bleaching of a fullerene-containing medium when it is acted on by nano- and femtosecond laser pulses," Journal of Optical Technology **70**(2), 89-91 (2003).

109. I. M. Belousova, N. G. Mironova, and M. S. Yur'ev, "Theoretical investigation of the dependence of attenuation of pulsed laser radiation by fullerene-containing solutions on the pulse duration," Optics and Spectroscopy **91**(5), 820-825 (2001).

110. A. Beeby, J. Eastoe, and E. R. Crooks, "Remarkable stability of C-60(center dot-) in micelles," Chemical Communications (8), 901-902 (1996).

111. R. J. Sension, A. Z. Szarka, G. R. Smith, and R. M. Hochstrasser, "Ultrafast photoinduced electron transfer to C60," Chemical Physics Letters **185**(3-4), 179-183 (1991).

112. SES Research, "Properties of Carbon 60, http://www.sesres.com/PhysicalProperties.asp", retrieved 11/16/2012.

113. The Dow Chemical Company, "http://dow-answer.custhelp.com/cgi-bin/dow_answer.cfg/php/enduser/std_adp.php?p_faqid=1668&p_created=1084563836&p_topview=1", retrieved 9/16/2008.

114. J. D. Lindberg, R. E. Douglass, and D. M. Garvey, "Imaginary refractive index of buckyballs," Appl. Opt. **32**(21), 3921-3922 (1993).

115. B. B. Weiner, W. W. Tscharnuter, and W. Bernt, "Characterizing ASTM carbon black reference materials using a disc centrifuge photosedimentometer," Journal of Dispersion Science and Technology **23**(5), 671-678 (2002).

116. A. I. Medalia and L. W. Richards, "Tinting strength of carbon black," Journal of Colloid and Interface Science **40**(2), 233-252 (1972).

117. R. V. Bensasson, E. Bienvenue, M. Dellinger, S. Leach, and P. Seta, "C60 in model biological systems. A visible-UV absorption study of solvent-dependent parameters and solute aggregation," J. Phys. Chem. **98**(13), 3492-3500 (1994).

118. F. Diederich, J. Effing, U. Jonas, L. Jullien, T. Plesnivy, H. Ringsdorf, C. Thilgen, and D. Weinstein, "C60 and C70 in a basket - Investigations of monolayer and multilayers from azacrown compounds and fullerenes," Angewandte Chemie-International Edition in English **31**(12), 1599-1602 (1992).

119. J. A. Brant, J. Labille, J. Y. Bottero, and M. R. Wiesner, "Characterizing the impact of preparation method on fullerene cluster structure and chemistry," Langmuir **22**(8), 3878-3885 (2006).

120. J. A. Brant, J. Labille, L. Y. Bottero, and M. R. Wiesner, "Comparative characteristics of aqueous suspensions of fullerene nanoclusters produced through different techniques," Abstracts of Papers of the American Chemical Society **230**, U1544-U1545 (2005).

121. D. Heymann, "Solubility of fullerenes C-60 and C-70 in seven normal alcohols and their deduced solubility in water," Fullerene Science and Technology **4**(3), 509-515 (1996).

122. D. Heymann, "Solubility of C-60 in alcohols and alkanes," Carbon **34**(5), 627-631 (1996).

123. R. S. Ruoff, D. S. Tse, R. Malhotra, and D. C. Lorents, "Solubility of C-60 in a variety of solvents," Journal of Physical Chemistry **97**(13), 3379-3383 (1993).

124. D. Boucher, S. A. Kovalenko, P. Masselin, Y. A. Matveets, M. G. Novikov, V. V. Ragulsky, A. G. Stepanov, and S. V. Chekalin, "Investigation of ultrafast relaxation of photoexcited fullerenes at different excitation conditions by broadband femtosecond laser spectrometry," Izvestiya Akademii Nauk Seriya Fizicheskaya **62**(2), 237-244 (1998).

125. D. Boucher, S. V. Chekalin, S. A. Kovalenko, A. Matveets Yu, P. Masselin, M. G. Novikov, V. V. Ragulsky, and A. G. Stepanov, "Investigation of ultrafast relaxation of fullerenes and fullerites by broadband femtosecond laser spectrometry," SPIE-Int. Soc. Opt. Eng. Proceedings of the SPIE - The International Society for Optical Engineering **3239**, 302-314 (1997).

126. J. E. Rogers, T. M. Cooper, P. A. Fleitz, D. J. Glass, and D. G. McLean, "Photophysical characterization of a series of platinum(II)-containing phenyl-ethynyl oligomers," J. Phys. Chem. A **106**(43), 10108-10115 (2002).

127. M. Sheik-Bahae, A. A. Said, T. H. Wei, D. J. Hagan, and E. W. Van Stryland, "Sensitive measurement of optical nonlinearities using a single beam," IEEE Journal of Quantum Electronics **26**(4), 760-769 (1990).

128. G. L. Wood, M. J. Miller, and A. G. Mott, "Investigation of tetrabenzporphyrin by the z-scan technique," Optics Letters **20**(9), 973-975 (1995).

129. L. Vivien, E. Anglaret, D. Riehl, F. Hache, F. Bacou, M. Andrieux, F. Lafonta, C. Journet, C. Goze, M. Brunet, and P. Bernier, "Optical limiting properties of singlewall carbon nanotubes," Optics Communications **174**(1-4), 271-275 (2000).

130. J. Williams, "Oceanographic Instrumentation," in *Oceanographic Instrumentation* (Naval Institute Press, Annapolis, MD, 1973), pp. 87-88.

131. LabSphere, Inc., "Integrating sphere theory and applications" (2012), retrieved Nov. 11, 2012, www.labsphere.com/technical/technical-guides.aspx.

132. R. Goedert, R. Becker, A. Clements, and T. Whittaker, "Time-resolved shadowgraphic imaging of the response of dilute suspensions to laser pulses," Journal of the Optical Society of America B-Optical Physics **15**(5), 1442-1462 (1998).

133. R. Goedert, R. Becker, A. Clements, and T. Whittaker, "Shadowgraphic imaging of dilute carbon and $Mo_2Ag_4S_8[PPh_3]_4$ suspensions," presented at the Materials for Optical Limiting II. Symposium. San Franicso, CA, 31 March-2 April, 1998.

134. R. V. Goedert, R. J. Becker, A. Clements, and T. A. Whittaker Iii, "Time-resolved shadowgraphic imaging of nonlinear liquids and suspensions," Proceedings of SPIE - The International Society for Optical Engineering **2853**, 54-72 (1996).

135. Google, "scatterlib" (July 5, 2012, 2012), retrieved Nov. 13, 2012, http://code.google.com/p/scatterlib/wiki/Spheres.

136. C. F. Bohren and D. R. Huffman, *Absorption and Scattering of Light by Small Particles* (Wiley-VCH Verlag GmbH & Co. KGaA, Weinheim, 2004), p. 530.

137. K. J. McEwan and P. A. Madden, "Transient grating effects in absorbing colloidal suspensions," Journal of Chemical Physics **97**(11), 8748-8759 (1992).

138. S. Egerev, S. Ermilov, O. Ovchinnikov, A. Fokin, D. Guzatov, V. Kilmov, A. Kanavin, and A. Oraevsky, "Acoustic signals generated by laser-irradiated metal nanoparticles," Applied Optics **48**(7), C38-C45 (2009).

139. E. A. Brujan, "Numerical investigation on the dynamics of cavitation nanobubbles," Microfluidics and Nanofluidics **11**(5), 511-517 (2011).

140. A. Kobyakov, D. J. Hagan, and E. W. Van Stryland, "Analytical approach to dynamics of reverse saturable absorbers," J. Opt. Soc. Am. B **17**(11), 1884-1893 (2000).

141. M. Daimon and A. Masumura, "Measurement of the refractive index of distilled water from the near-infrared region to the ultraviolet region," Appl. Opt. **46**, 3811-3820 (2007).

142. D. J. Segelstein, "The Complex Refractive Index of Water," (University of Missouri, Kansas City, 1981).